UNIVERSIDADE FEDERAL DO CEARÁ

CENTRO DE CIÊNCIAS

DEPARTAMENTO DE QUÍMICA ANALÍTICA E FÍSICO-QUÍMICA

PROGRAMA DE PÓS-GRADUAÇÃO EM QUÍMICA

DENIS VALONY MARTINS PAIVA

DIELECTRIC AND PHOTOLUMINESCENT INVESTIGATION OF Sr$_3$MO$_6$ (M = W or Mo) DOUBLE PEROVSKITE ELECTROCERAMIC

FORTALEZA

2018

DENIS VALONY MARTINS PAIVA

DIELECTRIC AND PHOTOLUMINESCENT INVESTIGATION OF Sr_3MO_6 (M = W or Mo) DOUBLE PEROVSKITE ELECTROCERAMIC

Doctoral thesis submitted to the Programa de Pós-Graduação em Química of the Universidade Federal do Ceará as a requirement for the degree of Doctor of Chemistry. Area: Physical Chemistry.

Advisor: Prof. Dr. Pierre Basílio Almeida Fechine.
Co-advisor: Dr. Marcelo Antônio Santos da Silva.

FORTALEZA

2018

DENIS VALONY MARTINS PAIVA

DIELECTRIC AND PHOTOLUMINESCENT INVESTIGATION OF Sr_3MO_6 (M = W or Mo) DOUBLE PEROVSKITE ELECTROCERAMIC

Doctoral thesis submitted to the Programa de Pós-Graduação em Química of the Universidade Federal do Ceará as a requirement for the degree of Doctor of Chemistry. Area: Physical Chemistry.

Aprovada em: ___/___/_____.

BANCA EXAMINADORA

_____
Prof. Dr. Pierre Basílio Almeida Fechine (Orientador)
Universidade Federal do Ceará (UFC)

_____
Prof. Dr. Alejandro Pedro Ayala
Universidade Federal do Ceará (UFC)

_____
Prof. Dr. Francisco Nivaldo Aguiar Freire
Universidade Federal do Ceará (UFC)

_____
Prof. Dr. Alan Silva de Menezes
Universidade Federal do Maranhão (UFMA)

_____
Prof. Dr. Manuel Pedro Fernandes Graça
Universidade de Aveiro (UA)

First, I thank God for everything.

I dedicate this work to my parents, Antonio de Brito Paiva and Dulce Helena Martins Paiva, my wife, Rana Cinaria Lima Benicio, my brother, Aecio Keynes Martins Paiva, and my dear friends who have helped me to become the professional I am today.

ACKNOWLEDGMENTS

"O Senhor é meu pastor e nada me faltará. "

Salmo 23

RESUMO

Neste trabalho, as propriedades dielétricas das duplas perovskitas Sr_3WO_6 (SWO) e Sr_3MoO_6 (SMO) na região de rádio frequência com variação de temperatura e na região de microondas para avaliar o material como um novo ressonador dielétrico, foram investigadas pela primeira vez na literatura, da qual podem ser encontradas no segundo e terceiro capítulo da tese, respectivamente. O processo de transferência de carga termo-ativada da cerâmica SWO foi observado com duas associações resistor-capacitor para os diagramas de Nyquist. SWO apresentou valores negativos de coeficiente de capacitância de temperatura (TCC) e a energia de ativação do processo de relaxação dielétrica possui valor em torno de 1,3eV. Para a região de microondas, o SWO mostra alta permissividade dielétrica (13,57) e perda dielétrica (0,0281). O coeficiente de temperatura da frequência de ressonância da cerâmica SWO foi obtido pela primeira vez nesta investigação dielétrica. A antena ressonante dielétrica (DRA) fabricada com a cerâmica SWO apresentou uma freqüência de operação de 4,1 GHz e perda de retorno abaixo de -40dB. Para a dupla perovskita SMO, foi proposto um circuito equivalente utilizando três associações de R-CPE em paralelo. A DRA baseada na cerâmica de SMO opera 3,71 GHz (frequência de antena de operação), com ganho razoável (5,00 dBi) e diretividade (5,70 dBi), onde esses valores são próximos aos apresentados pelas antenas comerciais. A partir desses resultados, as DRA baseadas nas cerâmicas de SWO e SMO mostram boas propriedades para serem usadas como um novo ressonador dielétrico na região de microondas. Uma vez concluída a primeira parte, envolvendo uma investigação dielétrica, da tese de doutorado, o próximo passo foi estudar as propriedades de fotoluminescência da matriz cerâmica de SMO com íons Eu^{3+} e Tb^{3+}. A síntese satisfatória de materiais dopados com terras raras, o mecanismo de transferência de energia e as emissões dos íons Eu^{3+} e a contribuição energética dos íons Tb^{3+} estão no quarto capítulo dessa tese. Pode-se inferir que os espectros de emissão da cerâmica Sr_3MoO_6 dopada individualmente com Eu^{3+} consistem em transições eletrônica de 5D para 7F. Os espectros de emissão da cerâmica dopada com Tb^{3+} e Eu^{3+} dopado, indicam influência dos íons Tb^{3+} no mecanismo de transferência de energia para os íons Eu^{3+} na matriz cerâmica. A investigação indica que a matriz cerâmica com os íons Tb^{3+} e Eu^3 podem ser um promissor candidato para aplicações em chips de LEDs.

Palavras-chave: Materiais cerâmicos. SWO. SMO. Dielétricos. Fotoluminescentes.

ABSTRACT

In this work, the dielectric properties of Sr_3WO_6 (SWO) and Sr_3MoO_6 (SMO) double perovskite at radio frequencies as a function of the temperature and a study in microwaves range to evaluate the material as a novel dielectric resonator, those studies were first investigated when can be found in the second and third chapter of the thesis, respectively. Thermo-activated charge transfer process for SWO ceramic was observed and two resistor – capacitor associations were fitted for the Nyquist diagram. SWO presented negative values of temperature coefficient of capacitance (TCC) and the activation energies of dielectric relaxation processes was obtained the value around 1.3eV. For the microwave range, SWO shows high dielectric permittivity (13.57) and dielectric loss (0.0281). The temperature coefficient of resonant frequency value was first obtained in the literature. The dielectric resonator antenna (DRA) fabricated from SWO ceramic presented an operation frequency in 4.1 GHz and return loss below -40dB. For the SMO double perovskite, it was proposed an equivalent circuit using three associations of R-CPE in parallel. The SMO-based DRA operated at 3.71 GHz (frequency of operation antenna), with reasonable gain (5.00 dBi) and directivity (5.70 dBi), where these values are close to the ones presented by commercial antennas. From these results, the SWO and SMO based DRA shows good properties to be used as a novel microwave dielectric resonator. Once the first part, involving a dielectric investigation, of the doctoral thesis was concluded, the next step was to study the photoluminescence properties of SMO phosphors with Eu^{3+} and Tb^{3+} ions. The satisfactory synthesis of phosphors, the energy transfer mechanism and band emission from Eu^{3+}, and energetic contribution of Tb^{3+} are in the fourth chapter. It noticed that the emission spectra of singly Eu^{3+} doped Sr_3MoO_6 phosphors consist emission transitions of 5D to 7F. The emission spectra of co-doped Tb^{3+} and Eu^{3+} doped Sr_3MoO_6 phosphor, there is an influence of Tb^{3+} ions in the energy transfer mechanism of Eu^{3+} ions in the phosphor. The investigation indicates that the phosphors may be a promising candidate phosphor for applications in LED chips.

Keywords: Ceramics materials. SWO. SMO. Dielectric. Photoluminescent.

LIST OF FIGURES

LIST OF TABLES

LIST OF ABBREVIATIONS AND ACRONYMS

IS	Impedance Spectroscopy
RF	Radiofrequency
SWO	Sr_3WO_6
LED	Light Emitting Diodes
LTCC	Low Temperature Cofired Ceramics
DRA	Dielectric Resonator Antenna
SMO.	Sr_3MoO_6
PXRD	Powder X-ray Diffraction
SEM	Scanning Electron Microscopy
EDS	Energy Dispersive X-ray Spectroscopy
HFSS	High Frequency Structure Simulator
SOFC	Solid Oxide Fuel-Cell
ICSD	Inorganic Crystal Structure Database
TCC	Temperature Coefficient of Capacitance
CPE	Constant Phase Element
SE	Secondary Electron
IEC	International Electrotechnical Commission
EIA	Electronic Industries Alliance
UV	Ultraviolet
wLED	White Light Emitting Diodes
CTS	Charge Transfer State

LIST OF SYMBOLS

Mo^{6+}	Molybdenum ionic
W^{6+}	Tungsten ionic
α	Alpha
β	Beta
γ	Gamma
δ	Delta
K	Kelvin
ε^*	Complex dielectric constant
ε'	Dielectric constant real part
ε''	Dielectric constant imaginary part
Z^*	Complex impedance
Z'	Impedance real part
Z''	Impedance imaginary part
σ^*	Electric conductivity
σ'	Electric conductivity real part
σ'_{ac}	alternating current electric conductivity real part
σ''	Electric conductivity imaginary part
M^*	Electric modulus
M'	Electric modulus real part
M''	Electric modulus imaginary part
$\tan \delta$	Loss tangent
C_0	Vacuum capacitance
Ω	Ohm
$f_{HE11\delta}$	Resonance frequency
c	Velocity of light in the vacuum
a	Radius
h	Height
S	Quality factor
R_{wp}	Weighted residual error
%wt	Weight percent
E_a	Activation energy

A_0 Pre-exponential factor

k   Boltzmann's constant

RC   Resistor-Capacitor

n Deviation of ideal capacitance

τ_f Temperature coefficient of resonant frequency

S_{11} Return loss

BW   Bandwidth

RE^{3+} Rare earth

SUMÁRIO

1 INTRODUCTION AND OBJECTIVES

1.1 Introduction

1.1.1 Double perovskite

Ceramic oxides with structural formula $A_2B'B''O_6$ are called double perovskite. In this kind of structure, the A site generally is a large divalent cation twelve-coordinated and B' and B'' sites are octahedral-coordinated with varied oxidation state and commonly occupied by transition metal ions, as can be seen in Figure 1. The double perovskite presents a large number of different compositions, as a wide combination of ions in the B' and B'' sites, where the final combination must be a sum of charges equal to 8+ or the necessary charge for complete electroneutrality of the structure due to the charges of A site (Ca^{2+}, Sr^{2+}, Li^+, La^{3+} etc) (VASALA; KARPPINEN, 2014). In this sense, different applications can be obtained by changing in these sites, such as photocatalyst, (A_2ZnTiO_6) (A = Pr, Gd) (ZHU et al., 2017), a thermoelectric device, (Sr_2TiMoO_6) (SAXENA *et al.*, 2017), and an electrode for fuel cell, ($SmBa_{1-x}Ca_xCoCuO_{5+\delta}$) (WANG *et al.*, 2016). Dielectric properties of double perovskite ceramics ((A_2HoSbO_6 (A = Ba, Sr, Ca), Pr_2CuTiO_6 and Ba_2BiNbO_6) have been studied by Impedance Spectroscopy (IS) in Radiofrequency (RF) range (PANDA *et al.*, 2015; MAHATO; SINHA, 2016; HALDER *et al.*, 2017).

Sr_3WO_6 (SWO) is another example of double perovskite that has been traditionally studied due to luminescence properties: the photoluminescence and thermoluminescence properties of $Sr_3WO_6:Eu^{3+}$ was reported by Emen and Altinkaya (2013), while Zhigang Zou *et al.* (2013) obtained an efficient charge compensated red phosphor for $Sr_3WO_6:K^+$, Eu^{3+} for white Light emitting diodes (LED). The SWO perovskite structure are also an important oxide class for dielectric materials, but to our knowledge, the dielectric properties have not been reported. Due the similarly between molybdenum (Mo^{6+}) and tungsten (W^{6+}) ionic ratio and electrovalence allows an structural investigation Low temperature cofired ceramics (LTCC) based, the Sr_3MoO_6 double perovskite. In the literature have been many reports LTCC based molybdates materials (ZHOU. *et al.*, 2011; TANG *et al.*, 2013; JOSEPH *et al.*, 2016). The influence of Mo^{6+} in dielectric properties, sintering temperature and Dielectric resonator antenna (DRA) application have never been studied for the Sr_3MoO_6 (SMO) ceramic. Actually, few studies examine the properties of SMO double perovskite, such as the red phosphors $Sr_3MoO_6:Eu^{3+}$ applied in the white light emitting diode

(JING *et al.*, 2015).

Figure 1 - Different B-site cation orderings found in $A_2B'B''O_6$ perovskites: (a) rock-salt, (b) layered and (c) columnar order.

(a) (b) (c)
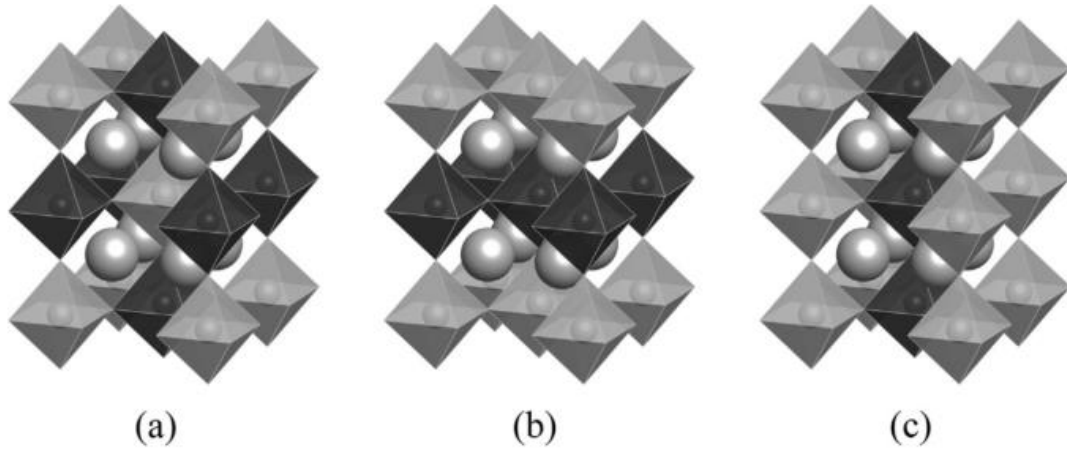
Source: (VASALA; KARPPINEN, 2014)

1.1.2 Dielectric resonator antenna

The microwave region of the electromagnetic spectrum (see Figure 2) has been attracted attention due to the rapid development of technology for this frequency range in last decades. The demand for dielectric materials in the microelectronics industry has increased for different range communications. (PARIDA *et al.*, 2012). The development in DRA application influenced in growing of the telecommunication field in the microwave range (PARIDA *et al.*, 2012)(LUK; LEUNG, 2003), which are low loss ceramic pucks used mainly in wireless communication devices. Compared to other antenna devices, DRAs have lower weight and cost, high radiation efficiency, small size, different geometry (cylindrical, rectangular, half-hemispherical etc.) and feeding (slots, probes, waveguides etc.). This device converts a wave propagation on a transmission line to a plane wave propagation in free-space (transmission or reception).(PARIDA *et al.*, 2012)(ALMEIDA *et al.*, 2008).

The use of dielectric oxide ceramics has changed the microwave wireless communication production due to decrease the size and cost of diverse components, like as filter, oscillator and antenna components in applications ranging from cellular phones to global positioning systems. The demand for miniaturization has been growing in the last years provides a continuing driving force for the discovery and advancement of increasingly sophisticated materials. (SEBASTIAN, 2008).

Figure 2 – Microwave spectrum and application.
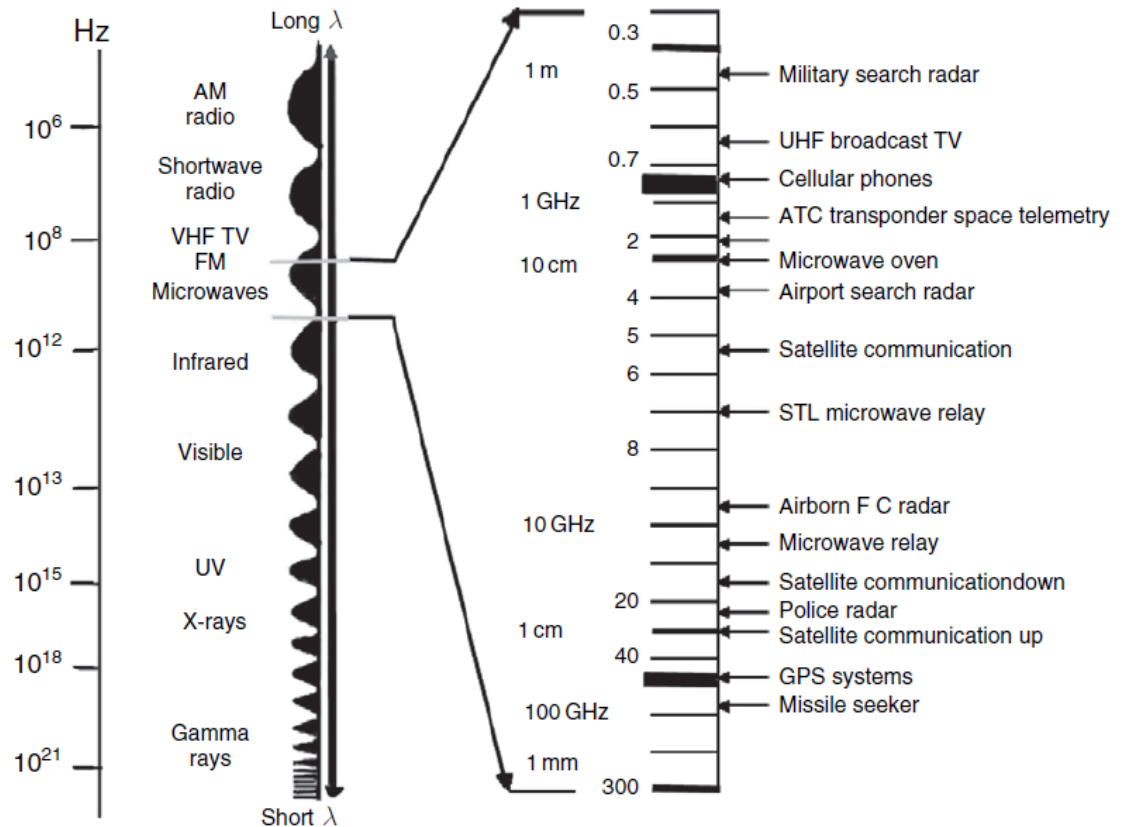
Source: (SEBASTIAN, 2008)

1.2 Objectives

1.2.1 General

- To explore the dielectric properties at RF/microwave of Sr_3MO_6 (M = W or Mo) in order to apply in microwave application as dielectric resonator antenna and to investigate the photoluminescent of $Sr_3MoO_6{:}Eu^{3+}/Tb^{3+}$ phosphors.

1.2.2 Specifics

- To synthesize Sr_3WO_6 and Sr_3MoO_6 by solid state route;
- To investigate the structure of Sr_3WO_6 and Sr_3MoO_6 synthesized at different temperatures by using powder X-ray diffraction (PXRD);
- To analyze the microstructural of Sr_3MoO_6 ceramic by micrograph images from Scanning electron microscopy (SEM) and Energy dispersive X-ray spectroscopy

(EDS);

- To analyze the dielectric properties of Sr_3WO_6 and Sr_3MoO_6 in radio-frequency as function of the temperature by IS;

- To explore the dielectric measurements in the microwave range of Sr_3WO_6 and Sr_3MoO_6;

- To investigate the temperature coefficient of resonant frequency of Sr_3WO_6 by dielectric measurements in the microwave range;

- To evaluate the DRA parameters of Sr_3WO_6 and Sr_3MoO_6 by numerical simulation via the High Frequency Structure Simulator (HFSS);

- To synthesize Tb^{3+}-Eu^{3+} co-doped Sr_3MoO_6 by solid state reaction;

- To investigate the structure of the Sr_3MoO_6:Eu^{3+}/Tb^{3+} synthesized using PXRD and SEM;

- To study the photoluminescent results using different excitation of Sr_3MoO_6:Eu^{3+}/Tb^{3+} phosphors.

2 DIELECTRIC INVESTIGATION OF THE Sr_3WO_6 DOUBLE PEROVSKITE AT RF/MICROWAVE FREQUENCIES

2.1 Introduction

Double perovskite are ceramic oxides with structural formula $A_2B'B''O_6$, when A site generally is a large divalent cation and B' and B'' sites are commonly occupied transition metal ions. The double perovskite presents a large number of different compositions due to the different combination of ions in the B' and B'' sites, hence different applications can be obtained by changing in these sites (VASALA; KARPPINEN, 2014). For example, La_2NiMnO_6 nanoparticles (WU $et\ al.$, 2013) have been studied for a potential carrier for large biomolecules, $Sr_2B'MoO_6$ (B' = Mg, Mn, Fe, Co, Ni and Zn) (WANG $et\ al.$, 2011; ZHANG $et\ al.$, 2011; JIANG $et\ al.$, 2014) has been found to be a promising compound as an anode material for solid-oxide fuel-cell (SOFCs) and Bi_2NiMnO_6 presents multiferroic properties at low temperature with potential as nonvolatile memories and sensors (SHIMAKAWA $et\ al.$, 2011). Pang and Zhou (2011) investigated Ca_3WO_6 phase, which presented good results for potential microwave applications (ZHOU $et\ al.$, 2012; ZHOU $et\ al.$, 2014), becoming important for development in wireless communication systems, miniaturization of components such as dielectric filters, and voltage-controlled oscillators.

Sr_3WO_6 (SWO) is another example of double perovskite that has two Sr^{2+} ions in site A and one Sr^{+2} and W^{6+} ions distributed in the B' and B'' sites. SWO presents four polymorphs (α, β, γ and δ) from low to high temperature (KING $et\ al.$, 2010). This material has been traditionally studied due to luminescence properties: the photoluminescence and thermoluminescence properties of $Sr_3WO_6:Eu^{3+}$ was reported by Emen and Altinkaya (2013), while Zhigang Zou $et\ al.$ (2013) obtained an efficient charge compensated red phosphor for $Sr_3WO_6:K^+$, Eu^{3+} for white LEDs. However, the SWO perovskite structure are also an important oxide class for dielectric materials with calcium, strontium and barium titanate, the most representative of perovskite structure for dielectric properties.

In this work, the best set of parameters to synthesize the SWO phase by solid-state route was achieved by PXRD. The dielectric properties of the material were measured at radio frequency as a function of the temperature (298-718 K). For microwave applications, SWO was experimentally measured as a dielectric resonator and supported by numerical simulation. The results set can be used to suggest potential novel applications for SWO phase as a DRA or other devices that operate in the microwaves range (microwave filters, oscillators, radar

detuctors etc.).

2.2 Experimental methods

The synthesis of the SWO phase was performed by a solid state route, where stoichiometric amounts of the precursors employed in the process were $SrCO_3$ (97%, Vetec) and WO_3 (99%, Aldrich). These starting materials were activated by milling in the planetary mill, on a Fritsch Pulverissette 6, for 2 h with zirconia balls and polyacetal vessels. The activated powder was calcined in air at 1323, 1423 and 1523 K for 6 h. The reactions occurring during calcination can be summarized as:

$$3SrCO_{3(s)} + WO_{3(s)} \rightarrow Sr_3WO_{6(s)} + 3CO_{2(g)} \tag{1}$$
$$3SrCO_{3(s)} + WO_{3(s)} \rightarrow (Sr_3WO_6)_{1-x(s)} + (SrWO_4)_{x(s)} + (SrO)_{2x(s)} + 3CO_{2(g)} \tag{2}$$
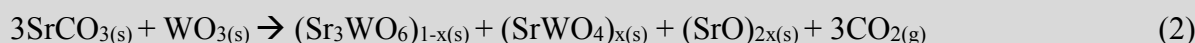
The second reaction shows a spurious phase ($SrWO_4$) and SrO (from decomposition of strontium carbonate). This probable reaction was observed for sample calcined at 1323K. However, SrO phase was not detected due to the small concentration and weak diffraction peak compared to Sr_3WO_6 and $SrWO_4$. Thus, it was not taken into account for crystal structure refinement (see XRD results).

The preparation of the samples for dielectric measurements consisted of the fabrication of pellets and a cylindrical ceramic. Thus, SWO powder was molded into a steel die by uniaxial press and its green body sintered at two steps (773 K for 2 h and after at 1523 K for 6 h), see Figure 3. The pellets and cylinders were polished after the sintering process. For analysis by IS, both faces of the ceramic pellet were covered with a silver conductive electrode to form a parallel face capacitor geometry. The dimensions of the pellets in dielectric were 14.04 mm of diameter and 7.34 mm of thickness for the microwave range, and 14.30 mm of diameter and 1.56 mm of thickness for the radio frequency range.

The diffractograms were obtained by PANalytical diffractometer (Xpert Pro MPD) operating at 40 kV and 45 mA in the geometry Bragg-Brentano, with a Cu tube ($K\alpha_1$ = 1.540562 Å, $K\alpha_2$ = 1.54439 Å) at room temperature (~300 K), from crushed samples of SWO in three different temperatures (1323, 1423 and 1523 K). The diffraction patterns were obtained from 15° to 65° (2θ) with a step size of 0.013°, with the analysis time at each step (70 s), using a plane graphite monochromator for diffracted beam. The Rietveld method's

(RIETVELD, 1967) was used for obtain the refinements through the DBWS Tools software (BLEICHER *et al.*, 2000), where the refined parameters were the lattice parameters, scale factor, background, U and X parameters, and overall thermal factors. The Inorganic Crystal Structure Database (ICSD) was used to identify what phases were present in the samples.

Figure 3 – The scheme used of the sintering process.
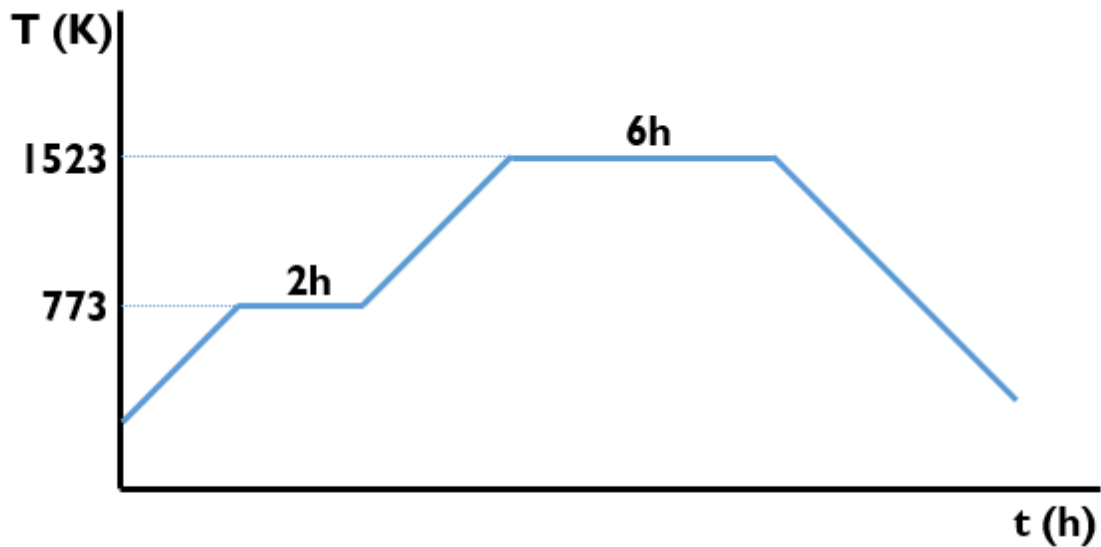
Source: Author.

The IS data (radiofrequency range) were collected in the Solartron 1260 Impedance Analyzer at different temperatures (298-718 K). For this propose, the electric properties of the SWO was represented in terms of the: complex dielectric constant ε^* $(\omega) = \varepsilon'$ $- j\varepsilon''$, complex impedance Z^* $(\omega) = Z' - jZ''$, electric conductivity $\sigma^*(\omega)=1/Z^*=\sigma'+j\sigma''$, electric modulus M^* $(\omega) = 1/ \varepsilon^*$ $(\omega) = M' + j M''$ and loss tangent $\tan \delta = \varepsilon''/\varepsilon'$, where $(')$ and $('')$ represents the real and imaginary part, respectively. Where $j= \omega C_0 Z^*$ and the vacuum capacitance is represented C_0 and $j = \sqrt{-1}$ (SOHN *et al.*, 2010)(COSTA *et al.*, 2010). Nyquist diagrams were obtained by fitting using the Eisanalyser software (BONDARENKO; RAGOISHA, 2005).

The Hakki-Coleman method (HAKKI; COLEMAN, 1960; COURTNEY, 1970) was used for dielectric measurements in the microwave range. For antenna applications, the ceramic cylinder was placed in a ground plane (copper sheet). The device was fed by a 50 Ω coaxial cable and SMA connector, as shown in Figure 4.

Figure 4 - Physical layout of the DRA displaying various components.
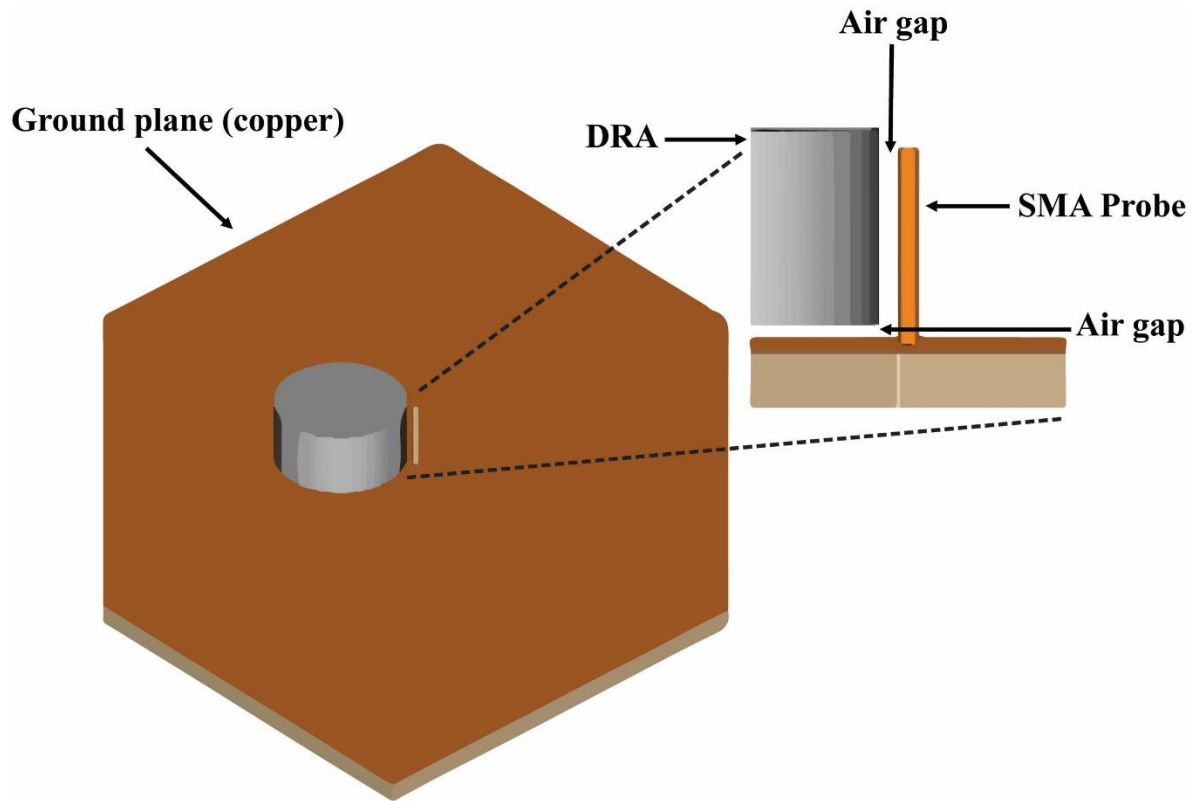
Source: Author.

Both measurements, by Hakki-Coleman method and by antenna configuration, were undertaken with an Agilent Network Analyser, model N5230A, at room temperature. Using numerical simulations via the HFSS of Ansoft, the electromagnetic fields generated by DRA were obtained by simulation of a perfect cylinder model above a perfect ground plane. The air gaps were inserted in the model targeting for approximation of real case between numerical and experimental data from HE11δ mode. Thus, the cylindrical DRA can be approximately by the following equation:

$$f_{HE11\delta} = \frac{6.324c}{2\pi a\sqrt{\varepsilon+2}}\left[0.27+0.36\left(\frac{a}{2h}\right)+0.02\left(\frac{a}{2h}\right)^2\right]$$

(3)

where $f_{HE11\delta}$ (GHz) is the measured resonance frequency and c is the velocity of light in the vacuum (299,792,458 m.s^{-1}), and a (m) is the radius and h (m) is the height of the cylindrical DRA (see Figure 4).

2.3 Results and discussion

Structural characterization was performed by the PXRD technique, where it was analyzed the SWO phase formation and/or reagents and presence of spurious phase in the obtained products. The Rietveld refinement was performed for validation of the observed phases in the tested temperatures. The residuals indicators, R_{Bragg}, S (quality factor, "goodness of fit") and R_{wp} (weighted residual error), showed a satisfactory refinement and that obtained values are adequate in the range of acceptable values (Rwp < 20 and S < 1.6). For the R_{Bragg}, the values are closer to the acceptable limits due to the experimental conditions (PASCOAL *et al.*, 2002)(SILVA *et al.*, 2014). The results of the refinement are showed in the Figure 5, where the black dots and red lines are used for represent the experimental and calculated data, respectively. The blue line is the difference between the experimental and calculated intensity. For the sample obtained at 1323K (incomplete reaction), diffraction peaks for SWO (ICSD: 24-7338, triclinic, C1) and an intermediate phase $SrWO_4$ (ICSD: 15-5425, tetragonal, C_{4h}^6) were observed. For samples synthesized at 1423 and 1523K, the diffractograms showed peaks only for SWO. The crystalline profile of the analyzed phases are also illustrated in Figure 5.

All refinements match with the experimental diffraction profile and there is not significant noise intense in the blue line (Figure 5). Thus, the refinements were satisfactory, as demonstrate parameters derived from the Reitveld refinement (Table 1 and Table 2), where the lattice parameters, cell volume and density showed no significant changes. One can also observe a small concentration of $SrWO_4$ (6.62 %wt) for the sample synthesized at 1323 K. Thus, the phase obtained at 1423K was chosen for the course of the work due to lower energy involved in the process.

Figure 5 - XRD partner and Rietveld refinement of the SWO samples obtained in different calcination temperatures, where black dots and red line are the experimental and calculated intensity, respectively. The difference between experimental and calculated is represented by blue line.
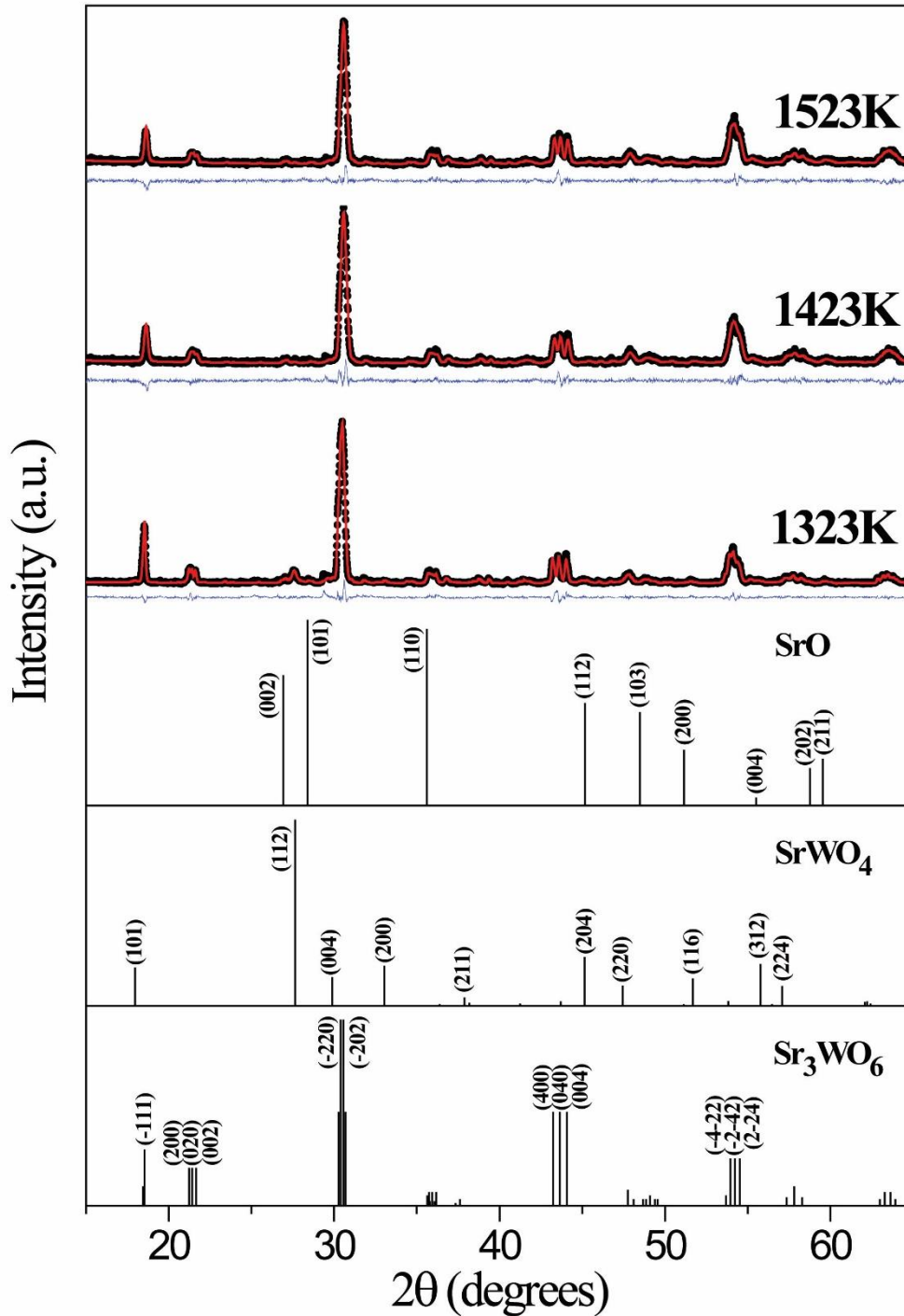
Source: Author.

Table 1 – Part 1 of the parameters obtained from Rietveld refinement of the samples SWO synthesized at 1323, 1423 and 1523K.

Sample	Phase	Lattice Parameters			R_{wp} (%)	R_{Bragg}	S
		a (Å)	b (Å)	c (Å)			
SWO (1323K)	Sr_3WO_6	10.093290	17.646570	11.813420	10.23	7.14	1.55
	$SrWO_4$	5.414999	5.414999	12.052610		8.17	
SWO (1423K)	Sr_3WO_6	10.092880	17.642370	11.814300	12.60	9.64	1.11
SWO (1523K)	Sr_3WO_6	10.097800	17.649710	11.815720	12.59	8.81	1.07

Source: Author.

Table 2 – Part 2 of the parameters obtained from Rietveld refinement of the samples SWO synthesized at 1323, 1423 and 1523K.

Sample	Phase	V_{cell}	Quantitative phase analysis (%wt)	Density (g.cm^{-3})
SWO (1323K)	Sr_3WO_6	1714.028	93.38	6.311
	$SrWO_4$	353.409	6.62	6.306
SWO (1423K)	Sr_3WO_6	1713.669	100.0	6.312
SWO (1523K)	Sr_3WO_6	1715.148	100.0	6.307

Source: Author.

IS technique was used for analyzing the electric response of SWO ceramic under influence of the variation of frequency as a function of the temperature, and investigate the dielectric behavior. By measurements of IS is possible to find the phase transitions of the materials. In this sense, ε' was measured at 1 MHz and plotted as a function of the temperature (Figure 6). It can be seen a maximum value for ε' at 445K, corresponding to the transition temperature observed in literature (DRACHE *et al.*, 1981)(CHANG; PHILLIPS, 1967), where the SWO transits from triclinic to monoclinic symmetry, i. e., the γ↔β phase transition. King and coworkers (KING *et al.*, 2010) observed the same phenomena by using electron diffraction, synchrotron X-ray powder diffraction and neutron powder diffraction.

Figure 6 - ε' measured at 1MHz as a function of the temperature and the representative picture of phase transition (inset).
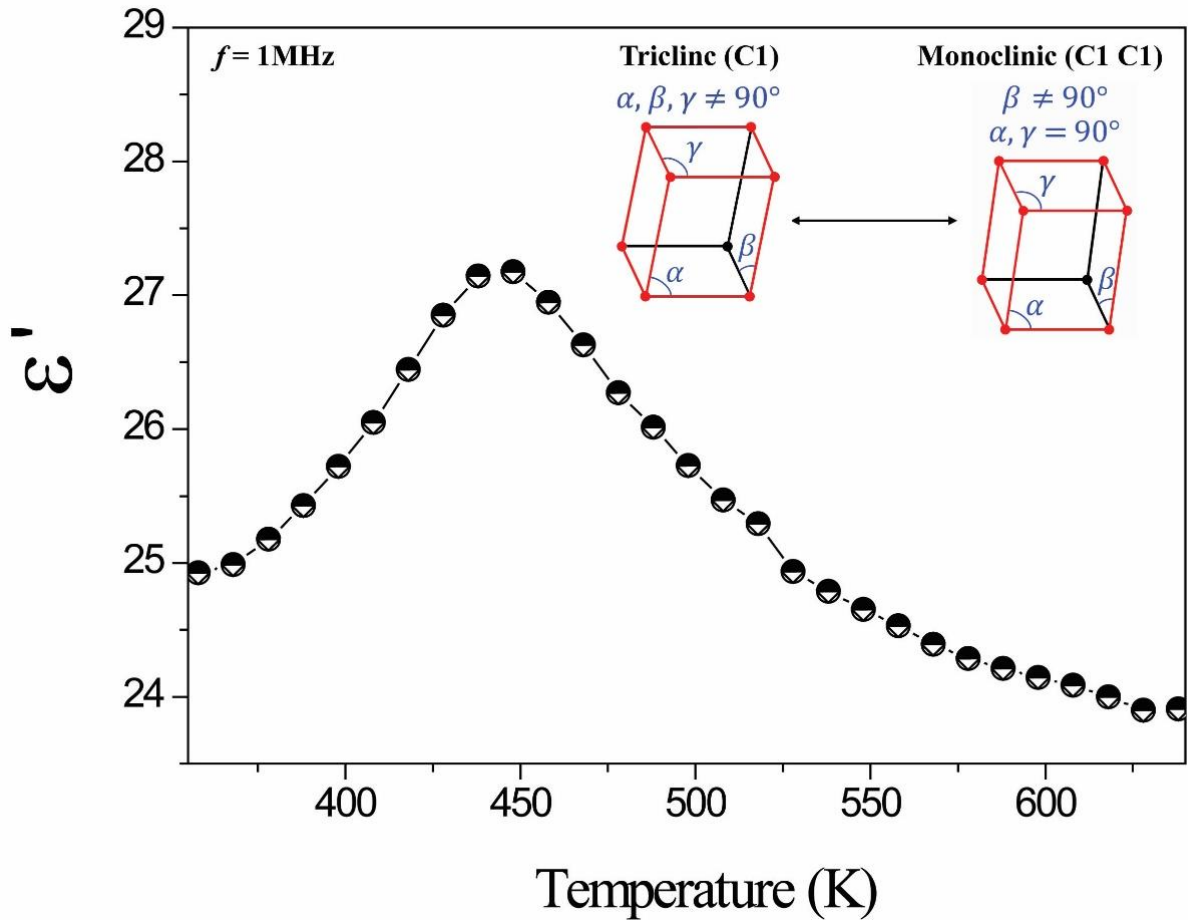
Source: Author.

       The dielectric characterization in the radiofrequency region as a function of the temperature (298-718 K) was used to investigate the changes in the dielectric behavior of the material. Figures 7 (a) and (c) present the ε' profile and show two behavior before and after the transition temperature (445 K). Before the phase transition, ε' values presented a decrease behavior when the temperature increases, as demonstrated by values of Temperature coefficient of capacitance (TCC).

Figure 7 - Dielectric spectra at 298-718 K: (a) and (c) for ε'; and (b) and (d) for tan δ.
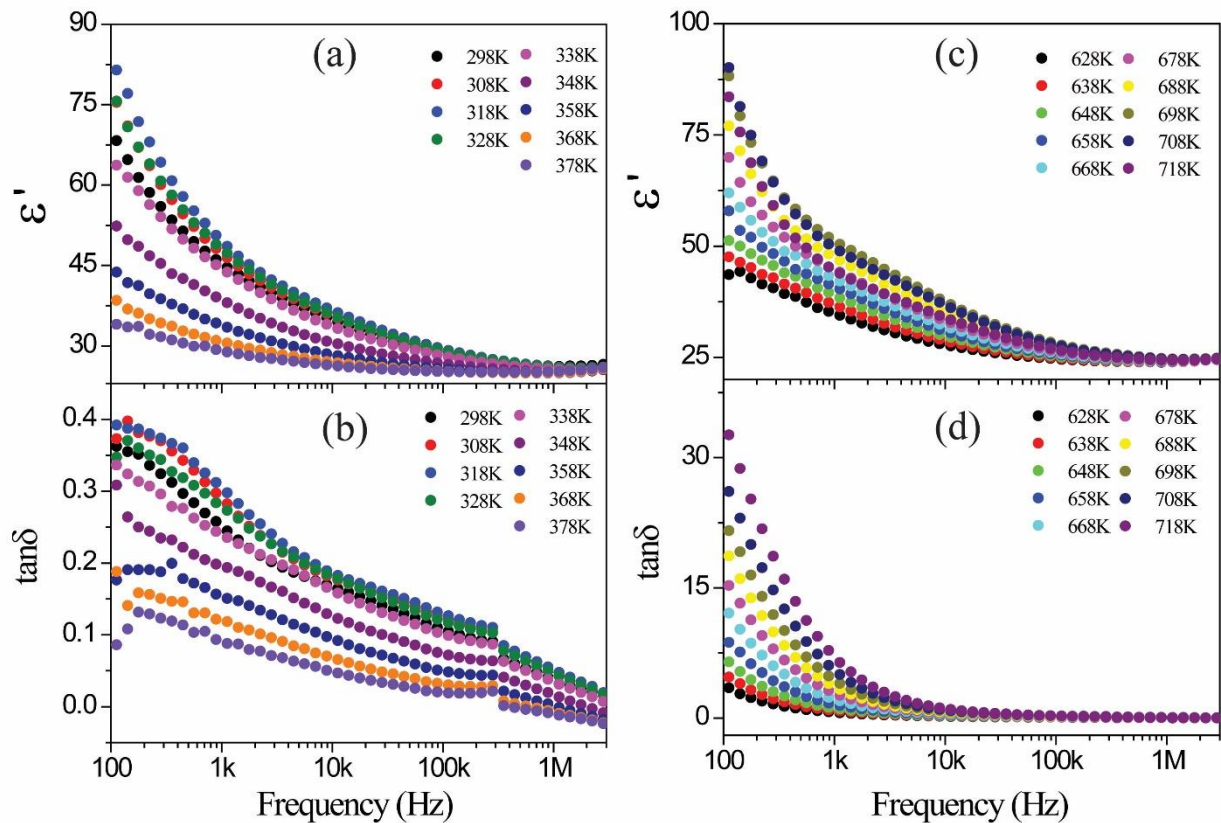
Source: Author.

This behavior is probably due to the triclinic SWO, where negatives values were obtained (Table 3). After transition temperature, the dielectric permittivity increases proportionally with the temperature. In this case, positive values of TCC can be obtained and shows the characteristics of monoclinic SWO. These values can be explained by increasing of polarization with the change of symmetry of SWO with increasing of temperature, where the highest temperature promotes a higher polarization (KOOPS, 1951) or increasing of conductivity due to the mechanism of conduction activated by temperature. The tan δ profile (Figures 7 (b) and (d)) presents similar behavior when compared to ε' values.

Table 3 – Temperature coefficient of capacitance (TCC) of the SWO at 100, 1k, 100k and 1MHz.

Frequency (Hz)	TCC (ppm.°C^{-1})
100	-6156.52
1 k	-4474.66
100 k	-1539.27
1 M	-471.73

Source: Author.

Some process activated by temperature are analyzed by shift of maximum frequency in the M'' *(f)*, ε'' *(f)*, Z'*(f)* diagrams or by conductivity with temperature variation. Figures 8 (a), (b) and (c) show measurements of alternating current electric conductivity real part (σ'_{ac}), M'' and Z'' as a function of the temperature (after phase transition, 608-718K). The Activation energy (E_a) for this thermo-activated process was calculated by shifting frequency of maximum frequency and the values for this thermo-active process were about 1.3 eV. Some double perovskites present smaller values than SWO, as ($La_2Co_{1+x}(Mg_yTi_{1-y})_{1-x}O_6$ (E_a = 0.77-0.81eV) (SHAFEIE *et al.*, 2015), $BaPrCoTaO_6$ (E_a = 0.35-0.38eV) (BHARTI *et al.*, 2014b), $BaLaMnSbO_6$ (E_a = 0.49-0.51eV) (BHARTI *et al.*, 2014), Sr_2CeTaO_6 (E_a = 0.78eV) (BHARTI; CHANDA; SINHA, 2013), $BaPrCoNbO_6$ (E_a = 0.4eV) (BHARTI *et al.*, 2014a) and $Sr_2MgMoO_{6-\delta}$ (E_a = 0.52 and 1.43 eV) (MARRERO-LÓPEZ *et al.*, 2009). Therefore, the thermo-active process requires more energy for SWO. The analysis of the E_a by three different methods showed values very close to each other and they are indicative of the same phenomenon.

Figure 8 - E_a obtained by temperature shift: (a) σ'_{ac}, (b) M" and (c) Z".
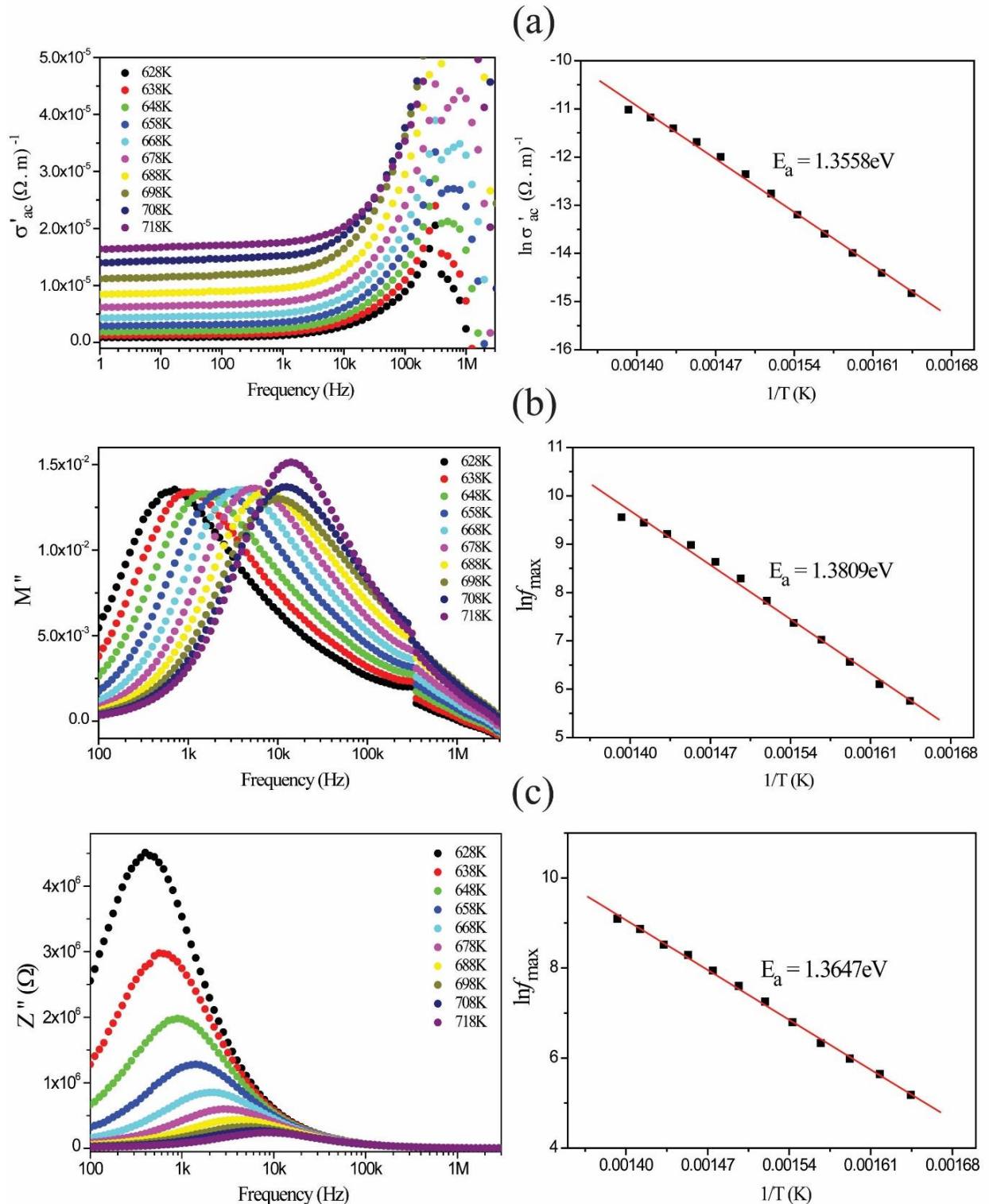
Source: Author.

The global dielectric and electric properties in the ceramic may be sum of contributions as electric and/or dielectric response provide by grain, grain boundary or electrode. The analysis of Nyquist diagram enables the visualization of this contribution. This

model can be seen by fitting with equivalent circuit method or by models (Cole-Cole, Cole-Davidson etc). The impedance measurements showed the presence of semicircle, where these results were fitted by equivalent circuit model. Although of this results show only one semicircle, it was necessary to use two associated RC for best fitting. Figure 9 (a) demonstrates the experimental and obtained Nyquist diagram following this methodology. The fittings presents good correlation with experimental data. Figure 9 (b) shows the equivalent circuit for SWO, where it can be seen two resistor–capacitor (RC) circuit. They are associated with the grain (C_g and R_g) and grain boundary (C_{gb} and R_{gb}) of the ceramics. In these associations were utilized Constant Phase Element (CPE) instead of Capacitance and it is well justified by increasing of conductivity of ceramic with temperature and the impedance values decreasing with temperature.

Table 4 summarizes the fitting value of parameters used in equivalent circuit. The R, P and N parameters were obtained by fitting and presents different values, dependent on the temperature. For example, the resistances R_1 and R_2 decrease when the temperature increase due to the increased conductivity. However, the N parameter decreased with temperature, since the material becomes more conductive and the capacitive characteristic ceases. The parameter are marked by subscript numbers 1 and 2. They are assigned to grain and grain boundary parameters, respectively.

Figure 9 - (a) Nyquist diagram at 608-718 K and fits obtained and (b) equivalent circuit based in the experimental data.
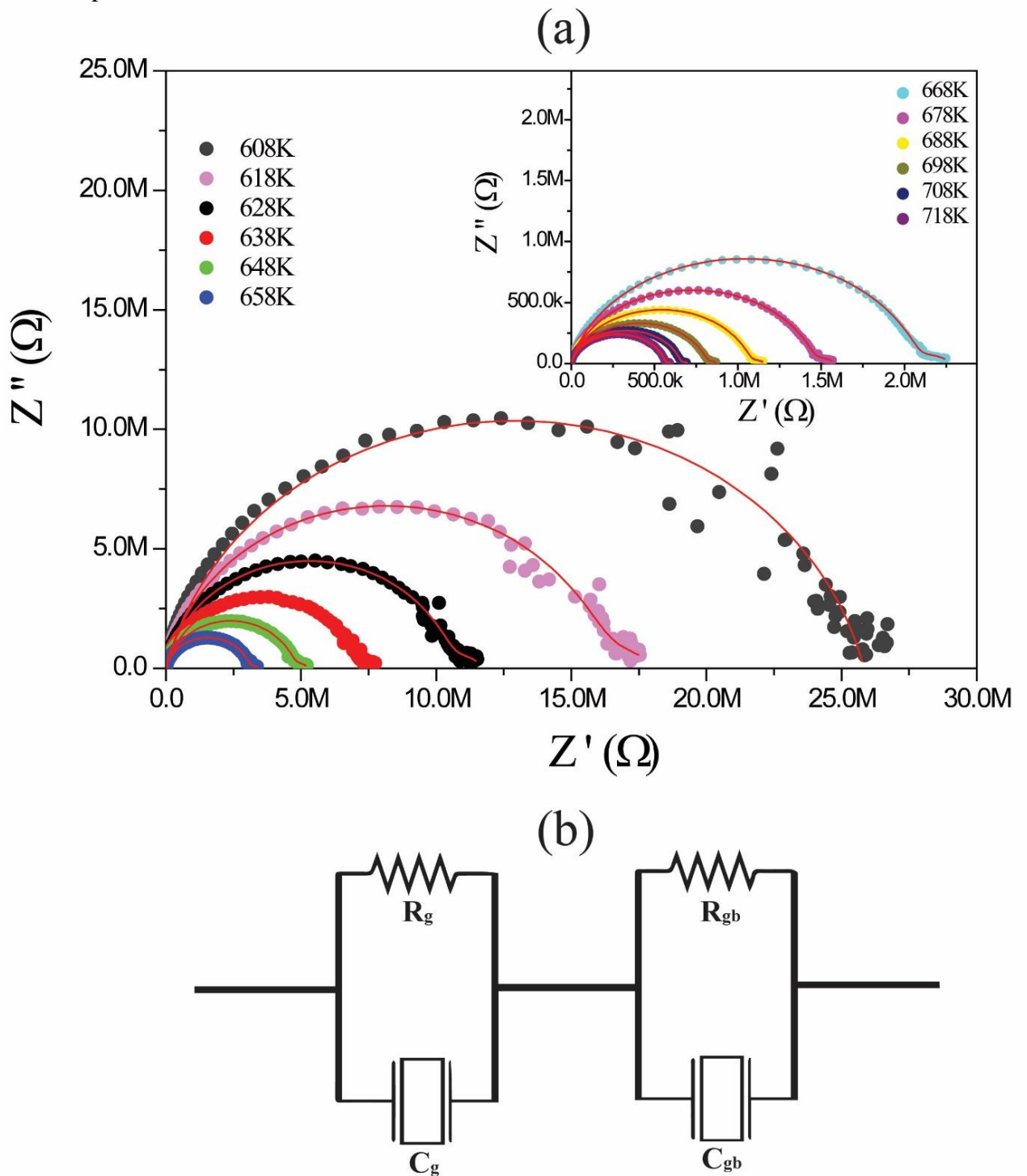
Source: Author.

Table 4 – Fitting of equivalent circuit parameters for SWO.

T(K)	Grain			Grain Boundary		
	$R_1 (\Omega)$	P_1	N_1	$R_2 (\Omega)$	P_2	N_2
608	2.71×10^6	9.32×10^{-8}	0.692	2.50×10^7	8.26×10^{-11}	0.883
618	2.26×10^6	7.61×10^{-8}	0.563	1.59×10^7	8.39×10^{-11}	0.888
628	1.30×10^6	9.56×10^{-8}	0.645	1.05×10^7	8.13×10^{-11}	0.896
638	1.17×10^6	2.64×10^{-7}	0.453	6.97×10^6	8.41×10^{-11}	0.897
648	5.57×10^5	1.80×10^{-7}	0.620	4.73×10^6	1.00×10^{-10}	0.884
658	3.49×10^5	3.30×10^{-7}	0.579	3.08×10^6	1.07×10^{-10}	0.882
668	2.07×10^5	5.02×10^{-7}	0.602	2.07×10^6	1.17×10^{-10}	0.877
678	1.42×10^5	6.60×10^{-7}	0.569	1.45×10^6	1.20×10^{-10}	0.878
688	9.96×10^4	1.12×10^{-6}	0.514	1.07×10^6	1.32×10^{-10}	0.875
698	6.83×10^4	1.45×10^{-6}	0.534	8.10×10^5	1.53×10^{-10}	0.867
708	4.83×10^4	2.68×10^{-6}	0.524	6.54×10^5	1.33×10^{-10}	0.877
718	3.85×10^4	3.35×10^{-6}	0.498	5.62×10^5	1.00×10^{-10}	0.895

Source: Author.

In microwaves range (7.84 GHz), the SWO shows high $\varepsilon' = 13.57$ and $\tan \delta = 0.0281$. This dielectric characterization was performed by Hakki-Coleman method, where was analyzed the TE011 mode of the cylindrical resonator. The dielectric properties demonstrated good agreement with results obtained in IS.

The Temperature coefficient of resonant frequency (τ_f) for SWO, i.e., the dielectric properties variation with increasing temperature was measured by the SFS method (SILVA *et al.*, 2012). The τ_f was measured by monitoring of displacement mode HE11δ frequency with increasing of temperature (Figure 10 (a)) and the linear correlation of temperature and HE11δ frequency was observed (Figure 10 (b)). It is possible to observe that with the increase of temperature the mode $f_{HE11\delta}$ shifts to smaller frequency. The linear fit with the experimental points were used to calculate τ_f (-207.60 ppm.K^{-1}). SWO shows an improbable τ_f values when compared to the results from other materials, where in the literature other double perovskites presented values below 25 ppm.K^{-1} (BIAN *et al.*, 2008, 2015; WU; BIAN, 2012; VASALA; KARPPINEN, 2014; GANDHI; KESHRI, 2015; BIAN; WU, 2016).

Figure 10 - (a) Displacement of mode $f_{HE11\delta}$ with variation of temperature and (b) τ_f of SWO.
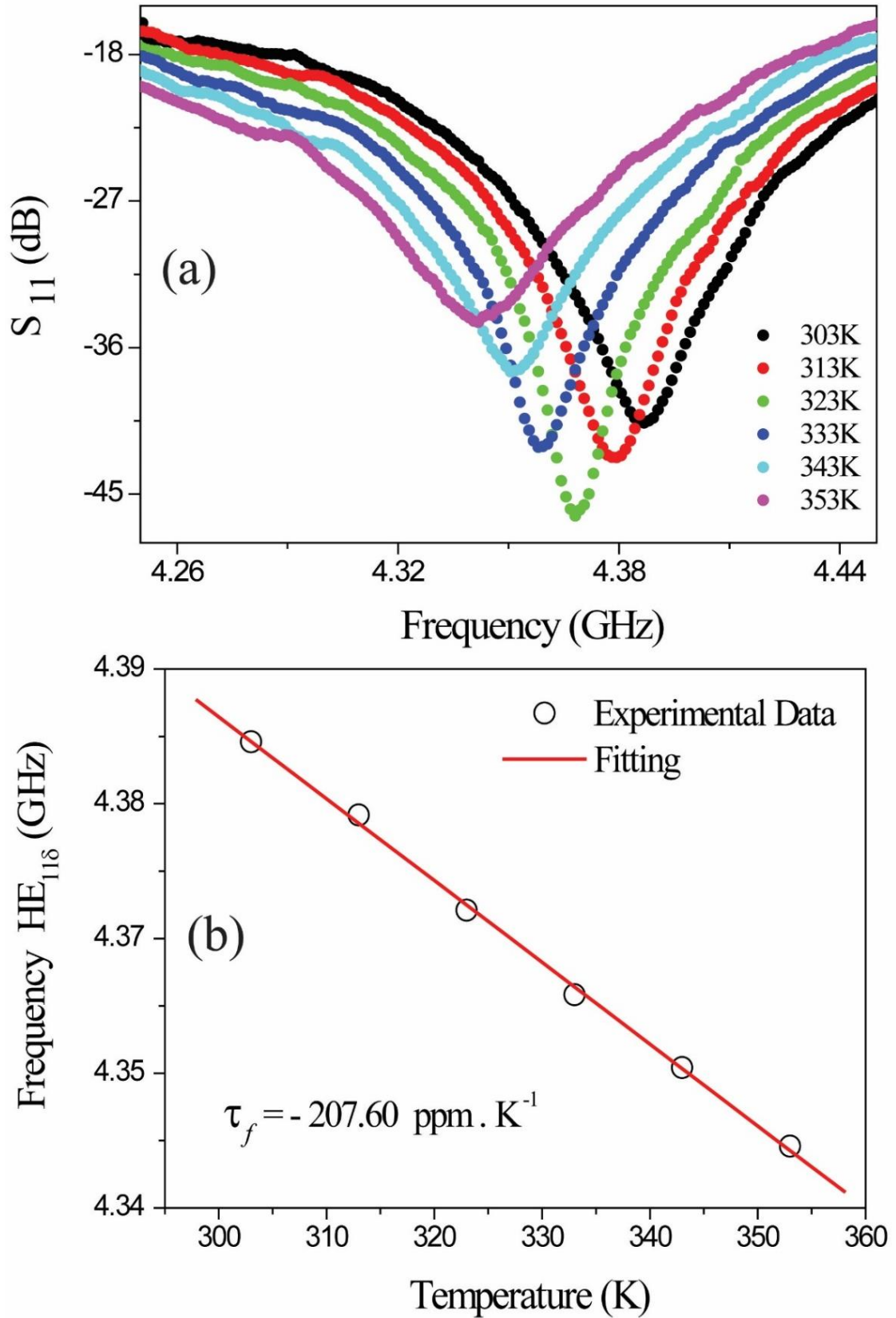
For the microwave applications, SWO dielectric resonator was analyzed in the antenna setup (Figure 4). From this experiment was possible to obtain the main parameter for evaluating the antenna device: return loss (S_{11}), bandwidth and by numerical simulation in HFSS software. The far field parameters were also obtained as radiation patterns, gain and efficiency of antenna. For the first analysis, the return loss (Figure 11 (a)) presented by SWO–based DRA shows $f_{HE11\delta}$ in 4.12 GHz and S_{11} (-43.96 dB) below -10dB, and presents a good coupling and operating as an antenna (Error = 0.75%), as shown in Table 5. Figure 11 (a) also shows a good agreement between experimental and simulated return loss obtained by numerical simulation and collected data. This condition is necessary for acquisition of accurate far field's parameters.

Table 5 – Antenna parameters of the SWO dielectric resonator.

	SWO–based DRA		
	Experimental	Simulated	Error (%)
$f_{HE11\delta}$	4.1256	4.1260	0.010
S_{11} (dB)	-43.97	-43.64	0.753
BW (%)	7.268	7.053	2.958
Efficiency (%)		57.90	
Peak resonant resistance (Ω)	108.125	107.155	0.896
Resistance (Ω)	49.702	50.280	1.163
Directivity (dBi)		3.41	
Gain (dBi)		1.98	

Source: Author.

For validation of the numerical simulation, it is necessary a good agreement of return loss and impedances or Smith chart with experimental data. Figure 11 (b) shows experimental and simulated Smith chart. Both presents inductive characteristics and the simulated results presents minor deviations from experimental data. Table 5 summarizes the results obtained by simulations and experimental data, where the DRA presents a bandwidth of 7 % or 287 MHz. These results are consistent for DRA characteristics. The gain (1.98 dBi) and efficiency (57.90 %) obtained in simulation shows small values compared with another DRAs in the literature (ALMEIDA *et al.*, 2008; PEREIRA *et al.*, 2010; ROCHA *et al.*, 2012; SILVA *et al.*, 2014; OLIVEIRA *et al.*, 2015). However, these parameters can be improved by a better coupling between DRA and SMA probe in the antenna device.

Figure 11 - (a) Experimental and simulated S_{11} and (b) Smith Chart of the SWO--based DRA;
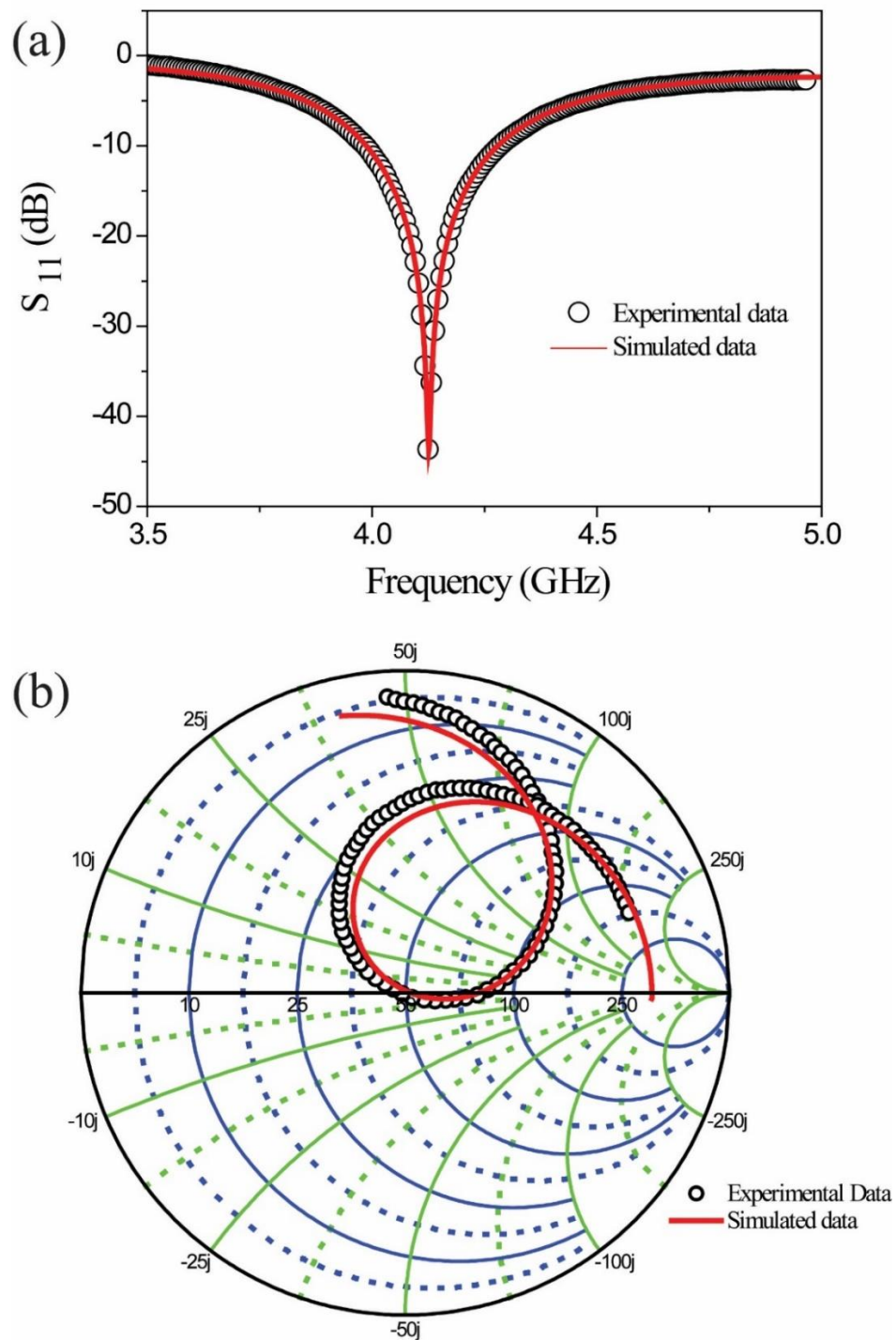
Source: Author.

The radiation profile of DRA is showed in the Figure 12. One can observed the cylindrical dielectric resonator involved by a simulated radiation patterns. The inset of the

Figure 12 shows that the radiation pattern profile is consistent with a cylindrical DRA, with maximum radiation for $\Theta = 0°$ when analyzed by $\varphi = 90°$ and $\varphi = 0°$.

Figure 12 - Radiation profile for DRA. Diagram inset shows radiations in function of Θ and φ.
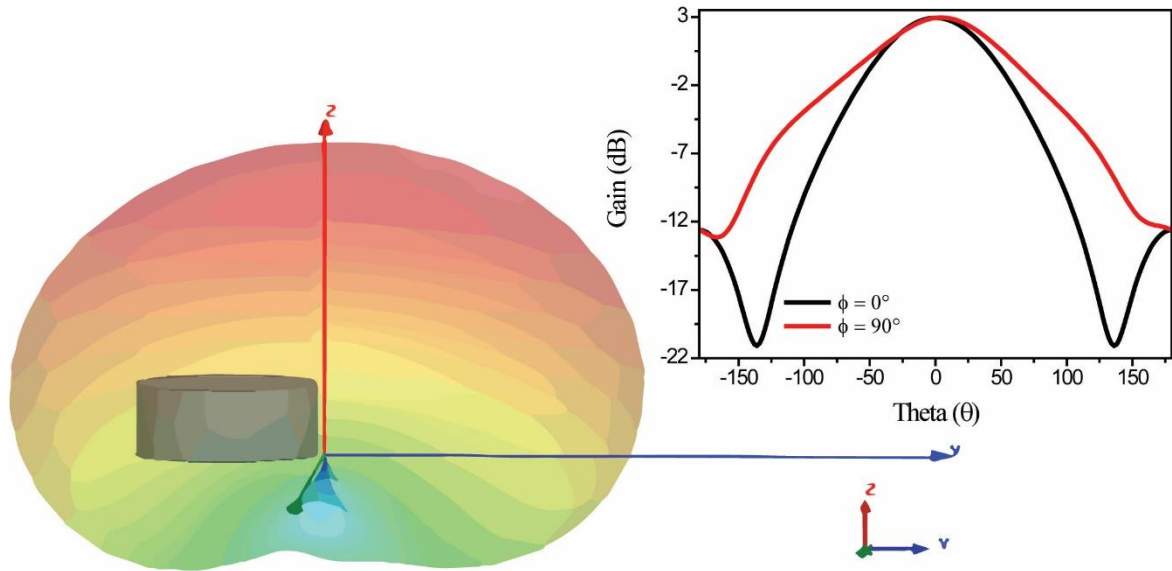
Source: Author.

These results shows an antenna device with a good gain and an appreciable efficiency operating at 4.12 GHz. In this sense, to create a device available for Wi-Fi devices (5.15-5.875 GHz)(BT. ISMAIL *et al.*, 2012) using SWO-based DRA, for example, requires a miniaturization process of this antenna, once the $f_{HE11\delta}$ is a function of dimensions and dielectric properties (see equation 3). The better coupling of this novel resonator with the coaxial feed presents gain values closer of commercial antennas (2-3dBi for residential users). In addition, due to isolating characteristics (higher *Ea* and impedance ($Z > 1$ GΩ), higher stable dielectric ($200 <$ TCC -5600 ppm $°C^{-1}$) and low dielectric permittivity, the SWO ceramic also can be applied in devices than needs of dielectric Class 1 (HIPPEL, 1954; MOULSON, A J; HERBERT, 2003).

2.4 Conclusion

The SWO phase was obtained by solid state route and the temperature of synthesis was below that of other works (KING *et al.*, 2010)(DRACHE *et al.*, 1981) due to

the previous grinding treatment (activating powder). Dielectric studies showed that SWO presents a transition temperature in 445 K in agreement with previous studies. SWO presented a thermo-activated process with *Ea* value around 1.35 eV, while showed negative values of TCC. The Nyquist diagrams were well fitted by two associations of R-CPE and the SWO-based DRA presented applicable as microwave antenna. τ_f value for SWO resonator was -207.60 ppm·K^{-1} and it is a novel option to be used in association with another phase with positive τ_f values for composite materials to achieve zero τ_f values. The results are important for development of devices that operate in microwaves range, although dielectric properties are frequency-dependent. For example, devices for telecommunications operates in microwaves range as wireless antenna, Bluetooth and mobile system. The SWO phase can be also used as dielectric substrates to fabricate microstrip patch antennas. The dielectric ceramic enables miniaturization of this antennas possibility miniaturization of this device and weight reduction.

3 PROPERTIES OF THE Sr_3MoO_6 ELECTROCERAMIC FOR RF/MICROWAVE DEVICES

3.1 Introduction

Ceramic materials based on double perovskite-type structure have been studied due to their magnetocaloric (CHAKRABORTY *et al.*, 2017; HUSSAIN *et al.*, 2017), magnetic (KOBAYASHI *et al.*, 1998; KAYSER *et al.*, 2017; AHMED *et al.*, 2017; TIITTANEN; KARPPINEN, 2018; HOSSAIN *et al.*, 2018), photoluminescent (LI, L. *et al.*, 2017; WANG *et al.*, 2017; LI *et al.*, 2018; ZHANG *et al.*, 2018), photovoltaic (SLAVNEY *et al.*, 2016; ZHOU *et al.*, 2018), and multiferroic (NECHACHE *et al.*, 2011; SHARMA *et al.*, 2013; WU *et al.*, 2018) properties. Double perovskites have an $A_2B'B''O_6$ type structure in which the twelve-coordinated A sites are generally occupied by divalent cations, most commonly an alkaline earth element. However, the octahedrally-coordinated B' and B'' sites can be occupied by various ion combinations, due to the different oxidation states, thus maintaining electroneutrality in the oxide (VASALA; KARPPINEN, 2014). Some of the many diverse applications of these ceramics include photocatalysts (ZHU *et al.*, 2017), thermoelectric devices (SAXENA *et al.*, 2017), and electrodes for fuel cells (WANG *et al.*, 2016).

Many double perovskite electroceramics have been studied with IS (PANDA *et al.*, 2015; MAHATO; SINHA, 2016; HALDER *et al.*, 2017; DEHURY *et al.*, 2018) to analyze their electrical response to different frequencies. Dielectric studies of electroceramics in microwave and RF have been of great interest due to the innumerous applications in telecommunications and electronic devices.

However, most electroceramics synthesize at a high temperature in a densification process, generating an energy-consuming pathway. Therefore, a variety of materials have been developed based on the well-known LTCC technology, which has found application in the fabrication of integrated microwave devices such as resistors, inductors, and capacitors (ZHOU *et al.*, 2014; ZHU *et al.*, 2014). Sintering aids, such as MoO_3 and TeO_2, are used to lower the sintering temperature of microwave electroceramics. Considering the cost and toxicity, MoO_3 has more advantage to be used in an LTCC (ZHOU *et al.*, 2014; LIAO *et al.*, 2014).

There have been many reports about LTCC based molybdates (ZHOU *et al.*, 2011; TANG *et al.*, 2013; JOSEPH *et al.*, 2016). For example, the standard LTCC process for $(Ag_{0.5}Bi_{0.5})MoO_4$ (ZHOU *et al.*, 2011) and $(Ag_{0.5}Bi_{0.5})WO_4$ (ZHOU *et al.*, 2014) phases were studied, which showed different dielectric properties and sintering temperatures (ZHOU *et al.*, 2014). It is reported that Mo (sheelite structure) (ZHOU, DI *et al.*, 2011) and W (wolfranite structure) (ZHOU *et al.*, 2014) show ε' of ~30.4 and ~35.9, τ_f of +57 ppm.°C^{-1} and -69 ppm.°C^{-1}, and sintering temperature of 690 °C and 580 °C, respectively. It is noted that the change of W for Mo provided different structures and opposite τ_f values. In our previous work (PAIVA et al., 2016), we investigated SWO double perovskite as a potential DRA. The similarly between Mo^{6+} and W^{6+} ionic ratio and oxidation state allows the formulation of new LTCCs based structures mixing Mo^{6+} and W^{6+} ions (ZHOU *et al.*, 2014). However, to our knowledge, the influence of Mo^{6+} on dielectric properties, sintering temperature and DRA application have never been reported for SMO electroceramics. Actually, few studies examine the properties of SMO double perovskite, such as the red phosphors $Sr_3MoO_6:Eu^{3+}$ applied in the white light emitting diode (JING *et al.*, 2015).

Compared to other antenna devices, DRAs have lower weight, cost and size, higher radiation efficiency, and easier manufacturing, including with different geometries (cylindrical, rectangular, half-hemispherical etc.) and feedings (slots, probes, waveguides etc.). A DRA converts a wave propagation on a transmission line to a plane wave propagation in free-space (transmission or reception) (BONDARENKO; RAGOISHA, 2005). The development in DRA technology has been influenced by growing use of the microwave range in the telecommunication field (PARIDA *et al.*, 2012). Dielectric resonators are also used in microwave circuits (oscillators and filters) and satellite communication.

In this chapter, the synthesis of the SMO electroceramic by solid-state reaction is reported. The crystalline phase and microstructure were studied by PXRD, SEM and EDS. For dielectric characterization at RF, IS was performed as a function of temperature. Impedance and radiation properties of the SMO dielectric resonator were studied as a DRA (SMO-based DRA) through experimental measurements and numerical simulation. The present study allows the possibility of application of the SMO electroceramic in microwave and RF devices.

3.2 Experimental methods

SMO electroceramic was synthesized by a solid-state reaction between $SrCO_3$ (97%, Vetec) and $MoO3$ (99.9%, Vetec). These starting materials were mixed using a mortar and pestle in stoichiometric amounts, and then the powder was milled for 2h at 370 rpm in a Fritsch Pulverissette 6 planetary mill. The obtained products from the milling process were calcined in air for 6 h, isothermally between 973 K and 1523 K, in order to determine the best calcination temperature for the synthesis. The chemical reaction occurring during calcination can be summarized as:

$$3SrCO_3(s) + MoO_3(s) \rightarrow Sr_3MoO_6(s) + 3CO_2(g) \tag{4}$$
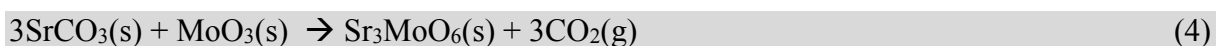
For dielectric measurements, the SMO powder was uniaxially pressed into a steel die to form pellets and cylinders of the electroceramic. The ceramics were sintered in two steps: 773 K for 2h and then 1523 K for 6h, in air. After this process, both sides of the sintered disk were polished, and a silver paste was applied to ensure electrical contact. The dimensions of the samples for dielectric measurements were: 15.94 mm diameter, 9.61 mm thickness, for microwave range (dielectric resonator); and 15.76 mm diameter, 1.79 mm thickness, for the RF ranges.

PXRD profiles were obtained by using a PANalytical diffractometer (Xpert Pro MPD) operating at 40 kV and 45 mA in the geometry Bragg-Brentano, with a Cu tube (Kα1 = 1.540562 Å, Kα2 = 1.54439 Å). The diffraction patterns were collected at room temperature (~300 K) from crushed SMO samples. They were obtained from 15° to 65° (2θ) with a step size of 0.013°, with an analysis time at each step of 70 s, using graphite monochromator for diffracted beam.

Micrograph images were obtained by SEM FEG Quanta 450 with EDS, in order to observe the microstructure of the sintered electroceramics. The sample was metalized with gold by the Metalizator Quorum QT150ES. 10 Pa of pressure was applied in the SEM chamber, with an incident electron beam of 20 kV.

For dielectric measurements at the RF range, the sample was evaluated using a Solartron 1260 computer-controlled impedance analyzer as a function of frequency (1 Hz to 1 MHz) at different temperatures (298 K–708 K). On the other hand, the dielectric measurements for the microwave range were evaluated by the impedance analyzer of Agilent

Model PNA N5230A with the Hakki-Coleman method (HAKKI; COLEMAN, 1960). Agilent PNA N5230A was also used to measure the S_{11} and impedance of the SMO-based DRA at room temperature.

Further, the setup of antenna measurements consisted of the electroceramic cylinder under a ground plane (copper plate) and the SMO-based DRA was fed by an SMA probe. The investigation of SMO-based DRA was performed by numerical simulation, using the HFSS of Ansoft, in order to validate the experimental results.

3.3 Results and discussion

To ensure complete calcination and thus the crystalline phase, the PXRD patterns of the samples were compared to that of the SMO crystalline phase (JCPDS nº 027-1441) (JING *et al.*, 2015). SMO double perovskite has a cubic structure ($\alpha = \beta = \gamma = 90°$) and belongs to the space group Fm-3m (225), with lattice constant (a = b = c) equal to 16.39 Å (see Figure 13) (MCCARTHY; GOODEN, 1973; JING *et al.*, 2015). The PXRD patterns for the samples obtained by a solid-state reaction at a low temperature (973 K, 1073 K and 1223 K) presented peaks of the starting materials and other phases (see Figure 14), which corresponds to a lack of calcination from the low synthesizing temperature. Figure 15 (a) shows the PXRD patterns of SMO calcinated at 1323 K, 1423 K and 1523 K; at 1323 K, there are weak peaks from the $SrMoO_4$ secondary phase ($2\theta = 27.53°$, $38.24°$ and $43.57°$), thus, this temperature is not high enough to obtain the single SMO phase. Samples synthesized at 1423 K and 1523 K have diffraction planes which show a good match to the SMO database phase (JING *et al.*, 2015), demonstrating good calcination. Therefore, as the sample obtained at 1423 K requires less energy to form the pure phase, this was chosen for further experiments. This temperature is lower than for the solid-state reaction in which SMO usually is formed (1533 K) (JING *et al.*, 2015), due to the high-energy involved in the ball milling process; the temperature of the calcination reaction decreases as a function of mechanical activation (GOMEZ-YAÑEZ *et al.*, 2000; OZER; KILIC, 2017).

Figure 13 – Crystal structure of Sr_3MoO_6.
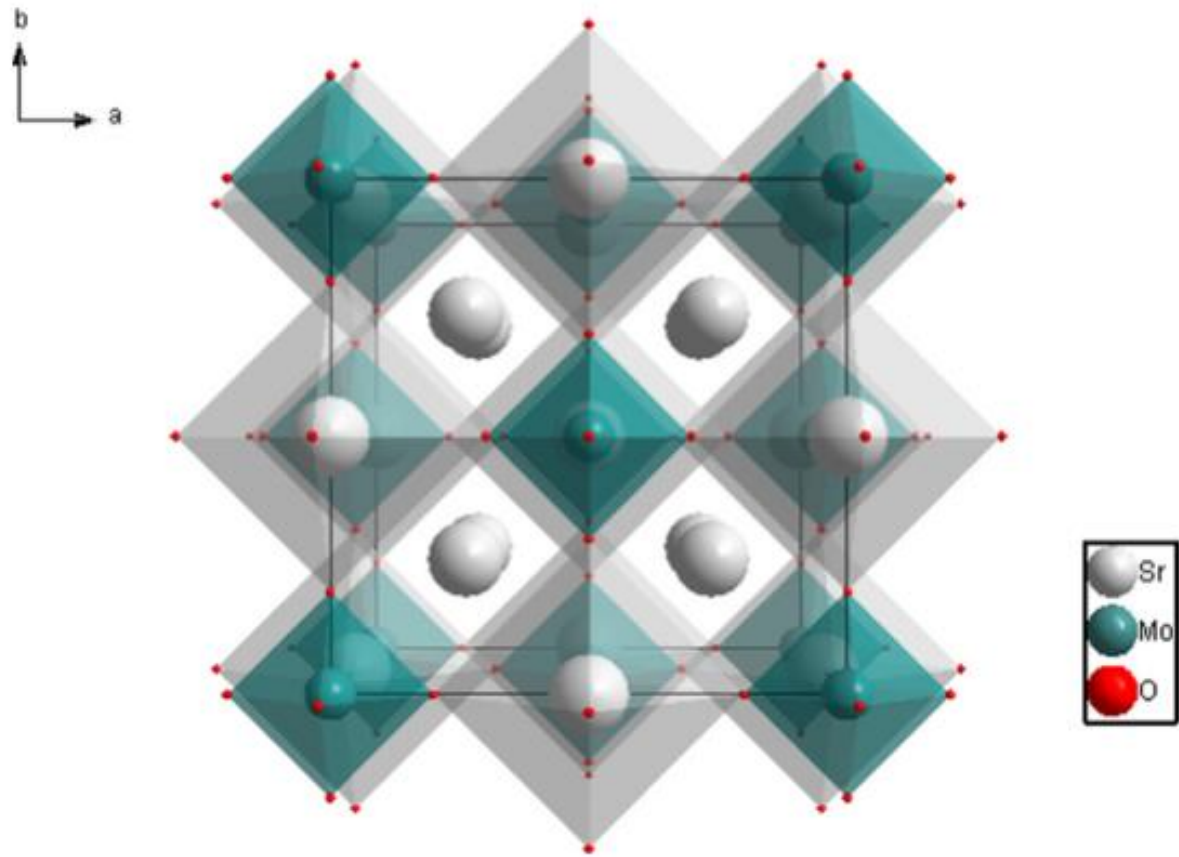
Source: (JING *et al.*, 2015).

The superficial morphology and the elemental composition of the SMO electroceramic (calcined at 1423 K) were assessed using SEM and EDS (Figures. 15 (b) and (c), respectively). Figure 15 (b) shows a Secondary electron (SE) image at an amplification of 10,000x, in which homogeneous grains with a globular shape can be clearly observed. The inset in Figure 15 (c) shows the elemental X-ray map of the same region. Additionally, X-ray energies of the selected elements (Sr, Mo and O) show the expected composition of the sample; there are no impurities.

Figure 14 (a) Comparison of the diffraction pattern database (PDF#00-027-1441) with the experimental diffractograms obtained from different calcination temperatures (973K, 1073K, 1223K); (▲) and (▲) represents SrMoO4 and SrCO3 impurities, respectively.
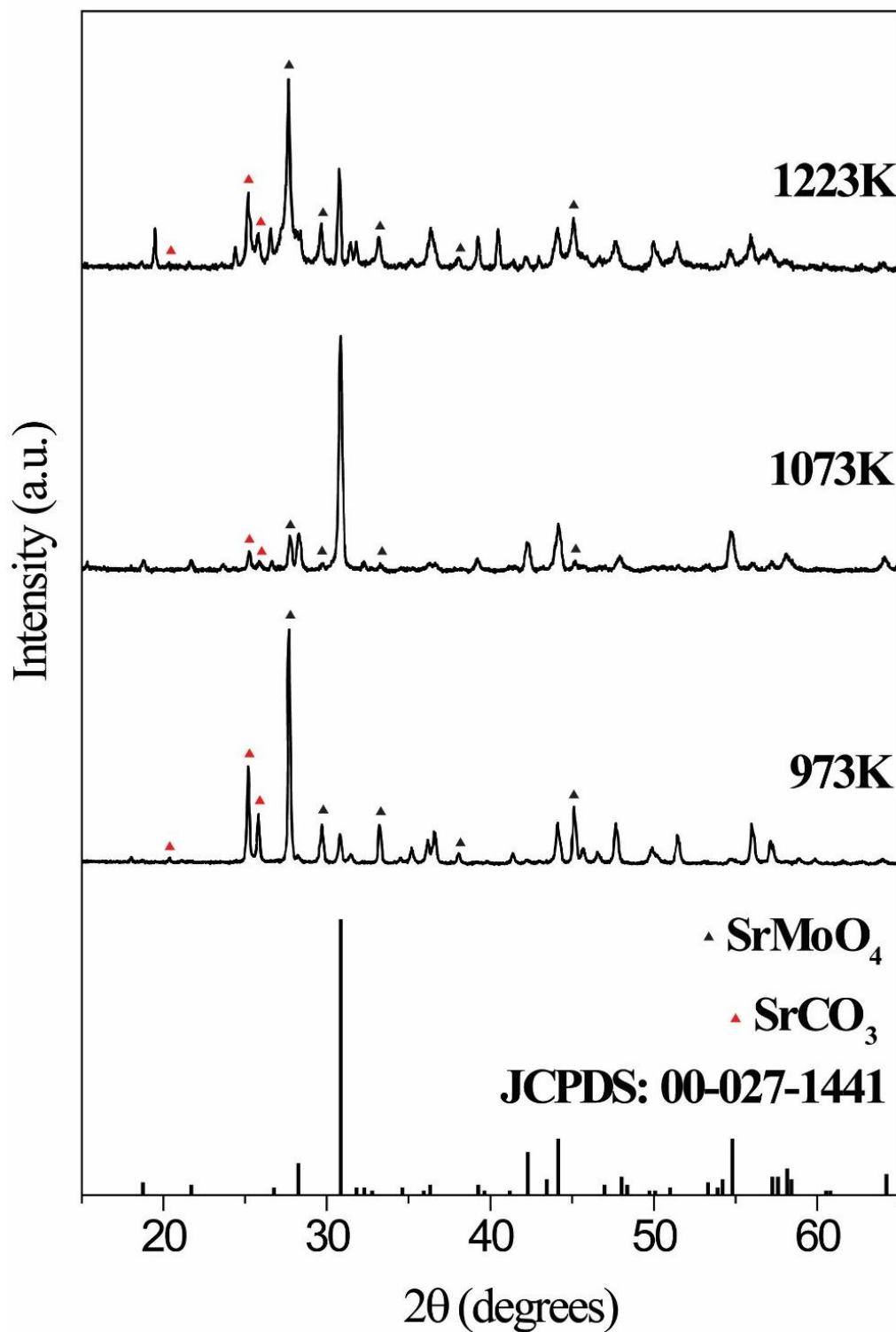
Source: Author.

Figure 15 - (a) Comparison of the diffraction pattern database (JCPDS nº 027-1441) with the experimental diffractograms obtained from different calcination temperatures (1323 K ((▲) represents SrMoO₄ impurities), 1423 K and 1523 K), (b) SEM micrograph of SMO synthesized at 1423 K an amplification of 10,000x, and (c) EDS spectrum and elemental X-ray map (inset) of SMO obtained at 1423 K; (*) represents (Au) gold from the metalization.
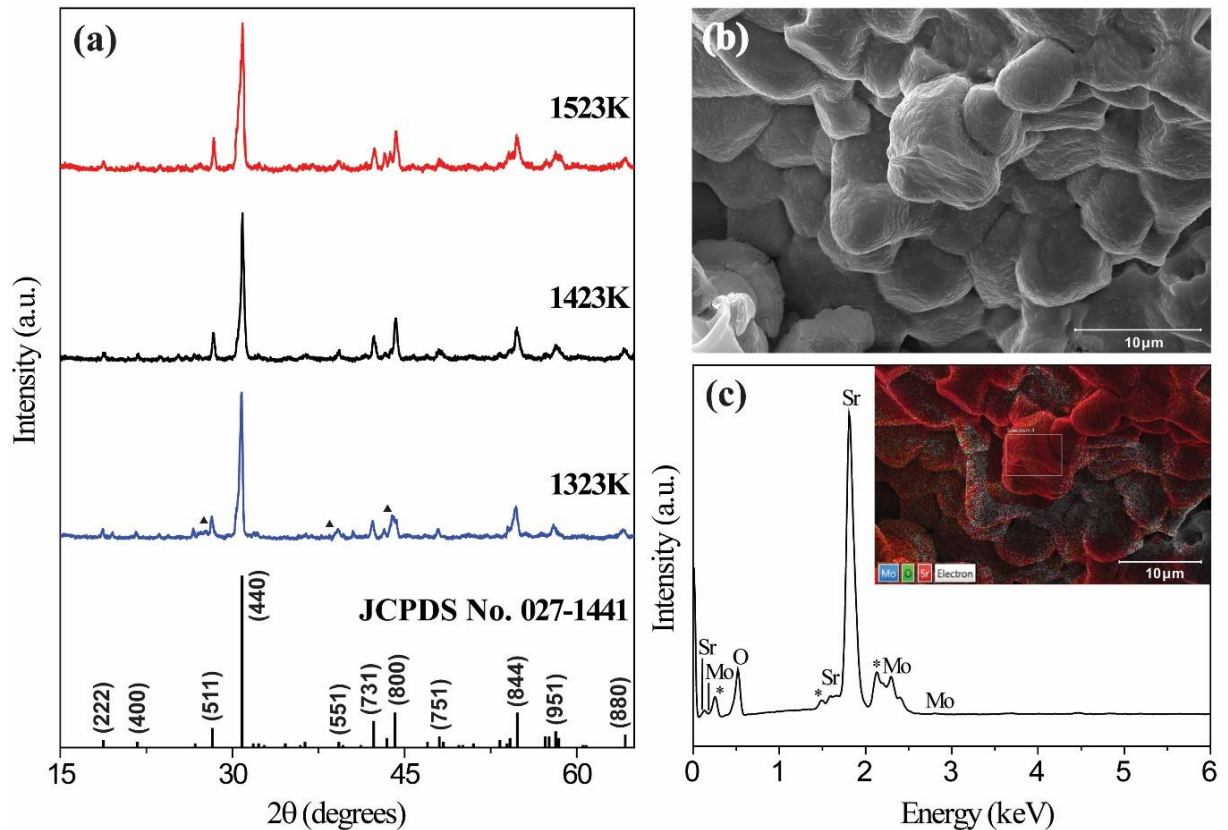
Source: Author.

Dielectric characterization in the RF range is the best way to explore the possibility of application in electronic devices, such as capacitors and filters (MOULSON, ANTHONY J; HERBERT, 2003). For this purpose, IS was used to investigate two important characteristics: the relaxation process and the thermal activation process. Figures 16 (a) and (b) show the ε' and tan δ as a function of temperature (298−708 K) in the range of 100 Hz to 1 MHz. For a better understanding of the parameters, Figures 17−20 shows ε' and tan δ values up to 5 MHz. Both ε' and tan δ values decrease as a function of frequency, due to dielectric relaxation and the electrode effect, but they also tend to increase when the temperature of the system rises. ε' values for SMO are smaller than those previously found for SWO (PAIVA *et al.*, 2016). This occurs due to replacement of W^{6+} with Mo^{6+}, which promotes a minor polarization, likely due to the change of symmetry of the double perovskite unit cell: from monoclinic (SWO) to cubic (SMO) symmetry.

Figure 16 - (a) ε' and (b) tan δ in the RF range (100 Hz–1 MHz), as a function of temperature (298 to 518 K (inset: 528–708 K)).
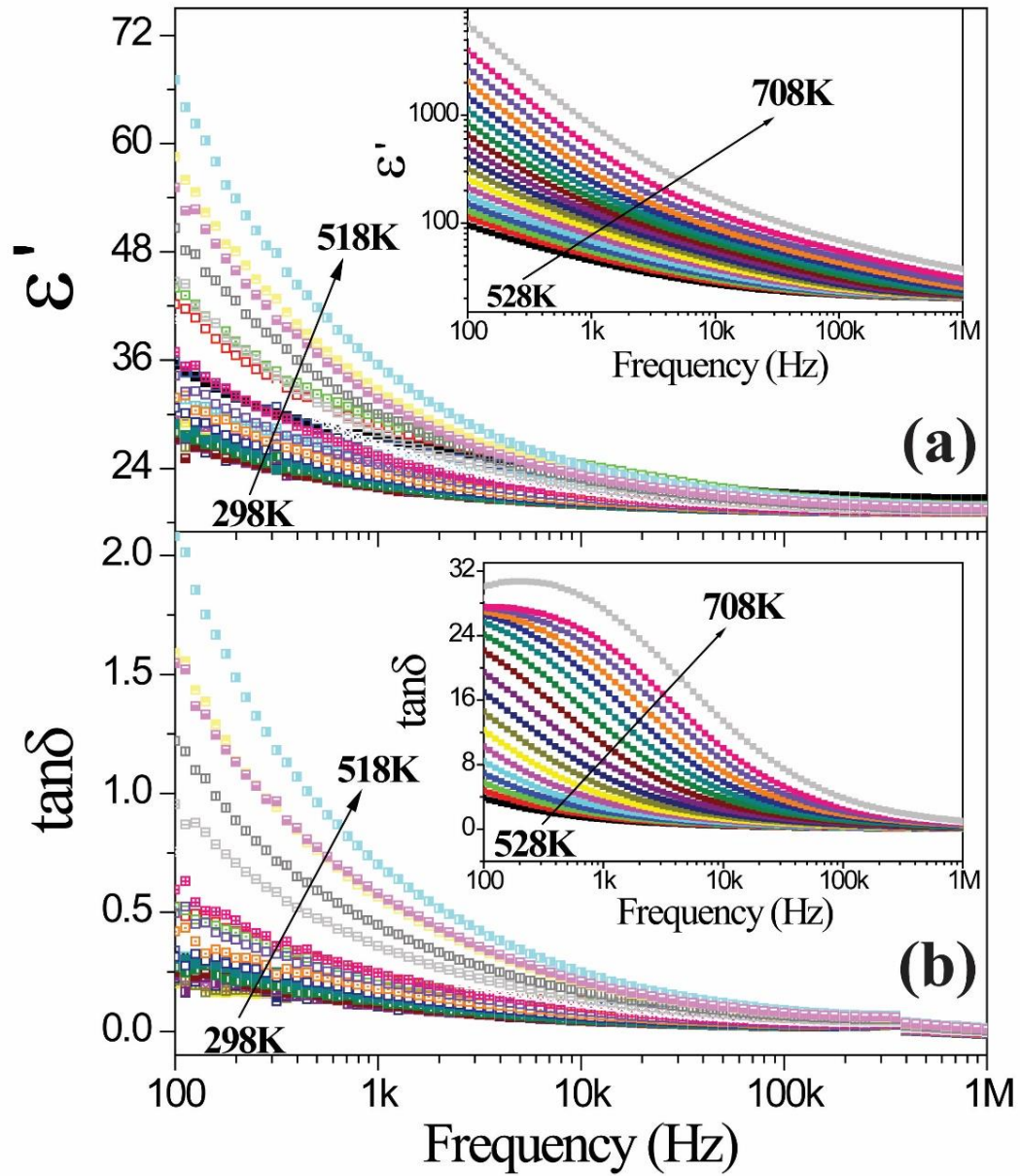
Source: Author.

Figure 17 - ε' in the RF range (100Hz – 5MHz) as a function of the temperature (298 – 518K).
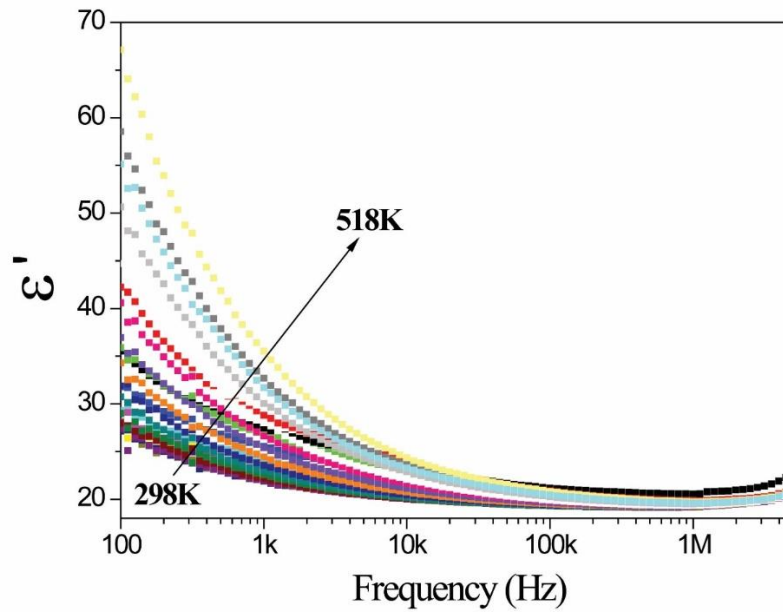
Source: Author.

Figure 18 - ε' in the RF range (100Hz – 5MHz) as a function of the temperature (528 – 708K).
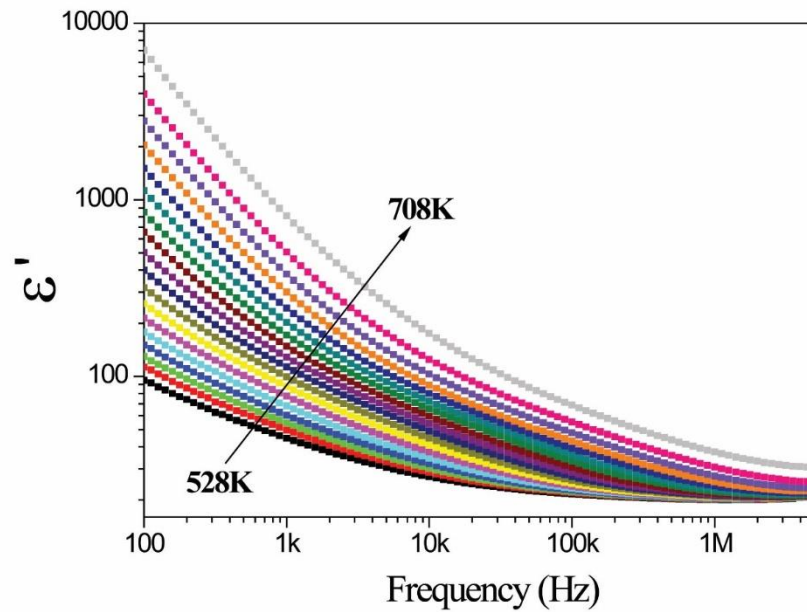
Source: Author.

Figure 19 – tan δ in the RF range (100Hz – 5MHz) as a function of the temperature (298 – 518K).
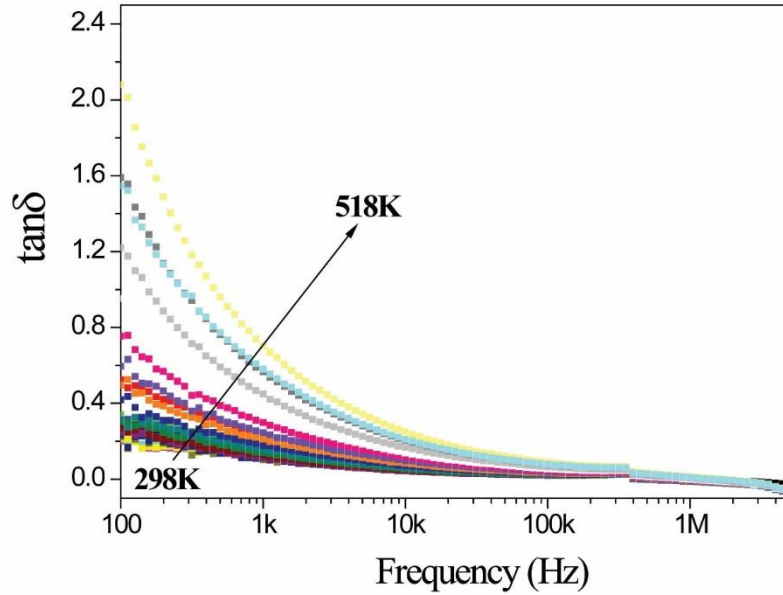
Source: Author.

Figure 20 – tan δ in the RF range (100Hz – 5MHz) as a function of the temperature (528 – 708K).
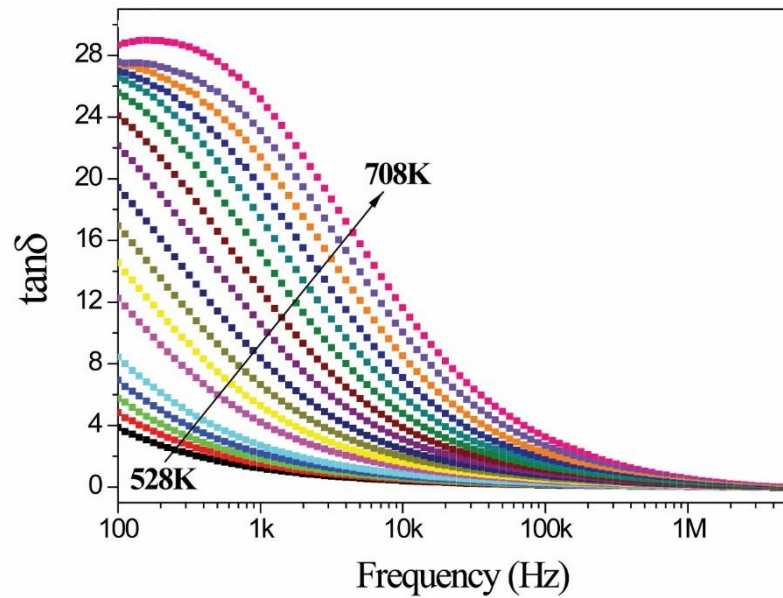
Source: Author.

As shown in Figures. 21 (a) and (b), the Z", and the M" spectra show a relaxation process occasioned by hopping of charge carriers (HALDER *et al.*, 2017). The peak of the spectrum shifts to a higher frequency when the temperature increases, suggesting a thermo-activated process occurring in the SMO electroceramic. In order to complement the study, the alternating current conductivity σ'_{ac} was assessed as a function of the temperature (Figure 21 (c)). σ'_{ac} values increase as a function of temperature due to the thermo-activated conduction in the sample. This is usually evaluated by Arrhenius' equation (ZHANG; MAK, 2012):

$$A = A_0 e^{-E_a/kT} \tag{5}$$

Where A can be the σ'_{ac}, or the frequency of the peak (f_{max}) as found in the Z" or M" spectra. A_0 is the pre-exponential factor, k is Boltzmann's constant (in electron-volts, eV), T is absolute temperature and E_a is activation energy. Figure 21 (d) illustrates the strong linear correlation between ln f_{max} and 1/T. From these plots, the E_a for SMO was calculated in three different ways: M" (1.10 eV), Z" (1.27 eV) and σ'_{ac} (1.18 eV). These values are lower than for SWO electroceramics (~1.37 eV) (PAIVA *et al.*, 2016), i.e., the conduction process occurs easier in SMO than in SWO. This temperature dependency is observed in other electric parameters, such as the imaginary parts of the ε'' and the C" Figures 22 and 23; both rise with temperature as the conduction process is thermally activated.

Figure 21 - (a) Z", (b) M", and (c) σ'ₐc, as a function of the temperature from 528 K to 708 K between 100 Hz and 1 MHz. (d) shows a graphical determination of Eₐ (Arrhenius plot).
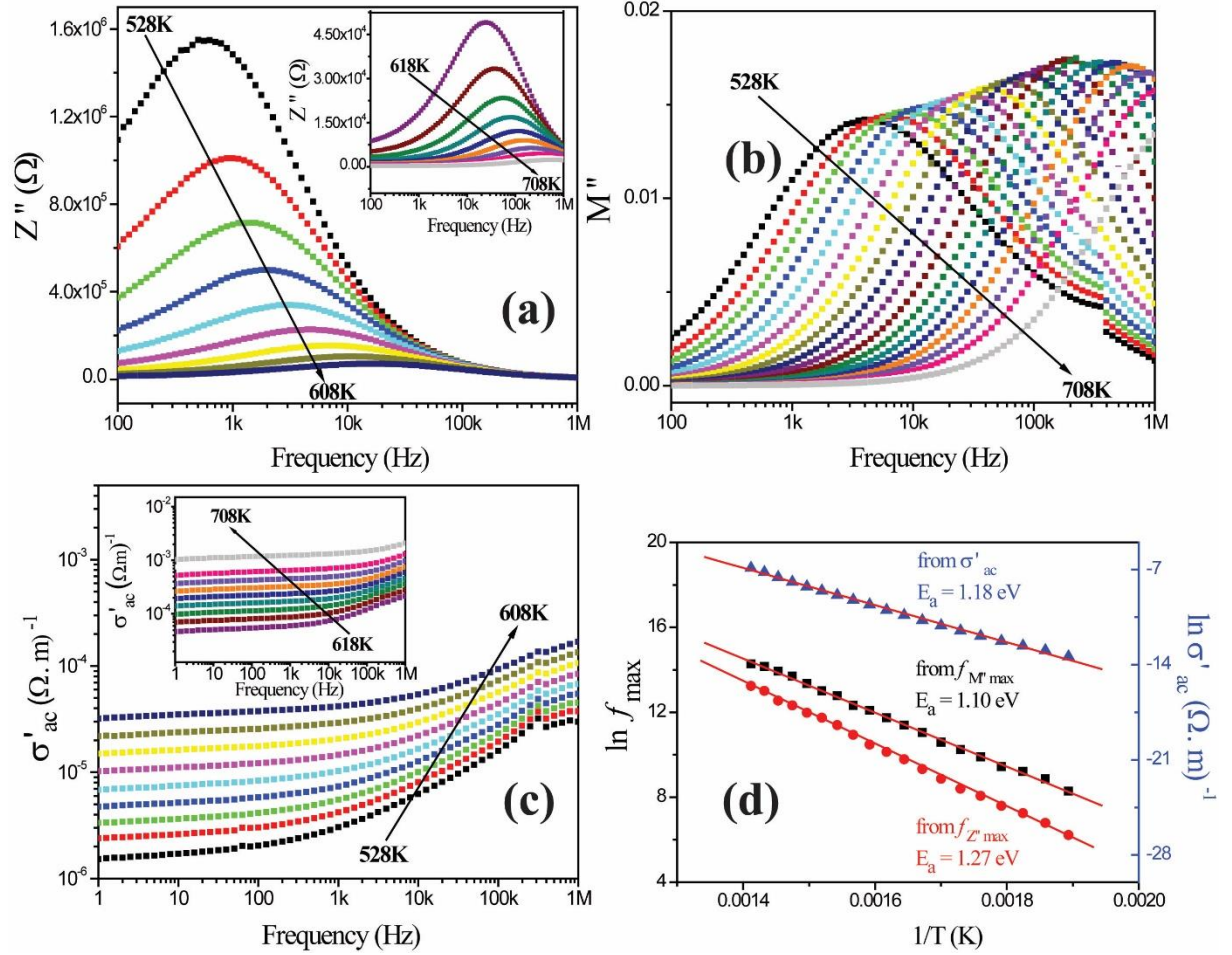
Source: Author.

Figure 22 - ε'' in the RF range (100Hz – 5MHz) as a function of the temperature (528 – 708K).
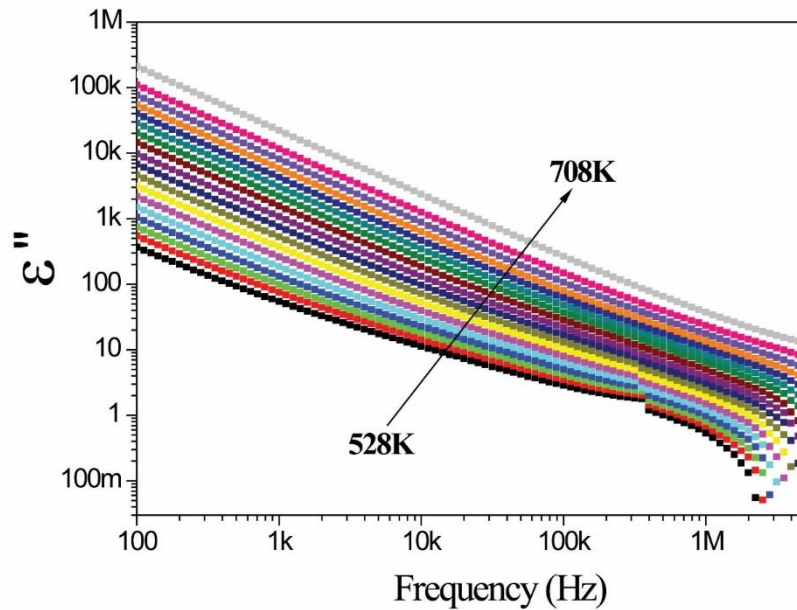
Source: Author.

Figure 23 - C′ in the RF range (100Hz – 5MHz) as a function of the temperature (528 – 708K).
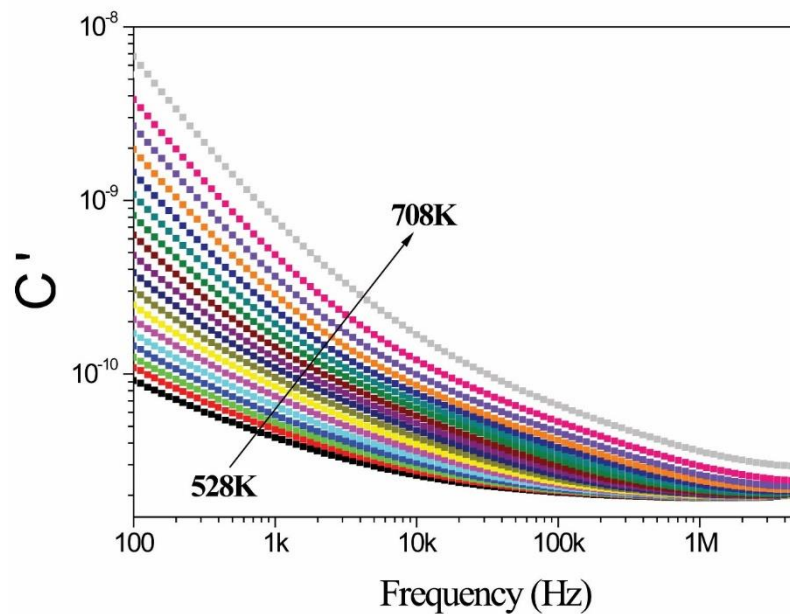
Source: Author.

The proposed methodology by using IS allows identification of each of the electrical contributions (grain, grain boundary and electrode) of the material by equivalent circuits (ZHANG; MAK, 2012). Therefore, it can be correlated to the microstructure, defects

and composition of the sample. From the Nyquist plots (Z' x Z") in Figure 24 (a), each distinct electrical contribution for SMO can be identified. A single semicircular arc can be observed at each temperature from 528 K to 708 K. There is a direct relation between temperature and the Z^* magnitude; the increase in temperature makes the semicircular arc's radii decrease, due to an increase in the conductivity (Figure 21 (c)). Through eisanalyser software (BONDARENKO; RAGOISHA, 2005)(PAIVA *et al.*, 2016), an equivalent circuit was proposed (Figure 24 (b)) for the fitting of the impedance data. The electric profile, obtained through Nyquist plots, was adjusted by the equivalent circuit with three parallel associations of constant phase elements (R-CPE), relative to the three traditional electrical contributions in electroceramics (grain, grain-boundary and electrode-interface). Thus, $Z(\omega)$ can be expressed by the sum of impedances of electric response to grain, grain boundary and electrode:

$$Z(\omega) = Z(\omega)_g + Z(\omega)_{gb} + Z(\omega)_e \tag{6}$$

Where each impedance ($Zn(\omega)$) is described by Equation 7, which is the electrical contribution of a capacitor (CPE), in parallel with a resistor (*Rn*):

$$Z_n(\omega) = \frac{R_n}{1+\omega^2\tau_n^2} - i\frac{\omega R_n \tau_n}{1+\omega^2\tau_n^2} \tag{7}$$

Where the time constant is defined by $\tau_n = R_n.CPE_n$, sub index n in equations corresponds to R_g, CPE_g (grain), R_{gb}, CPE_{gb} (grain-boundary) and R_e, CPE_e (electrode), representing the circuit elements. It is clear that increasing temperature causes decreasing resistance (R_g, R_{gb} and R_e) due to the thermo-activated conduction process, as shown in Table 6 and Table 7.

Table 6 – Part 1 of the values obtained from fitting of the equivalent circuit for SMO electroceramic, where R = resistance, P = equivalent of capacitance and n = deviation of ideal capacitance.

T (K)	Grain			Grain boundary		
	R_1 (Ω)	P_1	N_1	R_2 (Ω)	P_2	N_2
528	1.59×10^6	1.98×10^{-10}	0.868	3.00×10^6	7.94×10^{-10}	0.785
538	1.48×10^6	2.24×10^{-10}	0.845	1.70×10^6	1.73×10^{-9}	0.752
548	1.10×10^6	2.38×10^{-10}	0.843	1.19×10^6	2.18×10^{-9}	0.741
558	7.12×10^5	2.35×10^{-10}	0.854	8.63×10^5	2.19×10^{-9}	0.738
568	5.15×10^5	2.46×10^{-10}	0.849	5.67×10^5	2.64×10^{-9}	0.738
578	3.59×10^5	2.58×10^{-10}	0.848	3.78×10^5	3.45×10^{-9}	0.726
588	2.58×10^5	2.83×10^{-10}	0.842	2.46×10^5	4.63×10^{-9}	0.715
598	2.24×10^5	4.16×10^{-10}	0.807	1.29×10^5	1.25×10^{-8}	0.679
608	1.17×10^5	2.68×10^{-10}	0.853	1.14×10^5	5.38×10^{-9}	0.715
618	7.25×10^4	2.29×10^{-10}	0.871	8.42×10^4	4.46×10^{-9}	0.723
628	4.27×10^4	1.76×10^{-10}	0.897	6.17×10^4	3.36×10^{-9}	0.738
638	3.43×10^4	2.06×10^{-10}	0.884	3.99×10^4	5.36×10^{-9}	0.722
648	2.16×10^4	1.63×10^{-10}	0.908	3.02×10^4	3.90×10^{-9}	0.739
658	1.64×10^4	1.83×10^{-10}	0.900	2.09×10^4	4.71×10^{-9}	0.736
668	9.28×10^3	1.26×10^{-10}	0.937	1.72×10^4	2.75×10^{-9}	0.761
678	7.18×10^3	1.45×10^{-10}	0.928	1.18×10^4	3.67×10^{-9}	0.754
688	5.53×10^3	1.82×10^{-10}	0.917	7.48×10^3	5.58×10^{-9}	0.743
698	4.39×10^3	1.87×10^{-10}	0.918	4.76×10^3	9.75×10^{-9}	0.726
708	4.06×10^3	2.31×10^{-10}	0.902	2.89×10^3	2.56×10^{-8}	0.691

Source: Author.

Table 7 – Part 2 of the values obtained from fitting of the equivalent circuit for SMO electroceramic, where R = resistance, P = equivalent of capacitance and n = deviation of ideal capacitance.

T (K)	Electrode		
	R_3 (Ω)	P_3	N_3
528	1.57×10^6	5.59×10^{-8}	0.582
538	8.40×10^5	1.70×10^{-7}	0.536
548	5.99×10^5	2.55×10^{-7}	0.530
558	4.61×10^5	3.48×10^{-7}	0.484
568	3.24×10^5	4.63×10^{-7}	0.492
578	2.16×10^5	8.69×10^{-7}	0.463
588	1.49×10^5	1.39×10^{-6}	0.450
598	9.09×10^4	1.92×10^{-6}	0.513
608	7.55×10^4	3.06×10^{-6}	0.416
618	5.51×10^4	4.41×10^{-6}	0.387
628	3.81×10^4	6.44×10^{-6}	0.368
638	2.78×10^4	1.03×10^{-5}	0.362
648	2.03×10^4	1.39×10^{-5}	0.339
658	1.57×10^4	2.14×10^{-5}	0.330
668	1.20×10^4	2.53×10^{-5}	0.313
678	8.76×10^3	3.51×10^{-5}	0.309
688	6.74×10^3	4.94×10^{-5}	0.290
698	5.46×10^3	1.01×10^{-4}	0.266
708	5.10×10^3	1.99×10^{-4}	0.235

Source: Author.

Therefore, the three contributions are convoluted in the same arc. However, the increase in temperature makes the electric response of the electrode-interface start to distinguish between other processes (grain and grain boundary), with one arc present in lower frequencies. Moreover, the parameter fitted for this event demonstrates a conduction process; see lower values of n (deviation of ideal capacitance) for CPE in Table 6 and Table 7. It is also possible to see that the R_g and R_{gb} decrease with the temperature. However, the conduction of the grain boundary (CPE_{gb}) is more pronounced than that of the grain (CPE_g), due to the values of n being smaller than for the grain. For the grain, the fitting demonstrates no conduction, since n values remain almost constant throughout the temperature range. The deviation of n values of unity or to use of CPE instead to capacitance is due the inhomogeneity as roughness.

The TCC was also calculated for frequencies 100 Hz (23.47 ppm.$°C^{-1}$), 1 kHz (19.97 ppm.$°C^{-1}$), 100 kHz (8.59 ppm.$°C^{-1}$) and 1 MHz (6.35 ppm.$°C^{-1}$). According to the proposal suggested by the International Electrotechnical Commission (IEC) and the Electronic Industries Alliance (EIA) (IEC/EN 60384-1, IEC/EN 60384-8/9/21/22, and EIA

RS-198), SMO can be classified as a capacitor class 3 (IEC) for 100 Hz and 1 kHz or class 4 (EIA) for 100 kHz and 1 MHz. Herein, the SMO is adequate for application in barrier layer capacitors at frequencies of 100 Hz and 1 kHz, where the TCC presents high values. The SMO is also suited to use in resonant circuits, at frequencies of 100 kHz and 1 MHz.

The dielectric properties at microwave frequencies were measured using the Hakki-Coleman dielectric resonant method (Table 8). From the TE011 mode, the obtained frequency was 5.685 GHz (ε' = 17.21 and tan δ = 0.0145). The SMO shows equivalent dielectric properties when compared to other electroceramics, such as $Mg_5Ta_4O_{15}$ (JAWAHAR *et al.*, 2003), $LaVO_4$ (LI, W. *et al.*, 2017) and $BiCu_2PO_6$ (HAO *et al.*, 2017), but it has higher tan δ values. More recently, the relationship between the dielectric properties of an electroceramic and its application in antenna devices has been investigated (AUZEL, 2004; RODRIGUES *et al.*, 2013; SILVA *et al.*, 2014; CAMPOS *et al.*, 2015; PAIVA *et al.*, 2016). Therefore, there are important factors available to evaluate this material in dielectric resonators. One of them is the S_{11}, which shows the relationship between the reflected and irradiated energy from the resonator (SILVA, DA *et al.*, 2017).

Figure 24 - (a) Complex impedance plots of SMO at different temperatures (528–708 K) with respectively fitted spectrum and (b) equivalent circuit employed in the simulation of the complex impedance plots.
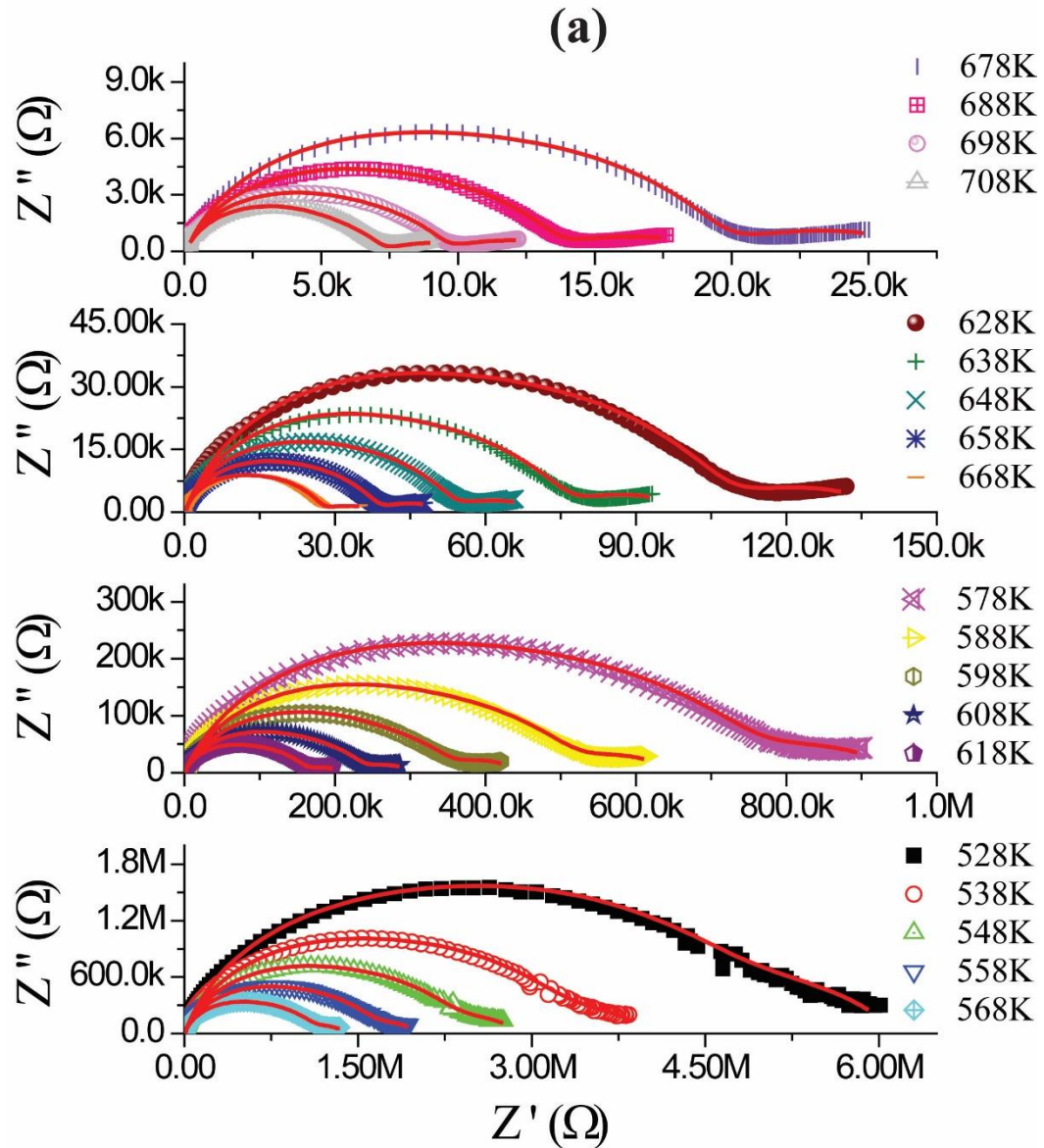
Source: Author.

Table 8 - Measurements in microwave range by Hakki-Coleman method (Q x *f* is quality factor).

Sr₃MoO₆	
Diameter (mm)	15.942
Length (mm)	9.614
f (GHz)	5.685
ε'	17.210
tanδ	1.45×10^{-2}
Q x f	395.37

Source: Author.

Figures 25 (a)–(c) illustrates a schematic of the setup used in the antenna measurement, with the radiation pattern simulated for a SMO-based DRA. The setup consists of a coaxial probe inserted into the ground plane (copper plate). This coaxial probe feeds the DRA and is positioned laterally on the antenna. In this experimental setup, the main or dominant mode is HE11δ; the frequency of the operation antenna (f_o), is given by Equation 3 (PETOSA, 2007).

Due to the imperfection of electroceramics, air gaps were introduced to the model, separating the SMO-based DRA from the coaxial probe and the ground plane, to allow better adjustment. For this purpose, f_o (3.653 GHz) was calculated by Equation 3 and using the data obtained by Hakki-Coleman method (Table 8). The use of air gaps are due to the frequency shift obtained by Equation. 3 (3.653 GHz (no air gap)) and experimental data (3.719 GHz). Therefore, the lateral air gap is used to match experimental data with numerical results. This model compares numerical simulations to experimental data (JUNKER *et al.*, 1994, 1995).

Figure 26 (a) shows the experimental and simulated data of S₁₁ from the SMO-based DRA. It can be seen that the DRA is operating with f_o at 3.72 GHz and its experimental S₁₁ value is -28.75 dB (Table 9). The experimental and simulated data show good agreement, which denotes a successful simulation. As seen in Table 9, the correlation between the experimental and simulated data is clearly shown for the S₁₁ values. For commercial antenna, the S₁₁ values must be ≤ -10 dB (BALANIS, 2007); the SMO-based DRA shows -28.756 dB.

Table 9 - Experimental and simulated data from DRA simulation for SMO.

	SMO-based DRA		
	Experimental	Simulated	Error (%)
f_o (GHz)	3.71965	3.72057	0.03
S_{11} (dB)	-28.756	-28.769	0.05
Bandwidth (%)	5.44	5.77	6.16
Efficiency (%)		85.37	
Peak resonant impedance (Ω)	81.44	70.85	13.00
Impedance (Ω)	50.84	51.43	1.16
Directivity (dBi)		5.70	
Gain (dBi)		5.00	

Source: Author.

Figure 25 - (a) Schematic of the setup used for SMO-based DRA with the simulated radiation diagram, (b) top and side (c) view of prototype of the proposed SMO-based DRA.
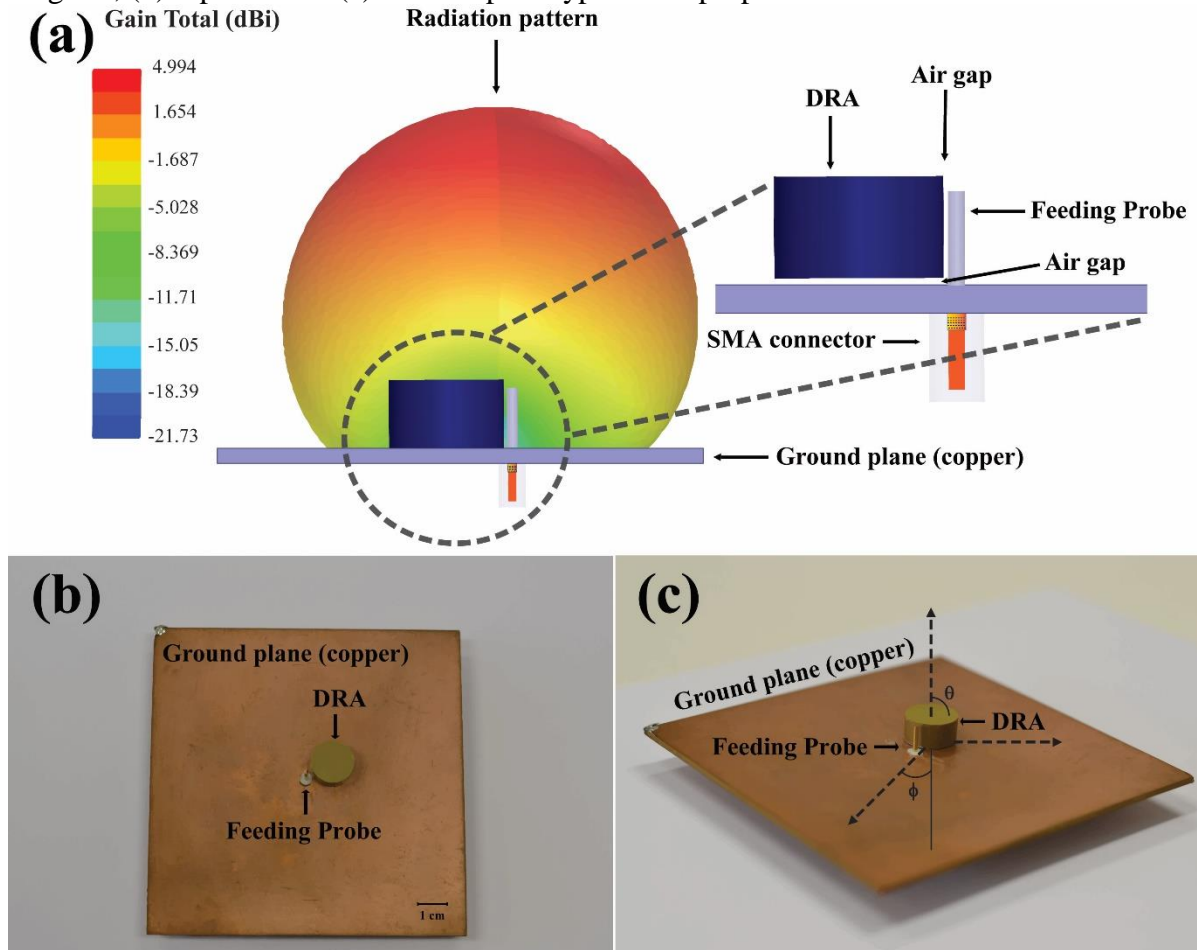
Source: Author.

The inspection of the simulated and experimental impedances (Figure 26 (b)) was performed to reinforce the good agreement between the SMO-based DRA; the simulated

impedance of the S_{11} follows the experimental values. Figure 27 shows this same information in the Smith chart, which is another way to evaluate this impedance matching. The impedance spectra (experimental and simulated) in the frequency range 3.2–4.4 GHz show a good agreement with each other. The deviations observed are due to the impossibility to replicate, in a numerical model, all of the details of the ceramic cylinder and ground plane (roughness, pores etc.), but good approximation in the results suggests good reliability of the simulated results.

The main deviation is in the operating frequency of the antenna (3.72 GHz), which has 50 Ω of feed impedance. The experimental (50.84 Ω) and simulated (51.43 Ω) values for this system demonstrate acceptable impedance matching between the feeder and the DRA (Table 9). The error is small (1.16 %) and can be neglected. This impedance matching is due to the modeled separation of the feeder and the DRA, as for better matching, micrometric shifts between the feeder and the DRA are necessary, to account for the imperfections in the sample.

Figures. 26 (c) and (d) show the simulated polar and Cartesian diagram of radiation, respectively. These results describe how the DRA is radiating into free-space below θ and ϕ angles, as shown in Figure 26 (c). It can be seen that the simulated radiation pattern (E-plane (ϕ = 0º) and H-plane (ϕ = 90º)) presents a radiate profile consistent with a typical cylinder DRA, i.e., this antenna presents a maximum radiation at the top of the cylinder, as a preferred direction (LUK; LEUNG, 2003; PETOSA, 2007).

Figure 26 - (a) Experimental and simulated plots of the S_{11}, (b) experimental and simulated impedance input Z' and Z'', (c) simulated radiation pattern of E_θ ($\phi = 0°$, 90°), d) gain of E_θ ($\phi = 0°$, 90°) for SMO-based DRA.
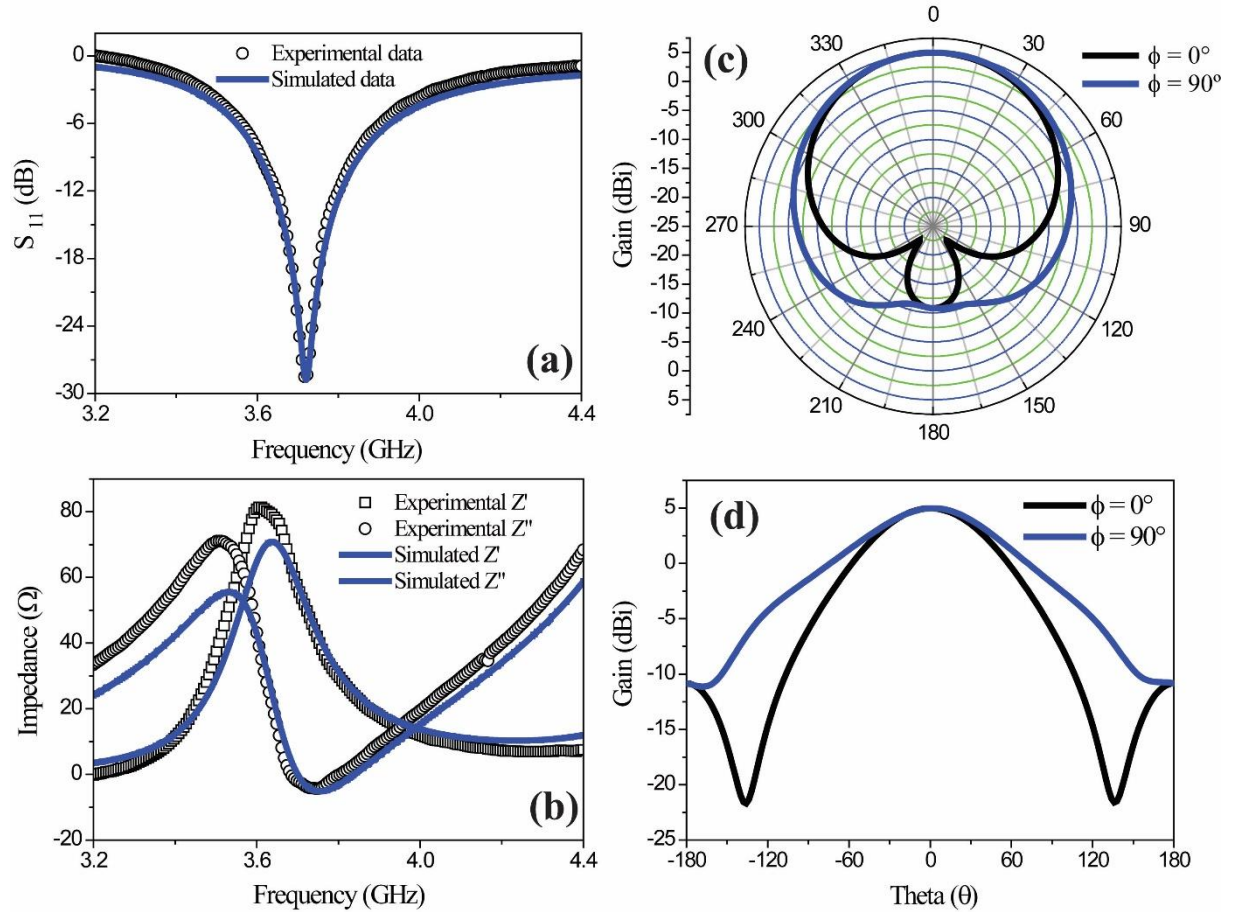
Source: Author.

Figure 27 - Experimental and simulated Smith chart of the SMO-based DRA.
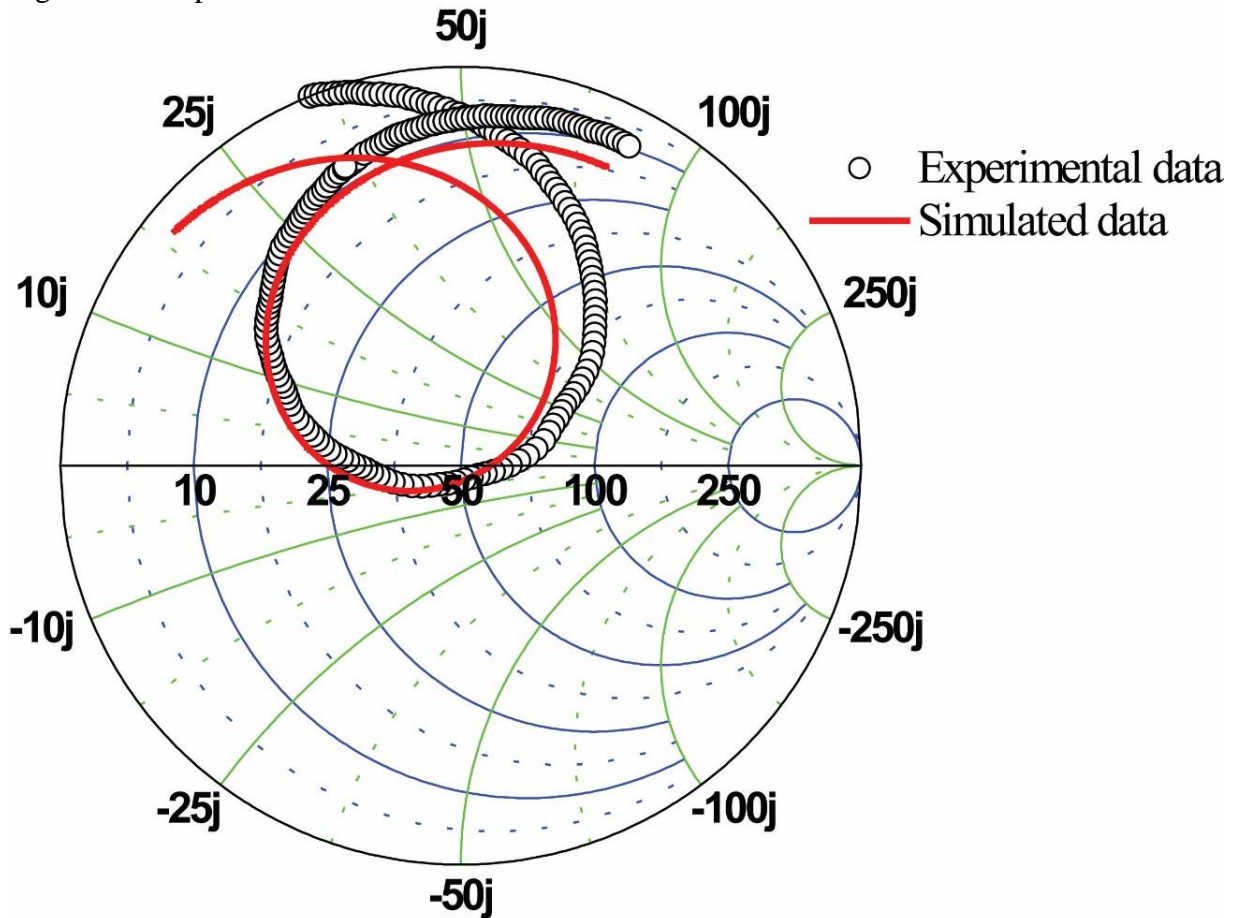
Source: Author.

In dielectric resonators, the Bandwidth (BW) of the analyzed mode is a function of the dielectric properties (PETOSA, 2007). In this sense, for higher ε' values, there is a narrower BW. For SMO-based DRA, the BW measured at -10 dB (5.44 %), was consistent with values seen in other DRAs (KAJFEZ; GUILLON, 1998; PETOSA, 2007). From the numerical simulation, the values of directivity (5.70 dBi, Figure 28 (a)), gain (5.00 dBi. Fig. 28 (b)) and efficiency (85.37 %, Fig. 28 (c)) for the SMO-based DRA (Table 9) are higher than SWO-based DRAs (PAIVA *et al.*, 2016) and other systems (AUZEL, 2004; RODRIGUES *et al.*, 2013; SILVA *et al.*, 2014; CAMPOS *et al.*, 2015; PAIVA *et al.*, 2016). Compared to alumina (Al_2O_3), which is mostly used to design DRAs, SMO-based DRA shows an attractive advantages, such as smaller dimensions, besides presenting a narrower BW.

Figure 29 (a-b) shows the numerical simulations used to compare both DRAs. For equal f_o values, considering SMO-based DRA ceramic, Al_2O_3 ceramic geometry needs to be

adjusted for higher dimensions (diameter= 19.6 mm and thickness = 12.25 mm) than SMO (Table 8). Moreover, due to Al_2O_3-based DRA presents lower ε' (9.80) and $\tan\delta$ ($2.0x10^{-4}$) values (SEBASTIAN; JANTUNEN; UBIC *et al.*, 2017), the gain (5.95 dBi) and efficiency (99.71 %) are higher than SMO-based DRA (Figure 28).

From the obtained results, it is possible to demonstrate that SMO-based DRA is operating as an antenna, with good results in the far fields parameter for the dimensions and dielectric properties used in this DRA. From the operation frequency and gain, and the efficiency achieved by this antenna, there are some interesting suggested applications in different devices operating in the S-band (from 2 to 4 GHz) such as weather radars, surface ship radars, and some communications satellites (BALANIS, 2012).

Figure 28 - (a) Directivity, (b) gain and (c) efficiency from numerical simulation as a function of the frequency for θ = 0°.
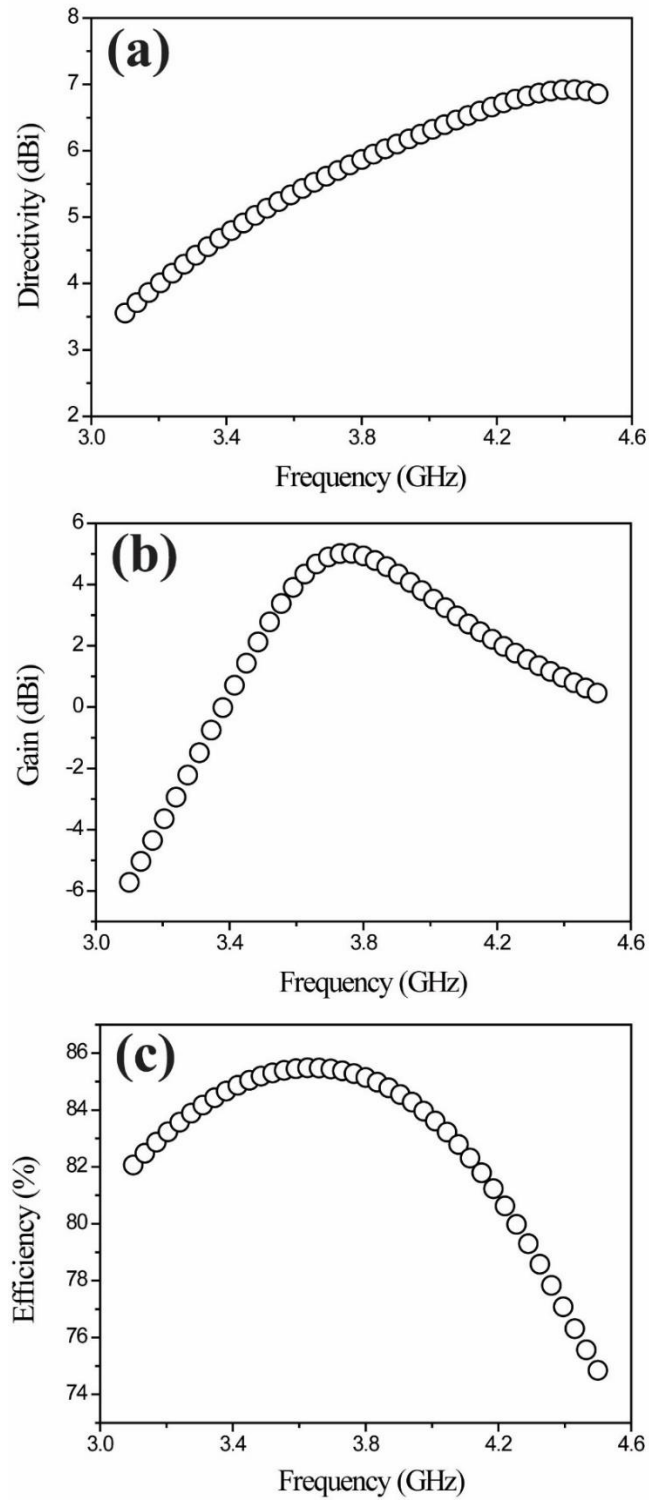
Figure 29 - (a) S_{11} and SMO-based DRA; Al_2O_3-based DRA in the same geometry ($\bullet$) and f_o ($\blacksquare$) observed for SMO-based DRA ($\blacktriangle$), and (b) radiation pattern for Al_2O_3-based DRA.
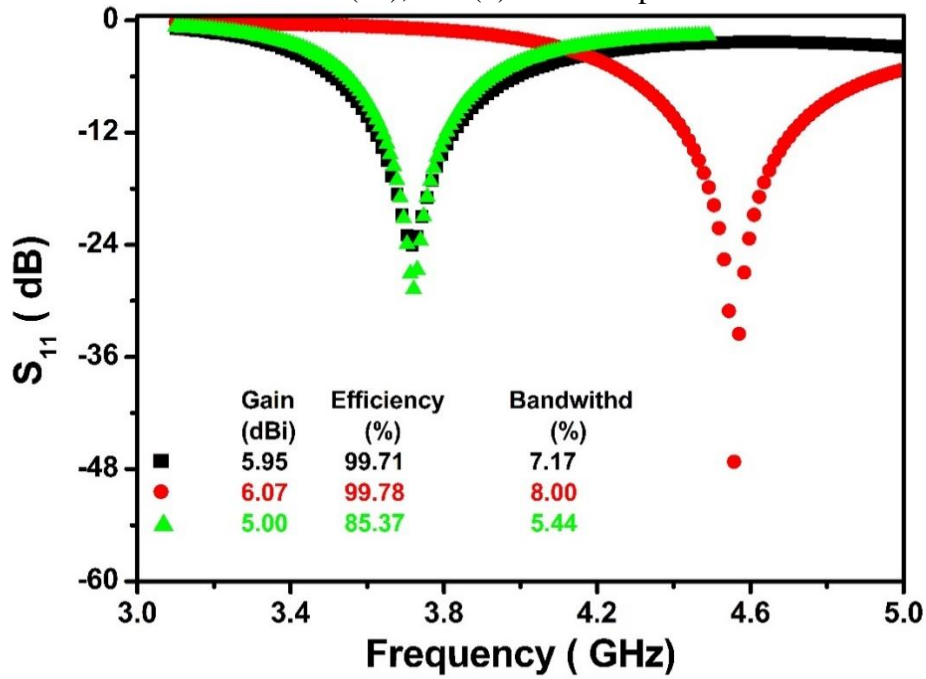
(a)
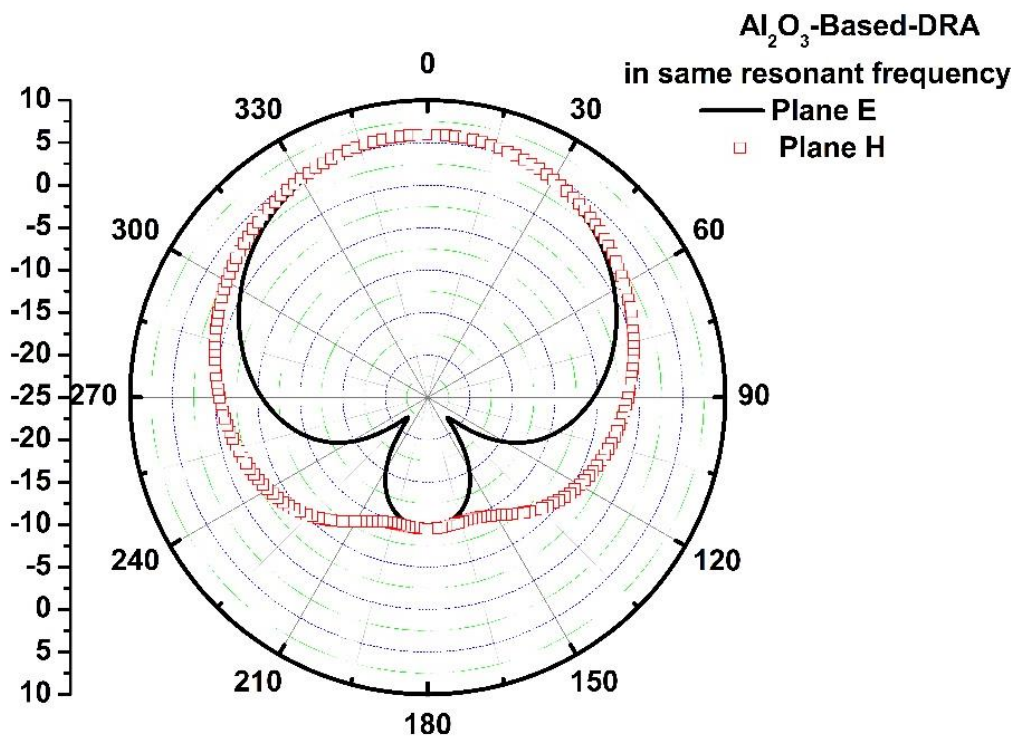
(b)

Source: Author.

3.4 Conclusions

In this work, the crystalline phase of the SMO double perovskite electroceramic was successfully synthesized and characterized. The IS studies show three relaxation processes suitable for electroceramics: grain, grain boundary and electrode interface. A thermo-activated process with activation energy equal to 1.1 eV was observed. SMO electroceramics can be used for barrier layer capacitors for small frequencies (100 Hz and 1 kHz) and resonant circuits for higher frequencies (100 kHz and 1 MHz). In addition, for the microwave range, SMO-based DRA is also available to be used as an antenna device operating in the S-band range.

4 INVESTIGATION OF THE PHOTOLUMINESCENCE PROPERTIES OF Tb^{3+} AND Eu^{3+} IONS CO-DOPED Sr$_3$MoO$_6$ DOUBLE PEROVSKITE PHOSPHORS

4.1. Introduction

The electronic devices with photoluminescent main feature such as ultraviolet (UV) light emitting diodes (LED) and solid state lightening materials have been studied in the last years. Actually, there are many investigations of news inorganic luminescence materials for practical applications in the devices for artificial light production (PAVANI *et al.*, 2014). Lanthanide ions are excellent candidates for spectral conversion and have used to explore the luminescence properties, including the upconversion and downconversion process. Also, in the diverse investigations to obtain emission in the visible region have been used one type of lanthanide ion or a pair of lanthanide ions. (AARTS *et al.*, 2011). Among the rare earth (RE^{3+}) ions, Eu^{3+} and Tb^{3+} have been studied due to their excellent electronic properties under excitation in the UV range. In white light emitting diodes (wLED) devices, the red emission can be obtained by using the Eu^{3+} doped materials. On the other hand, the Tb^{3+} ion have used in wLED application due to be a good luminescent activator and also to its attractive reproducible optical properties in the green spectral region (PAVANI *et al.*, 2014).

As shown, the materials obtained with vanadates, molybdates and tungstates groups doped with RE^{3+} ions have significantly grown in the field of wLEDs due to shows shorter wavelength excitation properties and excellent chemical stabilities. Recently, much attention has been paid to the investigation on molybdate-based inorganic host materials by exhibits of a great chemical stability and potential applications in photoluminescence area. There have been many reports about the photoluminescent properties of the double perovskite based-molybdate phosphors, such as Sr$_2$MgMo$_x$W$_{1-x}$O$_6$:Eu^{3+} (LI *et al.*, 2013), Sr$_2$ZnW$_{1-x}$Mo$_x$O$_6$:Eu^{3+},Li$^+$.(LI *et al.*, 2016) and Sr$_3$MoO$_6$:Eu^{3+} (JING *et al.*, 2015). But to our knowledge, the photoluminescence properties of Eu^{3+} and Tb^{3+} co-doped SMO phosphor have not been reported. Based on the above considerations, this research focused on the synthesis and studies photoluminescence properties of Eu^{3+} separately, and Eu^{3+} and Tb^{3+} ions co-doped SMO double perovskite phosphors. For structural characterization was used PXRD and SEM. The photoluminescence properties of the phosphors and the influence of concentration of the rare earth was examined under UV excitation.

4.2. Experimental Methods

Sr_3MoO_6 (SMO) co-doped with Eu^{3+} and Tb^{3+} ions ceramics were synthesized by a solid-state reaction. The starting materials powders $SrCO_3$ (Aldrich, 98%), MoO_3 (MaTeck, 99%), Eu_2O_3 (MaTeck, 3N), Tb_4O_7 (Aldrich, 99.9%) and Li_2CO_3 (Panreac, 99%) were weighted stoichiometric amounts for each sample, and then the respective powders for each sample was milled for 2h at 370 rpm in a Fritsch Pulverissette 6 planetary mill. After milling process, each powder milled were calcined in corundum crucible in air for 6 h at 1100 °C. And then the calcined products were ground and mixed with mortar and pestle. Finally, the powders calcined from each sample were uniaxially pressed into a steel die to form pellets. The pellets ceramics were sintered at 1100°C for 6 h in air. The nomenclatures of all prepared samples are exhibited in Table 10.

XRD measurements were carried out using a PANalytical diffractometer (Empyrean Model) operating at 40 kV and 45 mA in the geometry of Bragg-Brentano, with a Cu tube ($K\alpha1 = 1.54059$ Å, $K\alpha2 = 1.54443$ Å). The diffraction patterns were obtained at room temperature (~25 °C). Each measurement was collected from 10° to 70° (2θ) at a step size of 0.026° with an analysis time at each step of 56.7 s. Micrograph images and microstructure analyze from sintered samples were obtained at room temperature by SEM using TESCAN VEGA3 microscope with EDS linked. For this, each sample was previously metalized with thin layer of graphite by the Metalizator Quorum QT150ES. Photoluminescence measurements (PL) was obtained on a spectrofluorimeter (JOBIN YVON Fluorolog-3) equipped with a 450 W Xenon lamp as the excitation source.

Table 10 - Nomenclature of Eu^{3+}–Tb^{3+} co-doped Sr_3MoO_6 phosphors.

Concentration of dopants (molar fraction)			Nomenclature
Tb_4O_7	Eu_2O_3	Li_2CO_3	
0.00	0.00	0.00	SMO
0.00	0.02	0.02	SMO:Eu2Li2
0.01	0.02	0.03	SMO:Eu2Tb1Li3
0.02	0.02	0.04	SMO:Eu2Tb2Li4
0.04	0.02	0.06	SMO:Eu2Tb4Li6

Source: Author.

4.3. Results and discussion

In order to analyze the synthesis and the crystalline structure of double perovskite SMO undoped and doped was obtained the diffractograms using PXRD. Figure 30 shows the PXRD patterns of all synthesized phosphors obtained by a solid-state reaction at 1100°C, were correlated with Sr_3MoO_6 JCPDS nº 027-1441 (JING *et al.*, 2015)(PAIVA *et al.*, 2018) pattern that belongs to the cubic crystal system with space group Fm-3m. As can be seen all phosphors showed similar crystallographic plans when compared with the pattern and absence of other peaks from secondary phase, those confirm that addition of rare earth in crystallographic structure was obtained correctly. Therefore, the structure of SMO does not change with the addition (Eu^{3+}, Tb^{3+}, and Li^+) in these composition studied.

Figure 30 - XRD calcined obtained from SMO doped and co-doped.
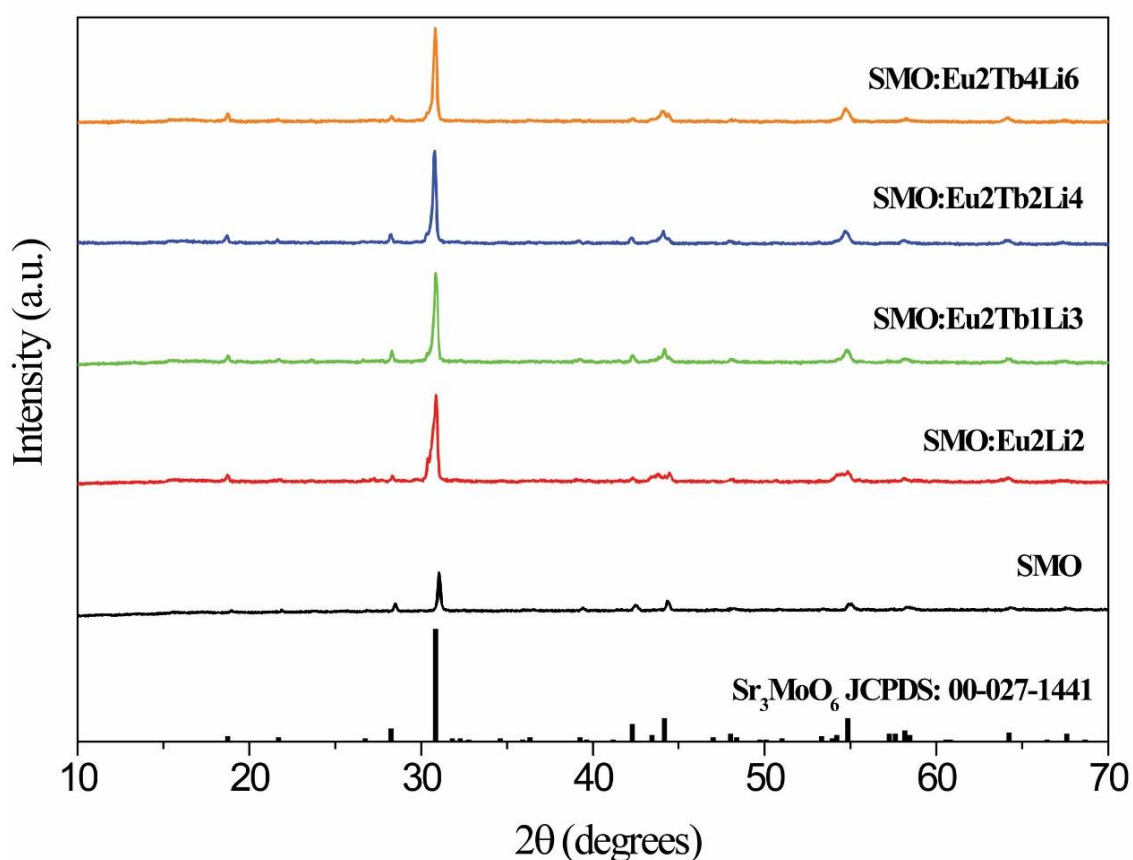
Source: Author.

The photomicrograph of all sintered phosphors (at 1100°C) at an amplification of 1.000x was assessed using SEM (Figure 31 (a-e)). As can be seen that all micrographs exhibit homogeneous grains with a globular shape. In addition, it reported a decrease of empty spaces with the increase of Tb^{3+} ions in the phosphors; it can suggest an increase of densification of material. These results show a different morphology when compared with to literature (JING *et al.*, 2015) due to the different parameters of the synthesis process (calcination and sintering temperature and/or measurements) in this work.

Figure 31 - Scanning electron photomicrograph of SMO (a), SMO:Eu2Li2 (b), SMO:Eu2Tb1Li3 (c) SMO:Eu2Tb2Li4 (d) SMO:Eu2Tb4Li6 at an amplification of 1.000x.

(a)
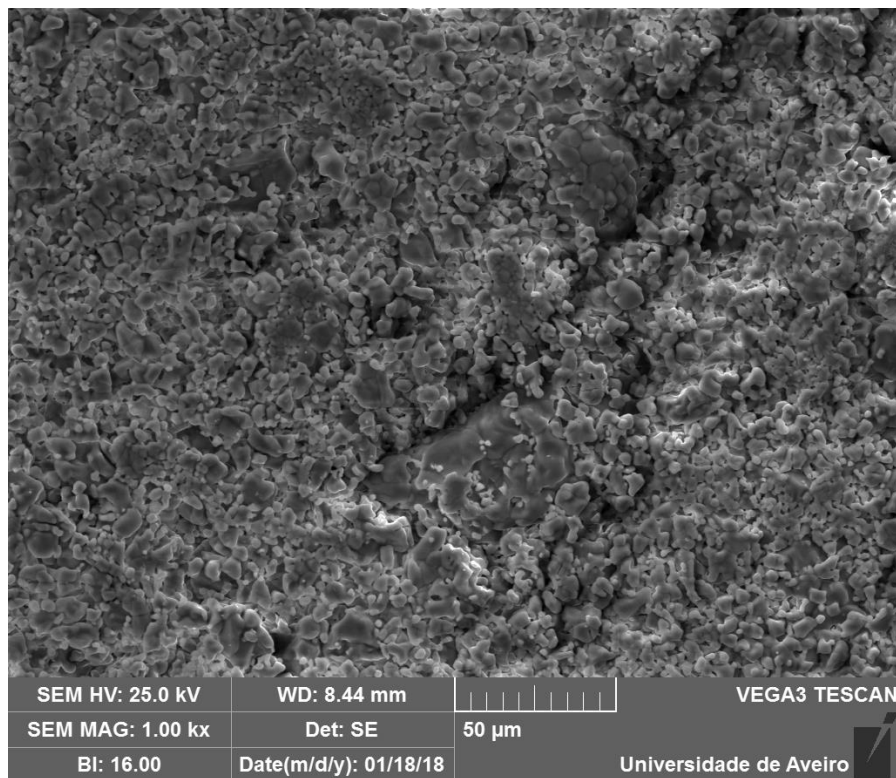
(b)
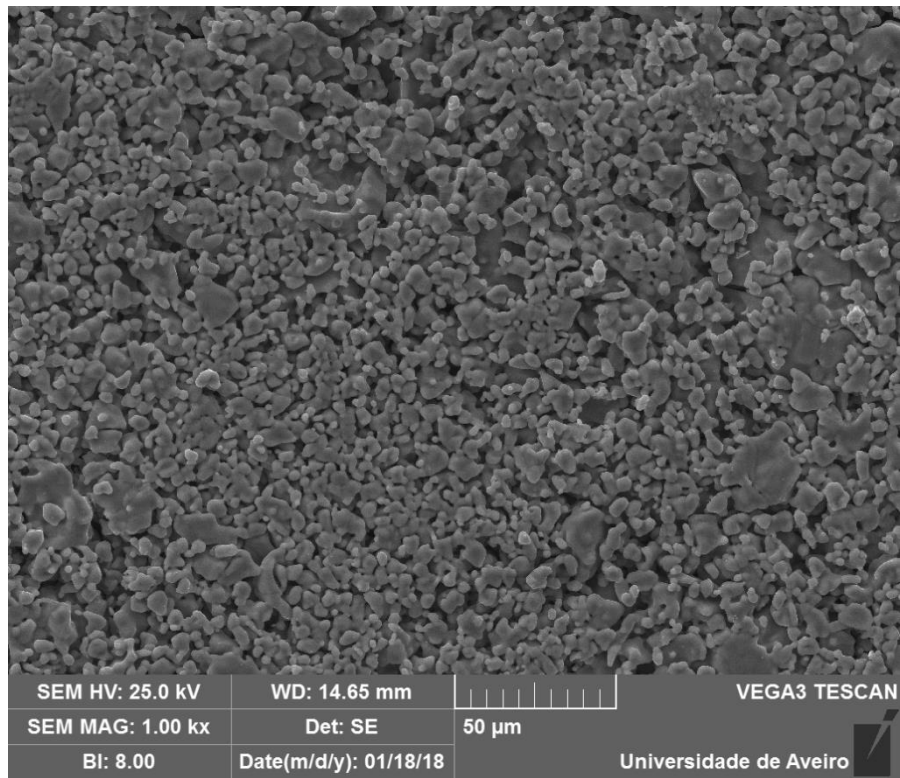
(c)
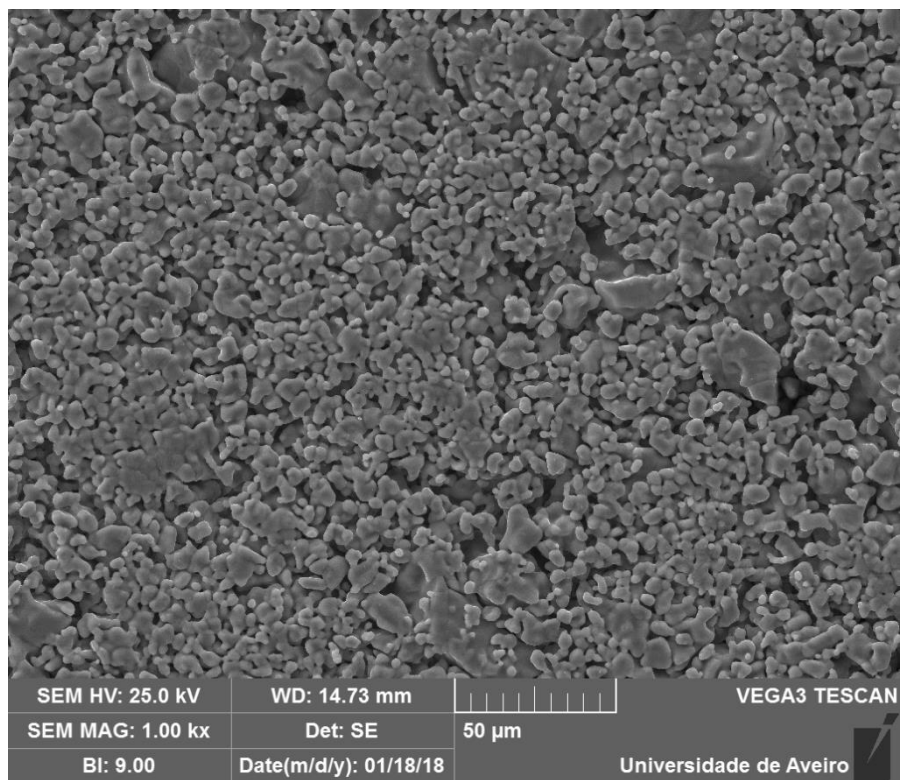
(d)
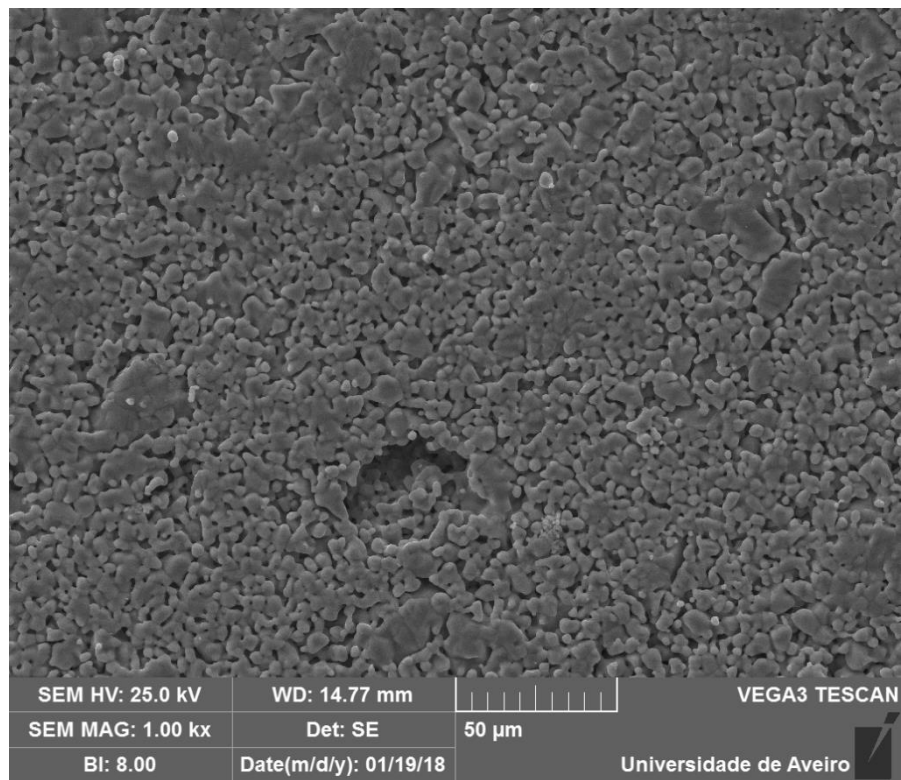
(e)
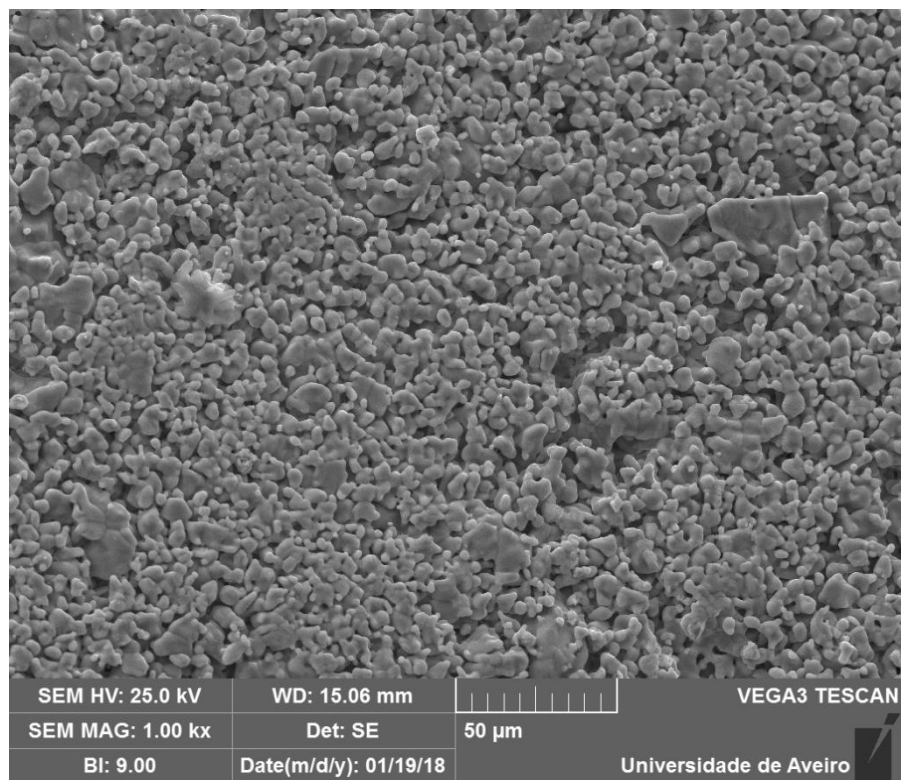
Source: Author.

The photoluminescence spectrum of SMO:Eu2Li2 phosphor upon excitation at (a) 325 nm and (b) 532 nm are shown in Figure 32. In figure 32 (a) the spectrum is composed of main bands assigned to $^5D_1 \rightarrow {}^7F_2$ (555 nm), $^5D_0 \rightarrow {}^7F_0$ (580nm), $^5D_0 \rightarrow {}^7F_1$ (593 nm), $^5D_0 \rightarrow {}^7F_2$ (613nm) and $^5D_0 \rightarrow {}^7F_3$ (656 nm) transitions of Eu^{3+} ion. Hence, the results obtained by PL indicated that the host (Sr_3MoO_6) was effectively doped with Eu3+ and the calcination process was satisfactory.

Figure 32 - Photoluminescence spectra of SMO:Eu2Li2 phosphor (a) 325 nm and (b) 532 nm excitations, respectively.
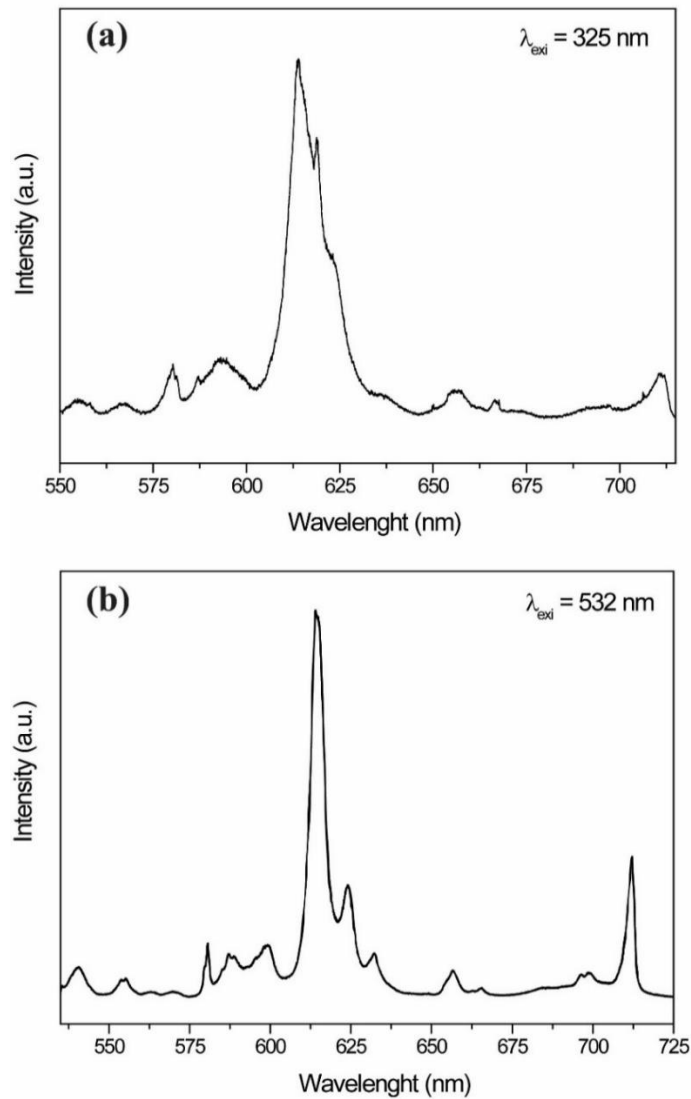
Source: Author.

Figure 33 (a) shows the photoluminescent spectra of SMO:Eu2Li2, SMO:Eu2Tb1Li3, SMO:Eu2Tb2Li4 and SMO:Eu2Tb4Li6 phosphors excited at 325 nm. The

spectra consist of emission peaks from Eu^{3+} ions with prominent emission at 617 nm, but it does not possible to identify any emission from Tb^{3+} in different compositions. Moreover, the sample with the lowest concentration of Tb^{3+} (SMO:Eu2Tb1Li3) shows the spectra with higher intensity, it can suggest the possible influence of Tb^{3+} ions in the energy transfer mechanism of Eu^{3+} ions in the phosphor. Through of energy level diagram for Eu^{3+} ions (see Figure 34) is possible to understand the optical transition of Eu^{3+} ions and the influence of Tb^{3+} ions in electronic transitions process. It is noticed that all the Eu^{3+} peaks in Figure 33 resembles those observed in Figure 32 (a). It is well known that the luminescence properties strongly depend on the concentration of dopant ions, composition and excitation wavelength (PAVANI *et al.*, 2014)(SHINDE *et al.*, 2013). Therefore, SMO phosphors with different concentration of co-dopants (Tb^{3+} and Eu^{3+}) were investigated to confirm the dopant concentration effect on the luminescence properties.

Figure 33 - Photoluminescence spectrum of Eu^{3+} and Tb^{3+} with different compositions co-doped SMO phosphors excited at 325 nm.
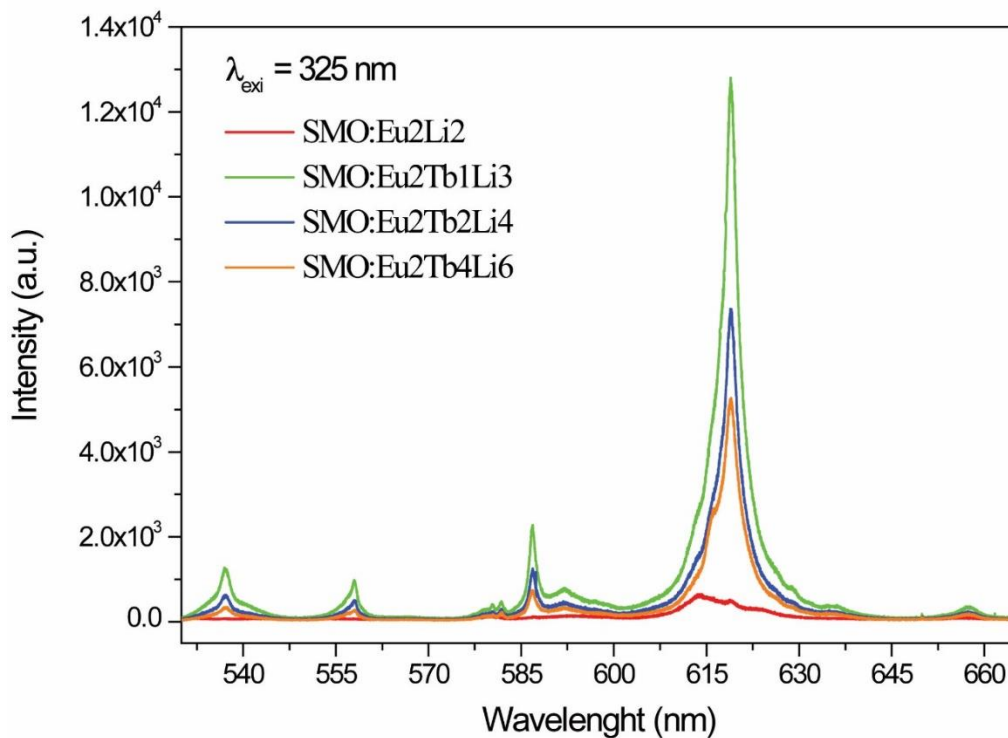
Figure 34 - Energy level diagram and the related optical transition for Tb^{3+} and Eu^{3+} ions.
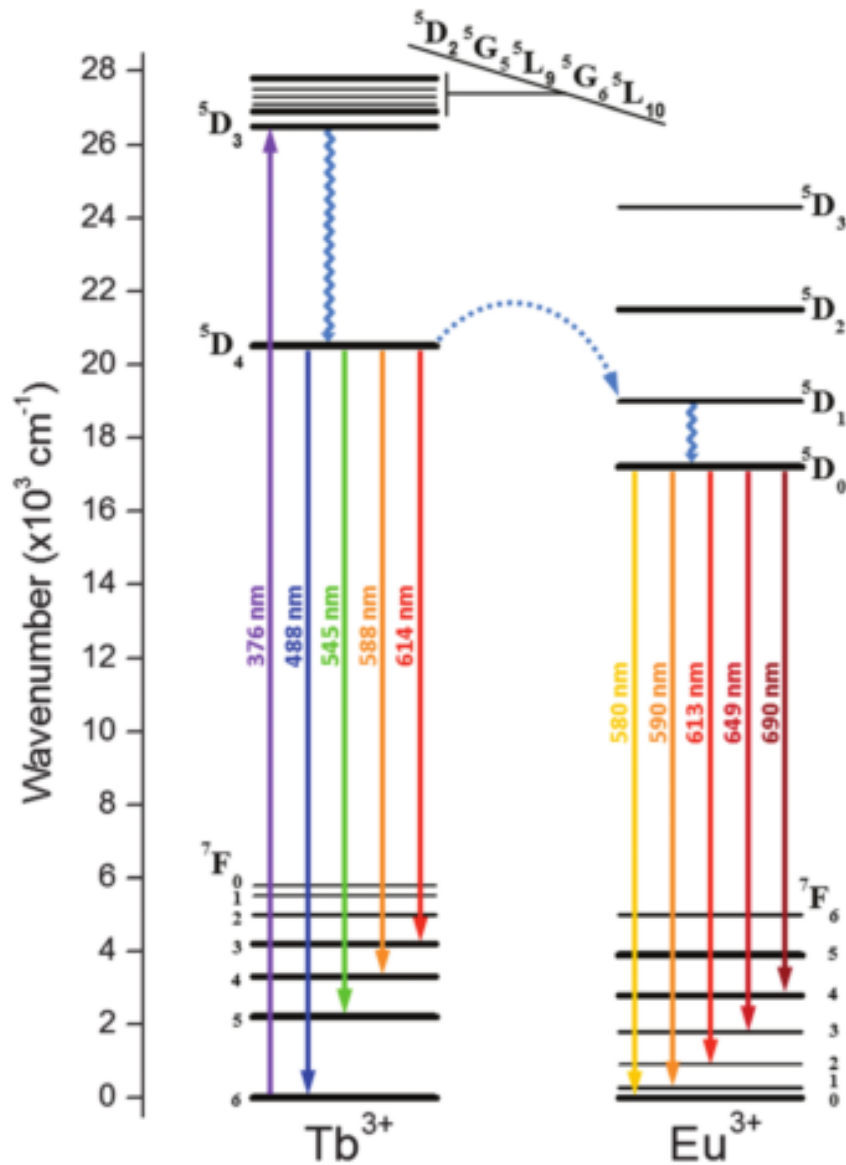
Source: (BACK et al., 2016)

The emission spectra of SMO:Eu2Tb1Li3 phosphors under 325 nm excitation at temperature range between 15 and 300 K are shown in Figure 35. It is reported the temperature dependence on the emission intensity of the phosphor, and the emission intensity of the phosphor increases gradually with the decreased temperature. This process take place due to the thermal excitation to the Charge transfer state (CTS) band (LI *et al.*, 2016).

Figure 35 - Temperature-dependent (from 15 to 300K) emission spectra of SMO:Eu2Tb1Li3 excited at 367 nm.
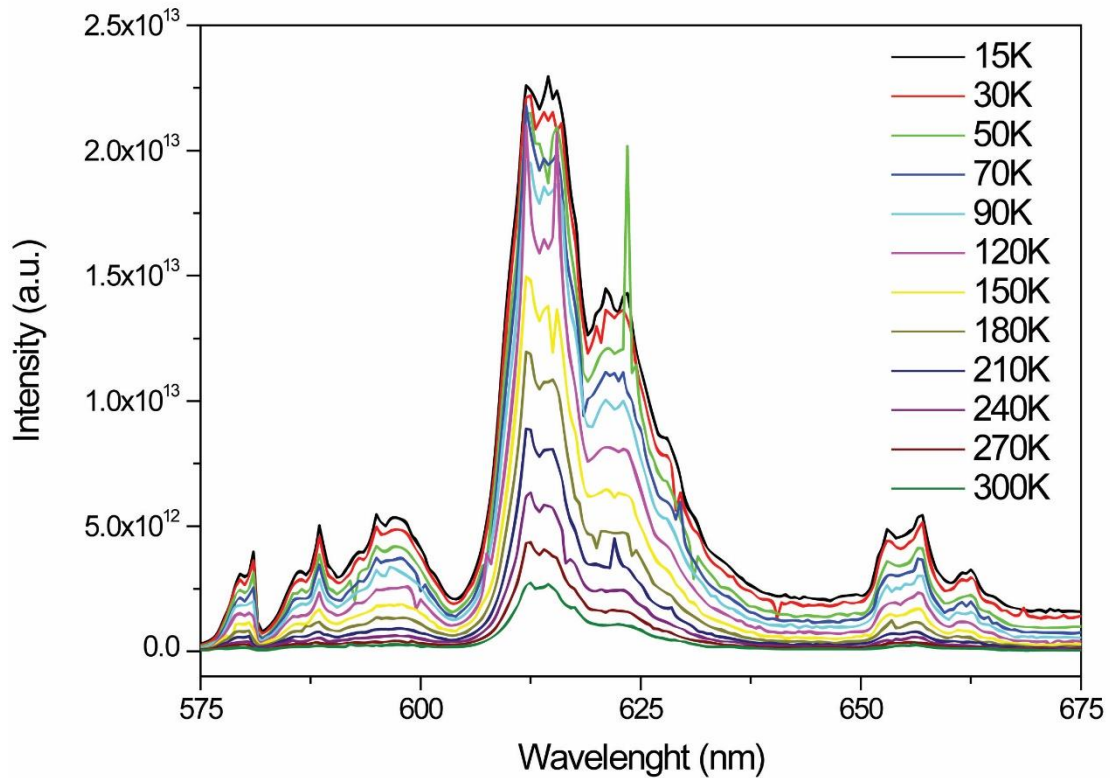
Source: Author.

4.4. Conclusion

The Eu^{3+}-Tb^{3+} co-doped Sr_3MoO_6 phosphors were successfully synthesized by solid-state reaction method. The emission spectra of Eu^{3+}-Tb^{3+} singly and co-doped double perovskite phosphors have been measured. The photoluminescent properties of Sr_3MoO_6:Eu^{3+} indicate that these phosphors exhibit red emission of Eu^{3+} (617 nm) under the excitation of near-UV or 532 nm. The lowest concentration of Tb^{3+} improved the luminescence intensity. The investigation indicates that the phosphors may be a promising candidate phosphor for near-UV and blue LED chips.

5. CONCLUSION AND PERSPECTIVES

5.1 General conclusion

The SWO and SMO double perovskite were obtained by solid state route and it was confirmed through PXRD. SWO and SMO presented a thermo-activated process with E_a value around 1.35 and 1.1 eV, respectively. The Nyquist diagrams were well fitted by two associations of R-CPE for SWO, while the SMO was necessary three associations of R-CPE and SMO. SWO-based DRA presented applicable as microwave antenna. τ_f value for SWO resonator was -207.60 ppm$\cdot$K^{-1} and it is a novel option to be used in association with another phase with positive τ_f values for composite materials to achieve zero τ_f values. The results are important for development of devices that operate in microwaves range, for example, devices for telecommunications operates in microwaves range as wireless antenna, Bluetooth and mobile system. By reflection coefficient measurements and from numerical simulation was identified a possible application of the SMO ceramic as an antenna device operating in the S-Band range (from 2 to 4 GHz), it comprises a frequency band adequated for weather radar, surface ship radar, and some communications satellites. The SWO and SMO phases can be also used as dielectric substrates to fabricate microstrip patch antennas. The dielectric ceramic enables miniaturization of this antennas possibility miniaturization of this device and weight reduction. These two investigations were reported in the international scientific journal in the literature (see attachment) The photoluminescent properties of Sr_3MoO_6:Eu^{3+} indicate that these phosphors exhibit red emission of Eu^{3+} (617 nm) under the excitation of near-UV or 532 nm. The lowest concentration of Tb^{3+} improved the luminescence intensity. The investigation indicates that the phosphors may be a promising candidate phosphor for near-UV and blue LED chips.

5.2 Perspectives

This work can be an extensive study optical, electrical for these double perovskite, for must completed study of this electroceramic the follows stage still achieved:

- Synthesis and luminescent studies: up-conversion emission of Eu^{3+}/Tb^{3+} co-doped Sr_3WO_6 double perovskite phosphors;
- Synthesis and luminescent studies: up-conversion emission of Er^{3+}/Yb^{3+} co-doped and Sr_3MoO_6 and Sr_3WO_6 double perovskite phosphors;

REFERENCES

AARTS, L.*et al*. Downconversion for the Er^{3+}, Yb^{3+} couple in KPb_2Cl_5 - A low-phonon frequency host. **Journal of Luminescence**, v. 131, n. 4, p. 608–613, 2011. North-Holland. Disponível em: <https://www.sciencedirect.com/science/article/pii/S0022231310004734>. Acesso em: 10 jul. 2018.

AHMED, T. *et al*. Magnetic, electronic, and optical properties of double perovskite Bi_2FeMnO_6. **APL Materials**, v. 5, n. 3, p. 035601, 2017. AIP Publishing LLC AIP Publishing. Disponível em: <http://aip.scitation.org/doi/10.1063/1.4964676>. Acesso em: 14 fev. 2017.

ALMEIDA, A. F. L. *et al*. Experimental and numerical investigation of a ceramic dielectric resonator (DRA): $CaCu_3Ti_4O_{12}$ (CCTO). **Physica B: Condensed Matter**, v. 403, n. 4, p. 586–594, 2008. Disponível em: <http://www.sciencedirect.com/science/article/pii/S0921452607008319>. Acesso em: 25 fev. 2014.

AUZEL, F. Upconversion and Anti-Stokes Processes with f and d Ions in Solids. **Chemical Reviews**, v. 104, n. 1, p. 139–174, 2004. Disponível em: < https://pubs.acs.org/doi/10.1021/cr020357g>. Acesso em: 25 fev. 2016.

BACK, M.; MARIN, R.; FRANCESCHIN, M.; et al. Energy transfer in color-tunable water-dispersible Tb-Eu codoped CaF_2 nanocrystals. **Journal of Materials Chemistry C**, v. 4, n. 9, p. 1906–1913, 2016. The Royal Society of Chemistry. Disponível em: <http://xlink.rsc.org/?DOI=C5TC03355A>. Acesso em: 10 jul. 2018.

BALANIS, Constantine. **Modern antenna handbook**. Wiley, 2007.

BALANIS, Constantine. **Antenna Theory: Analysis and Design**. Wiley, 2012.

BHARTI, C.; CHANDA, S.; SINHA, T. P. Electrical transport mechanism in a newly synthesized rare earth double perovskite oxide Sr_2CeTaO_6. **Physica B: Condensed Matter**, v. 409, p. 87–92, 2013. Disponível em: <https://www.sciencedirect.com/science/article/pii/S0921452612009349>. Acesso em: 7 jul. 2018.

BHARTI, C.*et al*. Rietveld refinement and dielectric relaxation of a new rare earth based double perovskite oxide: $BaPrCoNbO_6$. **Journal of Solid State Chemistry**, v. 210, n. 1, p. 219–223, 2014a. Disponível em: < https://www.sciencedirect.com/science/article/pii/S0022459613005707>. Acesso em: 7 jan. 2018.

BHARTI, C.*et al*. Cationic ordering, relaxation dynamics and polaron hopping in a new double perovskite oxide: $BaPrCoTaO_6$. **Journal of Alloys and Compounds**, v. 617, p. 677–682, 2014b. Disponível em: <https://www.sciencedirect.com/science/article/abs/pii/S0925838814018805>. Acesso em: 7 jan. 2018.

BHARTI, C. *et al*. Structural, vibrational and electrical properties of ordered double perovskite oxide $BaLaMnSbO_6$. **Journal of Alloys and Compounds**, v. 590, p. 125–130, 2014. Disponível em: <https://www.sciencedirect.com/science/article/abs/pii/S0925838813031034>. Acesso em: 10 jan. 2018.

BIAN, J. J.; WU, J. Y. Structure and microwave dielectric properties of B-site deficient double perovskite − $Ba[(Mg_{(1-x)}/2Y_{x/3\square x/6})W_{1/2}]O_3$. **Ceramics International**, v. 42, n. 2, p. 3290–3295, 2016. Disponível em: <https://www.sciencedirect.com/science/article/pii/S027288421502026X>. Acesso em: 10 jan. 2018.

BIAN, J. J.; YAN, K.; DONG, Y. F. Microwave dielectric properties of $A_{1-3x/2}La_x(Mg_{1/2}W_{1/2})O_3$ (A=Ba, Sr, Ca; $0.0 \leq x \leq 0.05$) double perovskites. **Materials Science and Engineering: B**, v. 147, n. 1, p. 27–34, 2008. Disponível em: <https://www.sciencedirect.com/science/article/pii/S0921510707006320>. Acesso em: 9 jan. 2018.

BIAN, J. *et al*. Structural stability and microwave dielectric properties of $(1-x)Ba(Mg_{1/2}W_{1/2})O_3-xBa(RE_{2/3}W_{1/3})O_3$ (RE=Sm, Dy, Y, Yb) solid solutions. **Journal of the European Ceramic Society**, v. 35, n. 5, p. 1431–1439, 2015. Disponível em: <https://www.sciencedirect.com/science/article/abs/pii/S095522191400627X>. Acesso em: 15 mar. 2018.

BLEICHER, L.; SASAKI, J. M.; PAIVA SANTOS, C. O. Development of a graphical interface for the Rietveld refinement program DBWS. **Journal of Applied Crystallography**, v. 33, n. 4, p. 1189–1189, 2000. International Union of Crystallography. Disponível em: <http://scripts.iucr.org/cgi-bin/paper?ks0035>. Acesso em: 21 jun. 2014.

BONDARENKO, A. S.; RAGOISHA, G. A. Inverse problem in potentiodynamic electrochemical impedance spectroscopy. **Progress in Chemometrics Research**. New York: Nova Science Publishers, 2005

BT. ISMAIL, N.*et al*. Design and analysis of microstrip Yagi antenna for Wi-Fi application. **2012 IEEE Asia-Pacific Conference on Applied Electromagnetics (APACE)**. p.283–286, 2012. Disponível em: < https://ieeexplore.ieee.org/document/6457677>. Acesso em: 11 jul. 2015.

CAMPOS, R. V. B. *et al*. A Study of the Dielectric Properties of $Al_2O_3-TiO_2$ Composite in the Microwave and RF Regions. **Journal of Electronic Materials**, v. 44, n. 11, p. 4220–4226, 2015. Disponível em: <http://link.springer.com/10.1007/s11664-015-3958-3>. Acesso em: 9 dez. 2015.

CHAKRABORTY, T.*et al*. Magnetocaloric properties of R_2NiMnO_6 (R=Pr, Nd, Tb, Ho and Y) double perovskite family. **Journal of Magnetism and Magnetic Materials**, v. 428, p. 59–63, 2017. Disponível em: <https://www.sciencedirect.com/science/article/abs/pii/S030488531632368X>. Acesso em: 4 jul. 2018.

CHANG, L. L. Y.; PHILLIPS, B. Phase Transition in the System Ca_3WO_6-Sr_3WO_6. **Journal of the American Ceramic Society**, v. 50, n. 8, p. 434–435, 1967. Disponível em: <https://ceramics.onlinelibrary.wiley.com/doi/abs/10.1111/j.1151-2916.1967.tb15151.x>. Acesso em: 12 fev. 2015.

COSTA, M. M.; PIRES JÚNIOR, G. F. M.; SOMBRA, A. S. B. Dielectric and impedance properties studies of the of lead doped (PbO)-Co_2Y type hexaferrite ($Ba_2Co_2Fe_{12}O_{22}$ (Co_2Y)). **Materials Chemistry and Physics**, v. 123, n. 1, p. 35–39, 2010. Disponível em: <http://www.sciencedirect.com/science/article/pii/S0254058410002191>. Acesso em: 21 abr. 2015.

COURTNEY, W. E. Analysis and Evaluation of a Method of Measuring the Complex Permittivity and Permeability Microwave Insulators. **IEEE Transactions on Microwave Theory and Techniques**, v. 18, n. 8, p. 476–485, 1970. Disponível em: <https://ieeexplore.ieee.org/abstract/document/1127271>. Acesso em: 21 abr. 2014.

DEHURY, S. K.; ACHARY, P. G. R.; CHOUDHARY, R. N. P. Electrical and dielectric properties of bismuth holmium cobalt titanate ($BiHoCoTiO_6$): a complex double perovskite. **Journal of Materials Science: Materials in Electronics**, v. 29, n. 5, p. 3682–3689, 2018. Disponível em: <http://link.springer.com/10.1007/s10854-017-8299-y>. Acesso em: 8 mar. 2018.

DRACHE, M.; RAVEZ, J.; HAGENMULLER, P. Les materiaux a proprietes non lineaires du systeme Sr_3WO_6 - Ba_3WO_6. **Solid State Communications**, v. 37, n. 2, p. 139–143, 1981. Disponível em: <http://www.sciencedirect.com/science/article/pii/0038109881907298>. Acesso em: 16 dez. 2015.

EMEN, F. M.; ALTINKAYA, R. Luminescence and thermoluminescence properties of Sr_3WO_6:Eu^{3+} phosphor. **Journal of Luminescence**, v. 134, p. 618–621, 2013. Disponível em: <http://www.sciencedirect.com/science/article/pii/S0022231312004218>. Acesso em: 16 dez. 2015.

GANDHI, A.; KESHRI, S. Microwave dielectric properties of double perovskite ceramics $Ba_2Zn_{1-x}Ca_xWO_6$ (x=0-0.4). **Ceramics International**, v. 41, n. 3, p. 3693–3700, 2015. Disponível em: < https://www.sciencedirect.com/science/article/pii/S0272884214017799>. Acesso em: 28 nov. 2015.

GOMEZ-YAÑEZ, C.; BENITEZ, C.; BALMORI-RAMIREZ, H. Mechanical activation of the synthesis reaction of $BaTiO_3$ from a mixture of $BaCO_3$ and TiO_2 powders. **Ceramics International**, v. 26, n. 3, p. 271–277, 2000. Disponível em: <https://www.sciencedirect.com/science/article/pii/S027288429900053X>. Acesso em: 15 fev. 2014.

HAKKI, B. W.; COLEMAN, P. D. A Dielectric Resonator Method of Measuring Inductive Capacities in the Millimeter Range. **IEEE Transactions on Microwave Theory and Techniques**, v. 8, n. 4, p. 402–410, 1960. Disponível em: <http://ieeexplore.ieee.org/lpdocs/epic03/wrapper.htm?arnumber=1124749>. Acesso em: 19 fev. 2014.

HALDER, S.; DUTTA, A.; SINHA, T. P. Dielectric relaxation and electrical conduction mechanism in A_2HoSbO_6 (A=Ba, Sr, Ca) Double Perovskite Ceramics: An impedance spectroscopic analysis. **Journal of Physics and Chemistry of Solids**, v. 102, p. 79–89, 2017. Disponível em: <http://linkinghub.elsevier.com/retrieve/pii/S0022369716302268>. Acesso em: 3 jan. 2017.

HAO, S.-Z.; ZHOU, D.; LI, W.-B.; PANG, L.-X. Microwave Dielectric Properties of $BiCu_2PO_6$ Ceramics with Low Sintering Temperature. **Journal of Electronic Materials**, v. 46, n. 11, p. 6241–6245, 2017. Disponível em: <https://link.springer.com/article/10.1007/s11664-017-5658-7>. Acesso em: 10 jul. 2017.

HIPPEL, A. VON. **Dielectric materials and applications**. Cambridge: The Techonology Press of MIT, 1954.

HOSSAIN, A.; BANDYOPADHYAY, P.; ROY, S. An overview of double perovskites $A_2B'B''O_6$ with small ions at A site: Synthesis, structure and magnetic properties. **Journal of Alloys and Compounds**, 5. Apr. 2018. Elsevier. Disponível em: <https://www.sciencedirect.com/science/article/pii/S092583881734478X?via%3Dihub>. Acesso em: 8 mar. 2018.

HUSSAIN, I. *et al*. Effects of electron injection on the magnetic and magnetocaloric behavior of Sr_2FeMoO_6 double perovskite. **Journal of Alloys and Compounds**, v. 694, p. 815–822, 2017. Disponível em: < https://www.sciencedirect.com/science/article/abs/pii/S0925838816331814>. Acesso em: 8 mar. 2018.

JAWAHAR, I. N.; MOHANAN, P.; SEBASTIAN, M. T. $A_5B_4O_{15}$ (A=Ba, Sr, Mg, Ca, Zn; B=Nb, Ta) microwave dielectric ceramics. **Materials Letters**, v. 57, n. 24–25, p. 4043–4048, 2003. Disponível em: <https://www.sciencedirect.com/science/article/abs/pii/S0167577X03002623>. Acesso em: 8 mar. 2018.

JIANG, L. *et al*. Effects of Sr-site deficiency on structure and electrochemical performance in Sr_2MgMoO_6 for solid-oxide fuel cell. **Journal of Power Sources**, v. 270, p. 441–448, 2014. Disponível em: <https://www.sciencedirect.com/science/article/abs/pii/S0378775314011239>. Acesso em: 15 mar. 2018.

JING, L.*et al*. Synthesis and optical properties of novel red phosphors Sr_3MoO_6:Eu^{3+} with highly enhanced emission by W^{6+} doping. **Journal of Luminescence**, v. 158, p. 351–355, 2015. Disponível em: <http://www.sciencedirect.com/science/article/pii/S0022231314006097>. Acesso em: 20 nov. 2015.

JOSEPH, N. *et al*. Glass-Free $CuMoO_4$ Ceramic with Excellent Dielectric and Thermal Properties for Ultralow Temperature Cofired Ceramic Applications. **ACS Sustainable Chemistry and Engineering**, v. 4, n. 10, p. 5632–5639, 2016. Disponível em: <http://pubs.acs.org/doi/abs/10.1021/acssuschemeng.6b01537>. Acesso em: 30 mai. 2017.

JUNKER, G. P.*et al*. Effect of an air gap around the coaxial probe exciting a cylindrical dielectric resonator antenna. **Electronics Letters**, v. 30, n. 3, p. 177–178, 1994. Disponível em: < https://ieeexplore.ieee.org/document/267262>. Acesso em: 30 mai. 2017.

JUNKER, G. P.*et al*. Effect of fabrication imperfections for ground-plane-backed dielectric-resonator antennas. **IEEE Antennas and Propagation Magazine**, v. 37, n. 1, p. 40–47, 1995. Disponível em: < https://ieeexplore.ieee.org/document/370580>. Acesso em: 30 mai. 2017.

KAJFEZ, D.; GUILLON, P. **Dielectric Resonators**. Tucker: Noble Publishing Corporation, 1998.

KAYSER, P.*et al*. Structural and magnetic characterization of the double perovskites R_2NiRuO_6 (R = Pr-Er): A neutron diffraction study. **Acta Materialia**, v. 126, p. 114–123, 2017. Disponível em: <http://linkinghub.elsevier.com/retrieve/pii/S1359645416309612>. Acesso em: 18 fev. 2017.

KING, G. *et al*. Crystal structure and phase transitions in Sr_3WO_6. **Inorganic chemistry**, v. 49, n. 13, p. 6058–65, 2010. Society. Disponível em: <http://dx.doi.org/10.1021/ic100598v>. Acesso em: 16 dez. 2015.

KOBAYASHI, K.I. *et al*. Room-temperature magnetoresistance in an oxide material with an ordered double-perovskite structure. **Nature**, v. 395, n. 6703, p. 677–680, 1998. Disponível em: <http://www.nature.com/doifinder/10.1038/27167>. Acesso em: 18 fev. 2017.

KOOPS, C. G. On the Dispersion of Resistivity and Dielectric Constant of Some Semiconductors at Audiofrequencies. **Physical Review**, v. 83, n. 1, p. 121–124, 1951. Disponível em: <http://link.aps.org/doi/10.1103/PhysRev.83.121>. Acesso em: 15 nov. 2015.

LI, L. *et al*. Double perovskite $LiLaMgWO_6$:Eu^{3+} novel red-emitting phosphors for solid sate lighting: Synthesis, structure and photoluminescent properties. **Ceramics International**, v. 43, n. 2, p. 2720–2729, 2017. Disponível em: < https://www.sciencedirect.com/science/article/pii/S0272884216320958>. Acesso em: 11 jan. 2018.

LI, L. *et al*. Luminescence enhancement in the $Sr_2ZnW_{1-x}Mo_xO_6$:Eu^{3+},Li^+ phosphor for near ultraviolet based solid state lighting. **Journal of Alloys and Compounds**, v. 685, p. 917–926, 2016. Disponível em: <https://www.sciencedirect.com/science/article/pii/S0925838816319880?via%3Dihub>. Acesso em: 10 jul. 2018.

LI, S. *et al*. A new red-emitting phosphor of Eu^{3+}-doped $Sr_2MgMo_xW_{1-x}O_6$ for solid state lighting. **Current Applied Physics**, v. 13, n. 7, p. 1288–1291, 2013. Disponível em: <https://www.sciencedirect.com/science/article/pii/S1567173913001491>. Acesso em: 10 jul. 2018.

LI, W. *et al*. Preparation, Crystal Structure and Microwave Dielectric Properties of Rare-Earth Vanadates: $ReVO_4$ (Re = Nd, Sm). **Journal of Electronic Materials**, v. 46, n. 4, p. 1956–1962, 2017. Disponível em: <https://link.springer.com/article/10.1007/s11664-016-5179-9>. Acesso em: 10 jul. 2018.

LI, X. *et al*. Structural and luminescent properties of Eu^{3+}-doped double perovskite $BaLaMgNbO_6$ phosphor. **Ceramics International**, v. 44, n. 2, p. 1909–1915, 2018. Disponível em: <https://www.sciencedirect.com/science/article/pii/S0272884217323374>. Acesso em: 8 mar. 2018.

LIAO, Q. *et al*. Ultra-Low Fire Glass Free $Li_3FeMo_3O_{12}$ Microwave Dielectric Ceramics. (D. Johnson, Ed.)**Journal of the American Ceramic Society**, v. 97, n. 8, p. 2394–2396, 2014. Disponível em: <http://doi.wiley.com/10.1111/jace.13073>. Acesso em: 31 mai. 2017.

LUK, K. M.; LEUNG, K. W. **Dielectric Resonator Antennas**. Hertfordshire: Research Studies Press, 2003.

MAHATO, D. K.; SINHA, T. P. Dielectric, Impedance and Conduction Behavior of Double Perovskite Pr_2CuTiO_6 Ceramics. **Journal of Electronic Materials**, v. 46, n. 1, p. 1–9, 17. Jan. 2016. Springer US. Disponível em: <http://link.springer.com/10.1007/s11664-016-4842-5>. Acesso em: 15 jan. 2017.

MARRERO-LÓPEZ, D.*et al*. High temperature phase transition in SOFC anodes based on $Sr_2MgMoO_{6–\delta}$. **Journal of Solid State Chemistry**, v. 182, n. 5, p. 1027–1034, 2009. Disponível em: < https://www.sciencedirect.com/science/article/pii/S0022459609000255>. Acesso em: 15 jan. 2017.

MCCARTHY, G. J.; GOODEN, C. E. Compound formation in the system $Sr\square Mo\square O$. **Journal of Inorganic and Nuclear Chemistry**, v. 35, n. 8, p. 2669–2672, 1973. Disponível em: <http://www.sciencedirect.com/science/article/pii/0022190273804968>. Acesso em: 15 dez. 2015.

MOULSON, A. J.; HERBERT, J. M. **Electroceramics: materials, properties, applications**. John Wiley & Sons, 2003.

NECHACHE, R. *et al*. Epitaxial thin films of multiferroic Bi_2FeCrO_6 with B-site cationic order. **Journal of Materials Research**, v. 22, n. 08, p. 2102–2110, 2011. Disponível em: <http://www.journals.cambridge.org/abstract_S0884291400036086>. Acesso em: 18 fev. 2017.

OLIVEIRA, L. S. *et al*. Study of the performance of dielectric resonator antennas based on the matrix composite of Al_2O_3-$CaTiO_3$. **Microwave and Optical Technology Letters**, v. 57, n. 4, p. 963–969, 2015. Disponível em: <https://onlinelibrary.wiley.com/doi/full/10.1002/mop.28999>. Acesso em: 18 fev. 2017.

OZER, A.; KILIC, O. B. High Energy Ball Milling of YAG Powders: Sintering Properties and Microstructural Evaluation. **Acta Physica Polonica A**, v. 131, n. 3, p. 329–332, 2017. Disponível em: < http://przyrbwn.icm.edu.pl/APP/PDF/131/a131z3p01.pdf>. Acesso em: 18 fev. 2018.

PAIVA, D. V. M. *et al*. Dielectric investigation of the Sr_3WO_6 double perovskite at RF/microwave frequencies. **RSC Adv.**, v. 6, n. 48, p. 42502–42509, 2016a. Disponível em: <http://xlink.rsc.org/?DOI=C6RA04640A>. Acesso em: 10 jan. 2017.

PAIVA, D. V. M. *et al*. Properties of the Sr_3MoO_6 electroceramic for RF/microwave devices. **Journal of Alloys and Compounds**, v. 748, p. 766–773, 2018. Disponível em: <https://www.sciencedirect.com/science/article/pii/S0925838818310703?via%3Dihub>. Acesso em: 29 mai. 2018.

PANDA, N. *et al*. Structural, dielectric and electrical properties of the Ba_2BiNbO_6 double perovskite. **Journal of Materials Science: Materials in Electronics**, v. 26, n. 6, p. 3797–3804, 2015. Springer US. Disponível em: <http://link.springer.com/10.1007/s10854-015-2905-7>. Acesso em: 18 fev. 2017.

PANG, L.-X.; ZHOU, D. Ca_3WO_6: a novel microwave dielectric ceramic with complex perovskite structure. **Journal of Materials Science: Materials in Electronics**, v. 22, n. 7, p. 807–810, 2011. Disponível em: < https://link.springer.com/article/10.1007/s10854-010-0215-7>. Acesso em: 11 fev. 2016.

PARIDA, S. *et al*. Structural refinement, optical and microwave dielectric properties of $BaZrO_3$. **Ceramics International**, v. 38, n. 3, p. 2129–2138, 2012. Disponível em: <http://linkinghub.elsevier.com/retrieve/pii/S0272884211009096>. Acesso em: 16 dez. 2016.

PASCOAL, C.; MACHADO, R.; PANDOLFELLI, V. C. Determinação de fase vítrea em bauxitas refratárias. **Cerâmica**, v. 48, n. 306, p. 61–69, 2002. Associação Brasileira de Cerâmica. Disponível em: <http://www.scielo.br/scielo.php?script=sci_arttext&pid=S0366-69132002000200004&lng=pt&nrm=iso&tlng=pt>. Acesso em: 21 jun. 2014.

PAVANI, K.; SURESH KUMAR, J.; RAMA MOORTHY, L. Photoluminescence properties of Tb^{3+} and Eu^{3+} ions co-doped $SrMg_2La_2W_2O_{12}$ phosphors for solid state lighting applications. **Journal of Alloys and Compounds**, v. 586, p. 722–729, 2014. Elsevier. Disponível em: <https://www.sciencedirect.com/science/article/pii/S0925838813025607?via%3Dihub>. Acesso em: 10 jul. 2018.

PEREIRA, F. M. M. *et al*. Experimental and numerical investigation of a magnetic resonator antenna based on the M-type hexaferrite ($Ba_xSr_{1-x}Fe_{12}O_{19}$). **Microwave and Optical Technology Letters**, v. 52, n. 2, p. 452–458, 2010. Disponível em: < https://onlinelibrary.wiley.com/doi/abs/10.1002/mop.24931>. Acesso em: 10 jul. 2018.

PETOSA, Aldo. **Dielectric resonator antenna handbook**. Artech House, 2007.

RIETVELD, H. M. Line profiles of neutron powder-diffraction peaks for structure refinement. **Acta Crystallographica**, v. 22, n. 1, p. 151–152, 1967. International Union of Crystallography. Disponível em: <http://scripts.iucr.org/cgi-bin/paper?a05418>. Acesso em: 21 jun. 2014.

ROCHA, G. N. *et al*. Study of the performance of dielectric resonator antennas based on the matrix $BiREWO_6$ [RE = Gd, Y, Nd]. **Microwave and Optical Technology Letters**, v. 54, n. 1, p. 18–23, 2012. Disponível em: <https://onlinelibrary.wiley.com/doi/full/10.1002/mop.26486>. Acesso em: 21 jun. 2014.

RODRIGUES, H. O. *et al*. Experimental and numerical investigation of dielectric resonator

antenna based on the $BiFeO_3$ ceramic matrix added with Bi_2O_3 or PbO. **Journal of Alloys and Compounds**, v. 576, p. 324–331, 2013. Disponível em: <http://www.sciencedirect.com/science/article/pii/S0925838813014060>. Acesso em: 11 dez. 2015.

SAXENA, M.; TANWAR, K.; MAITI, T. Environmental friendly Sr_2TiMoO_6 double perovskite for high temperature thermoelectric applications. **Scripta Materialia**, v. 130, p. 205–209, 2017. Disponível em: <http://linkinghub.elsevier.com/retrieve/pii/S1359646216305875>. Acesso em: 15 jan. 2017.

SEBASTIAN, M. T. **Dielectric materials for wireless communication**. Elsevier, 2008.

SEBASTIAN, M. T.; JANTUNEN, H.; UBIC, R. **Microwave Materials and Applications**. Wiley, 2017.

SHAFEIE, S. *et al*. Crystal structure, thermal expansion and high-temperature electrical conductivity of A-site deficient $La_{2-z}Co_{1+y}(Mg_xNb_{1-x})_{1-y}O_6$ double perovskites. **Journal of Solid State Chemistry**, v. 229, p. 243–251, 2015. Disponível em: < https://www.sciencedirect.com/science/article/pii/S0022459615300177>. Acesso em: 15 jan. 2017.

SHARMA, G. *et al*. Magnetism driven ferroelectricity above liquid nitrogen temperature in Y_2CoMnO_6. **Applied Physics Letters**, v. 103, n. 1, p. 012903, 2013. American Institute of PhysicsAIP. Disponível em: <http://aip.scitation.org/doi/10.1063/1.4812728>. Acesso em: 14 fev. 2017.

SHIMAKAWA, Y.; AZUMA, M.; ICHIKAWA, N. Multiferroic Compounds with Double-Perovskite Structures. **Materials**, v. 4, p. 153–168, 2011. Disponível em: < https://www.ncbi.nlm.nih.gov/pmc/articles/PMC5448468/>. Acesso em: 14 fev. 2017.

SHINDE, K. N. *et al*. Basic mechanisms of photoluminescence. **Phosphate Phosphors for Solid-State Lighting**. v. 174, p.41–60, 2013. Disponível em: <http://link.springer.com/10.1007/978-3-642-34312-4_2>. Acesso em: 10 jul. 2018.

SILVA, A. L. DA. *et al*. Superparamagnetic nano-biocomposites for application as dielectric resonator antennas. **Materials Chemistry and Physics**, v. 185, p. 104–113, 2017. Disponível em: < https://www.sciencedirect.com/science/article/pii/S0254058416307453>. Acesso em: 10 jul. 2018.

SILVA, M. A. S.; FERNANDES, T. S. M.; SOMBRA, A. S. B. An alternative method for the measurement of the microwave temperature coefficient of resonant frequency (τ_f). **Journal of Applied Physics**, v. 112, n. 7, p. 074106, 2012. Disponível em: <http://scitation.aip.org/content/aip/journal/jap/112/7/10.1063/1.4755799>. Acesso em: 1 fev. 2014.

SILVA, P. M. O. *et al*. Radiofrequency and microwave properties study of the electroceramic $BaBi_4Ti_4O_{15}$. **Materials Science and Engineering: B**, v. 182, p. 37–44, 2014. Disponível em: <http://www.sciencedirect.com/science/article/pii/S0921510713004042>. Acesso em: 8 jun. 2014.

SLAVNEY, A. H. *et al*. A Bismuth-Halide Double Perovskite with Long Carrier Recombination Lifetime for Photovoltaic Applications. **Journal of the American Chemical Society**, v. 138, n. 7, p. 2138–2141, 2016. Disponível em: <http://pubs.acs.org/doi/abs/10.1021/jacs.5b13294>. Acesso em: 24 mai. 2017.

SOHN, R. S. T. M. *et al*. Studies of the structural and electrical properties of lithium ferrite ($LiFe_5O_8$). **Physica Scripta**, v. 82, n. 5, p. 055702, 2010. Disponível em: <http://stacks.iop.org/1402-4896/82/i=5/a=055702>. Acesso em: 12 mai. 2015.

TANG, L.; WANG, J.; ZHAI, J. Low-temperature sintering of $Ba_{0.5}Sr_{0.5}TiO_3$-$SrMoO_4$ dielectric tunable composite ceramics for LTCC applications. **Journal of Electronic Materials**, v. 42, n. 8, p. 2542–2548, 2013. Disponível em: <http://link.springer.com/10.1007/s11664-013-2621-0>. Acesso em: 31 mai. 2017.

TIITTANEN, T.; KARPPINEN, M. Magnetic properties and B-site cation ordering in $(Sr_{0.5}Ba_{0.5})_2FeSbO_6$ perovskite. **Journal of Alloys and Compounds**, v. 737, p. 295–298, 2018. Disponível em: <https://www.sciencedirect.com/science/article/pii/S0925838817341488>. Acesso em: 8 mar. 2018.

VASALA, S.; KARPPINEN, M. $A_2B'B''O_6$ perovskites: A review. **Progress in Solid State Chemistry**, v. 43, n. 1, p. 1–36, 2014. Disponível em: <http://www.sciencedirect.com/science/article/pii/S0079678614000338>. Acesso em: 5 jan. 2015.

WANG, L.*et al*. A high quenching content red-emitting phosphor based on double perovskite host $BaLaMgSbO_6$ for white LEDs. **Journal of Alloys and Compounds**, v. 696, p. 443–449, 2017. Disponível em: <http://linkinghub.elsevier.com/retrieve/pii/S0925838816336842>. Acesso em: 15 jan. 2017.

WANG, W. *et al*. The effect of calcium on the properties of $SmBa_{1-x}Ca_xCoCuO_{5+\delta}$ as a cathode material for intermediate-temperature solid oxide fuel cells. **Journal of the European Ceramic Society**, v. 37, n. 4, p. 1–6, 2016. Disponível em: <http://dx.doi.org/10.1016/j.jeurceramsoc.2016.12.017>. Acesso em: 14 fev. 2017.

WANG, Z.; TIAN, Y.; LI, Y. Direct CH_4 fuel cell using Sr_2FeMoO_6 as an anode material. **Journal of Power Sources**, v. 196, n. 15, p. 6104–6109, 2011. Disponível em: < https://www.sciencedirect.com/science/article/abs/pii/S0378775311006689>. Acesso em: 14 fev. 2017.

WU, J. Y.; BIAN, J. J. Structure stability and microwave dielectric properties of double perovskite ceramics − $Ba_2Mg_{1-x}Ca_xWO_6$ (0.0≤x≤0.15). **Ceramics International**, v. 38, n. 4, p. 3217–3225, 2012. Disponível em: <https://www.sciencedirect.com/science/article/pii/S0272884211010947>. Acesso em: 14 fev. 2017.

WU, S. Q. *et al*. B-site ordering and strain-induced phase transition in double-perovskite La_2NiMnO_6 films. **Scientific Reports**, v. 8, n. 1, p. 2516, 2018. Disponível em: <http://www.nature.com/articles/s41598-018-20812-4>. Acesso em: 8 mar. 2018.

WU, Z.Y. *et al*. Double-perovskite magnetic La_2NiMnO_6 nanoparticles for adsorption of bovine serum albumin applications. **Nanoscale research letters**, v. 8, p. 207, 2013. Disponível em: < https://www.ncbi.nlm.nih.gov/pmc/articles/PMC3655024/>. Acesso em: 8 mar. 2018.

ZHANG, H.; MAK, C. L. Impedance spectroscopic characterization of fine-grained magnetoelectric $Pb(Zr_{0.53}Ti_{0.47})O_3–(Ni_{0.5}Zn_{0.5})Fe_2O_4$ ceramic composites. **Journal of Alloys and Compounds**, v. 513, p. 165–171, 2012. Disponível em: <http://www.sciencedirect.com/science/article/pii/S0925838811019670>. Acesso em: 23 abr. 2015.

ZHANG, P. *et al*. Sr_2CoMoO_6 anode for solid oxide fuel cell running on H_2 and CH_4 fuels. **Journal of Power Sources**, v. 196, n. 4, p. 1738–1743, 2011. Disponível em: <https://www.sciencedirect.com/science/article/abs/pii/S0378775310017349>. Acesso em: 23 abr. 2015.

ZHANG, X. *et al*. Deep-red photoluminescence and long persistent luminescence in double perovstkite-type $La_2MgGeO_6:Mn^{4+}$. **Journal of the American Ceramic Society**, v. 101, n. 4, p. 1576–1584, 2018. Disponível em: <http://doi.wiley.com/10.1111/jace.15312>. Acesso em: 8 mar. 2018.

ZHAO, X. *et al*. An efficient charge compensated red phosphor Sr_3WO_6: K^+, Eu^{3+} – For white LEDs. **Journal of Alloys and Compounds**, v. 553, p. 221–224, 2013. Disponível em: <http://www.sciencedirect.com/science/article/pii/S0925838812019597>. Acesso em: 16 dez. 2015.

ZHOU, D. *et al*. Structure, Phase Evolution, and Microwave Dielectric Properties of $(Ag_{0.5}Bi_{0.5})(Mo_{0.5}W_{0.5})O_4$ Ceramic with Ultralow Sintering Temperature. **Inorganic Chemistry**, v. 53, n. 11, p. 5712–5716, 2014. Disponível em: <http://pubs.acs.org/doi/abs/10.1021/ic5004808>. Acesso em: 30 mai. 2017.

ZHOU, D.*et al*. Phase evolution, phase transition, and microwave dielectric properties of scheelite structured $xBi(Fe_{1/3}Mo_{2/3})O_4–(1−x)BiVO_4$ $(0.0 \leq x \leq 1.0)$ low temperature firing ceramics. **Journal of Materials Chemistry**, v. 22, n. 40, p. 21412, 2012. Disponível em: <https://pubs.rsc.org/en/content/articlelanding/2012/jm/c2jm34603f#!divAbstract>. Acesso em: 10 jul. 2017.

ZHOU, D. *et al*. Influence of Ce Substitution for Bi in $BiVO_4$ and the Impact on the Phase Evolution and Microwave Dielectric Properties. **Inorganic Chemistry**, v. 53, n. 2, p. 1048–1055, 2014. Disponível em: < https://www.ncbi.nlm.nih.gov/pubmed/24392840>. Acesso em: 10 jul. 2017.

ZHOU, D. *et al*. Crystal Structure and Microwave Dielectric Properties of an Ultralow-Temperature-Fired $(AgBi)_{0.5}WO_4$ Ceramic. **European Journal of Inorganic Chemistry**, v. 2014, n. 2, p. 296–301, 2014. Disponível em: <http://doi.wiley.com/10.1002/ejic.201300789>. Acesso em: 8 jun. 2017.

ZHOU, D. *et al*. Ferroelastic phase transition compositional dependence for solid-solution $[(Li_{0.5}Bi_{0.5})_xBi_{1-x}][Mo_xV_{1-x}]O_4$ scheelite-structured microwave dielectric ceramics. **Acta**

Materialia, v. 59, n. 4, p. 1502–1509, 2011. Disponível em:
<http://www.sciencedirect.com/science/article/pii/S1359645410007688>. Acesso em: 30 mai.
2017.

ZHOU, D. *et al*. Microwave dielectric properties of $(ABi)_{1/2}MoO_4$ (A = Li, Na, K, Rb, Ag)
type ceramics with ultra-low firing temperatures. **Materials Chemistry and Physics**, v. 129,
n. 3, p. 688–692, 2011. Disponível em:
<http://www.sciencedirect.com/science/article/pii/S0254058411004354>. Acesso em: 8 jun.
2017.

ZHOU, J. *et al*. Exploring the transposition effects on the electronic and optical properties of
$Cs_2AgSbCl_6$ via a combined computational-experimental approach. **Journal of Materials
Chemistry A**, v. 6, n. 5, p. 2346–2352, 2018. Disponível em:
<http://xlink.rsc.org/?DOI=C7TA10062K>. Acesso em: 8 mar. 2018.

ZHU, H. *et al*. Novel chromium doped perovskites A_2ZnTiO_6 (A=Pr, Gd): Synthesis, crystal
structure and photocatalytic activity under simulated solar light irradiation. **Applied Surface
Science**, v. 393, p. 348–356, 2017. Disponível em:
<https://www.sciencedirect.com/science/article/pii/S0169433216321341>. Acesso em: 8 mar.
2018.

ZHU, X. *et al*. New Cu_3TeO_6 ceramics: Phase formation and dielectric properties. **ACS
Applied Materials and Interfaces**, v. 6, n. 14, p. 11326–11332, 2014. Disponível em:
<http://pubs.acs.org/doi/abs/10.1021/am501742z>. Acesso em: 30 mai. 2017.

ATTACHMENT A – COVER PAGE: DIELECTRIC INVESTIGATION OF THE Sr₃WO₆ DOUBLE PEROVSKITE AT RF/MICROWAVE FREQUENCIES

CrossMark
click for updates

Dielectric investigation of the Sr₃WO₆ double perovskite at RF/microwave frequencies

D. V. M. Paiva,[a] M. A. S. Silva,[b] A. S. B. Sombra[b] and P. B. A. Fechine[*a]

This work reports the dielectric properties of Sr₃WO₆ (SWO) double perovskite at radio frequencies as a function of the temperature and a study in microwaves range to evaluate the material as a novel dielectric resonator. Thermo-activated charge transfer process for SWO ceramic was observed and two resistor–capacitor associations were fitted for the Nyquist diagram. SWO presented negative values of temperature coefficient of capacitance (TCC) and the activation energies of dielectric relaxation processes were measured by conductivity (1.35 eV), imaginary modulus (1.38 eV) and imaginary impedance (1.36 eV). For the microwave range, SWO shows high dielectric permittivity (13.57) and dielectric loss (0.0281). The dielectric resonator antenna (DRA) fabricated from SWO ceramic presented an operation frequency in 4.1 GHz and return loss below −40 dB. It was possible to evaluate the performance of the antenna from numerical simulation. From these results, the SWO based DRA shows good properties to be used as a novel microwave dielectric resonator.

1. Introduction

Ceramic oxides with structural formula $A_2B'B''O_6$ are called double perovskite. In this kind of structure, the A site generally is a large divalent cation twelve-coordinated and B′ and B″ sites are octahedral-coordinated with varied oxidation state and commonly occupied by transition metal ions. The double perovskite presents a large number of different compositions, as a wide combination of ions in the B′ and B″ sites, where the final combination must be a sum of charges equal to 8+ or the necessary charge for complete electroneutrality of the structure due to the charges of A site (Ca^{2+}, Sr^{2+}, Li^+, La^{3+} etc.).[1] In this sense, different applications can be obtained by changing in these sites. For example, La_2NiMnO_6 nanoparticles[2] have been studied for a potential carrier for large biomolecules, $Sr_2B'MoO_6$ (B′ = Mg, Mn, Fe, Co, Ni and Zn)[3-5] has been found to be a promising compound as an anode material for solid-oxide fuel-cell (SOFCs) and Bi_2NiMnO_6 presents multiferroic properties at low temperature with potential as nonvolatile memories and sensors.[6] Pang and Zhou[7] investigated Ca_3WO_6 phase, which presented good results for potential microwave applications,[8,9] becoming important for development in wireless communication systems, miniaturization of components such as dielectric filters, and voltage-controlled oscillators.

Sr_3WO_6 (SWO) is another example of double perovskite that has two Sr^{2+} ions in site A and one Sr^{2+} and W^{6+} ions distributed in the B′ and B″ sites. SWO presents four polymorphs (α, β, γ and δ) from low to high temperature.[10] This material has been traditionally studied due to luminescence properties: the photoluminescence and thermoluminescence properties of Sr_3WO_6:Eu³⁺ was reported by Emen and Altinkaya,[11] while Zhigang Zou et al.[12] obtained an efficient charge compensated red phosphor for Sr_3WO_6:K⁺,Eu³⁺ for white LEDs. However, the SWO perovskite structure are also an important oxide class for dielectric materials with calcium, strontium and barium titanate, the most representative of perovskite structure for dielectric properties.

In this work, the best set of parameters to synthesize the SWO phase by solid-state route was achieved by X-ray diffraction (XRD). The dielectric properties of the material were measured at radio frequency as a function of the temperature (298–718 K). For microwave applications, SWO was experimentally measured as a dielectric resonator and supported by numerical simulation. The results set can be used to suggest potential novel applications for SWO phase as a dielectric resonator antennas (DRA) or other devices that operate in the microwaves range (microwave filters, oscillators, radar detectors etc.).

2. Experimental methods

The synthesis of the SWO phase was performed by a solid state route, where stoichiometric amounts of the precursors employed in the process were $SrCO_3$ (97%, Vetec) and WO_3 (99%, Aldrich). These starting materials were activated by milling in the planetary mill, on a Fritsch pulverisette 6, for 2 h with zirconia balls and polyacetal jars. The activated powder

ᵃGrupo de Química de Materiais Avançados (GQMAT), Departamento de Química Analítica e Físico-Química, Universidade Federal do Ceará – UFC, Campus do Pici, CP 12100, CEP 60451-970 Fortaleza, CE, Brazil. E-mail: fechine@ufc.br
ᵇLaboratório de Telecomunicações e Ciência e Engenharia de Materiais (LOCEM), Departamento de Física, Universidade Federal do Ceará, Brazil

ATTACHMENT B – COVER PAGE: PROPERTIES OF THE Sr₃MoO₆ ELECTROCERAMIC FOR RF/MICROWAVE DEVICES

Properties of the Sr_3MoO_6 electroceramic for RF/microwave devices

D.V.M. Paiva [a], M.A.S. Silva [b], A.S.B. Sombra [b], P.B.A. Fechine [a, *]

[a] Grupo de Química de Materiais Avançados (GQMat), Departamento de Química Analítica e Físico-Química, Universidade Federal do Ceará – UFC, Campus do Pici, CP 12100, CEP 60451-970, Fortaleza, CE, Brazil
[b] Laboratório de Telecomunicações e Ciência e Engenharia de Materiais (LOCEM), Departamento de Física, Universidade Federal do Ceará, Brazil

ABSTRACT

The Sr_3MoO_6 (SMO) double perovskite has been studied due to its photoluminescence properties. Herein, the aim of this work is to study the dielectric properties of the SMO in radiofrequency (RF). From impedance spectra, we proposed an equivalent circuit using three associations of R-CPE in parallel. We also evaluated its performance as a microwave device (dielectric resonator antenna - DRA). The SMO-based DRA operated at 3.71 GHz (frequency of operation antenna), with reasonable gain (5.00 dBi) and directivity (5.70 dBi), where these values are close to the ones presented by commercial antennas. Additionally, a numerical simulation is performed to obtain the main parameters for proper device application. Based on our results, SMO electroceramic shows important properties, which can be used for devices operating in the S-band such as weather radar, surface ship radar and communications satellites.

© 2018 Elsevier B.V. All rights reserved.

1. Introduction

Ceramic materials based on double perovskite-type structure have been studied due to their magnetocaloric [1,2], magnetic [3–7], photoluminescent [8–11], photovoltaic [12,13], and multiferroic [14–16] properties. Double perovskites have an $A_2B'B''O_6$ type structure in which the twelve-coordinated A sites are generally occupied by divalent cations, most commonly an alkaline earth element. However, the octahedrally-coordinated B' and B'' sites can be occupied by various ion combinations, due to the different oxidation states, thus maintaining electroneutrality in the oxide [17]. Some of the many diverse applications of these ceramics include photocatalysts [18], thermoelectric devices [19], and electrodes for fuel cells [20].

Many double perovskite electroceramics have been studied with complex impedance spectroscopy (CIS) [21–24] to analyze their electrical response to different frequencies. Dielectric studies of electroceramics in microwave and radiofrequency (RF) have been of great interest due to the innumerous applications in telecommunications and electronic devices.

However, most electroceramics synthesize at a high temperature in a densification process, generating an energy-consuming pathway. Therefore, a variety of materials have been developed based on the well-known low-temperature cofired ceramic (LTCC)

technology, which has found application in the fabrication of integrated microwave devices such as resistors, inductors, and capacitors [25,26]. Sintering aids, such as MoO_3 and TeO_2, are used to lower the sintering temperature of microwave electroceramics. Considering the cost and toxicity, MoO_3 has more advantage to be used in an LTCC [25,27].

There have been many reports about LTCC based molybdates [28–30]. For example, the standard LTCC process for $(Ag_{0.5}Bi_{0.5})MoO_4$ [31] and $(Ag_{0.5}Bi_{0.5})WO_4$ [32] phases were studied, which showed different dielectric properties and sintering temperatures [25]. It is reported that Mo (sheelite structure) [31] and W (wolframite structure) [32] show dielectric permittivity of ~30.4 and ~35.9, temperature coefficient of resonator frequency (TCF) of +57 ppm $°C^{-1}$ and -69 ppm $°C^{-1}$, and sintering temperature of 690 °C and 580 °C, respectively. It is noted that the change of W for Mo provided different structures and opposite TCF values. In our previous work [33], we investigated Sr_3WO_6 (SWO) double perovskite as a potential dielectric resonator antenna (DRA). The similarly between molybdenum (Mo^{6+}) and tungsten (W^{6+}) ionic ratio and oxidation state allows the formulation of new LTCCs based structures mixing Mo^{6+} and W^{6+} ions [25]. However, to our knowledge, the influence of Mo^{6+} on dielectric properties, sintering temperature and DRA application have never been reported for Sr_3MoO_6 (SMO) electroceramics. Actually, few studies examine the properties of SMO double perovskite, such as the red phosphors Sr_3MoO_6:Eu^{3+} applied in the white light emitting diode [34].

Compared to other antenna devices, DRAs have lower weight, cost and size, higher radiation efficiency, and easier manufacturing,

* Corresponding author.
E-mail address: fechine@ufc.br (P.B.A. Fechine).